# Light scattering and roughness properties of optical components for 13.5 nm

Dissertation

zur Erlangung des akademischen Grades
*doctor rerum naturalium* (Dr. rer. nat.)

vorgelegt dem Rat der Physikalisch-Astronomischen Fakultät
der Friedrich-Schiller-Universität Jena

von Dipl.-Phys. Marcus Trost
geboren am 17.08.1982 in Heilbad Heiligenstadt

**Gutachter:**

1. Prof. Dr. rer. nat. habil. Andreas Tünnermann, Friedrich-Schiller-Universität Jena

2. Prof. Dr. rer. nat. habil. Richard Kowarschik, Friedrich-Schiller-Universität Jena

3. Prof. Dr. Daniel Rönnow, University of Gävle, Schweden

**Tag der Disputation:** 30. Juni 2015

# Contents

# 1 Introduction

Optical components for the extreme ultraviolet[1] (EUV) exhibit some of the most challenging fabrication tolerances of any optic produced to date. These requirements are primarily evolving from semiconductor projection lithography which continuously pushes optical fabrication techniques towards never before realized levels of accuracy and surface finish with the predetermined schedule of what became known as Moore's law [2]. Already early in the history of optical lithography, in the year 1965, G. E. Moore stated that the number of transistors per unit area, produced in a more economical way, will double in less than two years. This initial observation and attempt to predict a way for low-cost electronics soon became a self-fulfilling prophecy for the next decades [3].

In order to increase the printing resolution in the lithographic imaging process, the exposure wavelength was gradually decreased, starting from the different spectral lines of mercury arc lamps (g-line at 436 nm and i-line at 365 nm) in the 1960s and late 1980s, to the deep ultraviolet light from excimer lasers at 248 nm (krypton fluoride lasers) and 193 nm (argon fluoride lasers) in the 1990s and early 2000s [4–7]. The next anticipated exposure wavelength for high volume manufacturing is 13.5 nm [8–10].

Along with the continuous reduction of the lithography wavelength, the demands on the surface finish of optical components have drastically increased. This is mainly caused by the strong wavelength dependence of scattered light ($\sim {}^1/_{\lambda^4}$) from interface imperfections [11–14]. Light scattering, on the one hand, removes power from the specular beam and reduces the optical throughput. On the other hand, light scattered close to the specular beam direction propagates through the optical system and causes flare which lowers the optical contrast and resolution [15, 16].

A further challenge is the need to use reflective multilayer coatings in the EUV spectral range, instead of the up to now primarily used transmissive optics in optical lithography, because all materials exhibit low refractive indices and become highly absorbing at these short wavelengths [17, 18]. Understanding the scattering contributions from all interfaces of the multilayer stack thus becomes essential in order to produce high quality optics.

But, besides being a pure loss factor, scattered light also carries valuable information about its possible origins, such as surface roughness, bulk imperfections, or local defects. This can

---

[1] The associated spectral bandwidth ranges from 10 nm to 121 nm [1].

be exploited to characterize optical components by light scattering measurements [19–22]. In particular, the combination of a high sensitivity to small imperfections with the non-contact, fast, as well as non-destructive measurement acquisition offers some unique features compared to conventional roughness characterization techniques, such as atomic force or electron microscopy.

A current challenge during the manufacturing of EUV multilayer optics is the characterization of the substrate roughness over extended surface areas. In particular the large sample dimensions required for high numerical apertures in EUV lithography steppers [23–25] with diameters of more than 100 mm are in direct contrast to the small measurement areas of classical high resolution characterization techniques. The point-wise scanning approach and the resultant long measurement times of these techniques only allow a few isolated measurement positions to be characterized. This bears the risk that the measurement results do not resemble the actual surface finish of most of the substrate area. However, instead of an image of the surface topography, the quantities of interest for the optical performance are the statistical properties of the surface roughness. These can alternatively be derived from angle-resolved light scattering measurements and first-order perturbation scattering theory.

This thesis is therefore, on the one hand, dedicated to the development of new light scattering based roughness characterization techniques particularly for EUV optics. On the other hand, the scattering and roughness evolution of molybdenum/silicon multilayer coatings for a wavelength of $\lambda = 13.5\,\mathrm{nm}$ are studied in order to obtain a deeper understanding between the interplay of substrate roughness, intrinsic thin film roughness, and multilayer interference effects on the scattering characteristics. Based on this information, a novel approach to specifically control the scattering from multilayer coatings is developed, extending earlier theoretical and experimental studies on the scattering characteristics of Mo/Si multilayer stacks [26–29], which focused primarily on just the modeling of the experimentally observed scattering distribution. In this way, it becomes possible to minimize the scattering from multilayer coatings without the classical approach of using ever tighter roughness specifications. Furthermore, the combination of the substrate roughness characterization through light scattering measurements with the modeling of the roughness evolution and scattering characteristics of the multilayer stack enables a detailed prediction of the final EUV reflectance prior to the coating process and thus an early feedback during in the manufacturing process.

In order to keep pace with Moore's law, first plans have also been proposed to reduce the exposure wavelength even further down to ∼6 nm [30–32]. However, this field of research is still at an early stage. Thus, to the best of the author's knowledge, no studies of the multilayer roughness evolution and associated scattering distribution exist although it is widely expected that roughness-induced scattering can become even more critical at this wavelength than at $\lambda = 13.5\,\mathrm{nm}$ due to its strong wavelength dependence [33–35]. In order to investigate the extent to which this holds true and whether it is possible to directly apply the characterization approaches developed for Mo/Si multilayer coatings, a first study of the roughness evolution and scattering of lanthanum and ruthenium based multilayer coatings optimized for a wavelength of $\lambda = 6.7\,\mathrm{nm}$ is presented in this thesis as well.

Even though the innovations of this work are primarily stimulated by optical lithography, other research areas can benefit from them as well. This includes, in particular, EUV microscopy as a reversed equivalent to optical projection lithography [36–40], experiments with free electron lasers [41, 42], or solar astronomy [43–46], where the observation of the EUV light enables the study of the solar corona almost free of contaminating emission from other temperature regimes so that the line-of-sight integration effects can be avoided.

The structure of the thesis is as follows:

In chapter 2, the most relevant definitions for surface roughness and light scattering are introduced. Furthermore, theoretical models for the roughness evolution and scattering from interface imperfections of single surfaces and thin film coatings are presented and discussed with respect to their applicability at $\lambda = 13.5\,\mathrm{nm}$. After the description of the experimental setups for the measurement of light scattering in the EUV and visible spectral ranges in chapter 3, the main achievements of this work are presented in the following three chapters.

In chapter 4, the roughness evolution and scattering of Mo/Si multilayer coatings are studied with the goal to separate and quantify the impact of the different scattering sources as well as to improve the scattering characteristics.

Chapter 5 focuses on the characterization of the substrate roughness by angle resolved light scattering measurements at $\lambda = 13.5\,\mathrm{nm}$ and visible wavelengths close to $\lambda = 400\,\mathrm{nm}$. Limiting effects, such as scattering from particles or Rayleigh scattering from air molecules, are also considered. Furthermore, it is shown how non-flat, grating-like substrates, which are appealing as an optical filtering device for the out-of-band radiation present in the spectrum of EUV plasma sources, can be characterized by angle-resolved light scattering measurements.

In chapter 6, the roughness evolution and scattering from multilayer coatings for $\lambda = 6.7\,\mathrm{nm}$ are investigated with the aim to provide an outlook into future directions and critical aspects of multilayer coatings in optical lithography beyond $\lambda = 13.5\,\mathrm{nm}$.

# 2 Fundamentals

An apt example of light scattering is the diffusely reflected light from this white paper [47, 48] which creates a homogeneous, bright background, giving a high contrast to the black printed letters, necessary to read the text. However, aside from this simple and, of course, subjective description of light scattering, well defined scattering and roughness quantities are necessary for comparable measurement results and theoretical predictions. These are introduced in this chapter. Along these lines, it is also shown how interface roughness is connected to the scattered light from single surfaces and multilayer coatings.

## 2.1 Description of rough surfaces

An elegant way to describe the roughness properties of a surface is provided by statistical quantities. In contrast to the pure surface topography, $z(x, y)$, they enable a compact and direct comparison among different samples and an accentuation of specific topography features [19, 21]. The most obvious quantitative characteristic of a rough surface is the root-mean-square (rms) roughness, $\sigma$, defined as the standard deviation of the surface topography along the evaluation lengths, $L_\mathrm{x}$ and $L_\mathrm{y}$ [49, 50]:

$$\sigma_\infty = \left\{ \lim_{L_\mathrm{x}, L_\mathrm{y} \to \infty} \frac{1}{L_\mathrm{x} L_\mathrm{y}} \int\limits_{-L_\mathrm{y}/2}^{L_\mathrm{y}/2} \int\limits_{-L_\mathrm{x}/2}^{L_\mathrm{x}/2} \left[ z(x, y) - \overline{z} \right]^2 \mathrm{d}x \mathrm{d}y \right\}^{\frac{1}{2}} , \tag{2.1}$$

with $\overline{z}$ denoting the mean surface height. In order to include the lateral structural properties and not only the vertical distribution of the surface height, as is the case for the rms-roughness, more general functions can be used. One of them is the power spectral density, PSD, defined as the squared modulus of the Fourier transform of the surface topography [51–53]:

$$\begin{aligned} \mathrm{PSD}_\mathrm{2D}(f_\mathrm{x}, f_\mathrm{y}) &= \lim_{L_\mathrm{x}, L_\mathrm{y} \to \infty} \frac{1}{L_\mathrm{x} L_\mathrm{y}} \left\langle z(\boldsymbol{f}) z^*(\boldsymbol{f}) \right\rangle \\ &= \lim_{L_\mathrm{x}, L_\mathrm{y} \to \infty} \frac{1}{L_\mathrm{x} L_\mathrm{y}} \left\langle \left| \int\limits_{-L_\mathrm{y}/2}^{L_\mathrm{y}/2} \int\limits_{-L_\mathrm{x}/2}^{L_\mathrm{x}/2} z(x, y) \mathrm{e}^{-2\pi \mathrm{i} (f_\mathrm{x} x + f_\mathrm{y} y)} \mathrm{d}x \mathrm{d}y \right|^2 \right\rangle . \end{aligned} \tag{2.2}$$

The asterisk denotes the complex conjugate quantity and $\langle\cdot\rangle$ an average over an ensemble of interface structures which have statistically equivalent random roughness.

The PSD basically expresses the strength of each roughness component as a function of the surface spatial frequencies, $f_\mathrm{x}$ and $f_\mathrm{y}$. Stochastic processes, such as polishing, etching, or thin film growth, usually lead to an isotropic surface roughness [54, 55]. In this case, the PSD is nearly symmetric in $f = \sqrt{f_\mathrm{x}^2 + f_\mathrm{y}^2}$ and can be averaged over all azimuthal angles, $\phi = \arctan {}^{f_\mathrm{y}}/_{f_\mathrm{x}}$, enabling a compact visualization of the roughness spectrum[1]:

$$\mathrm{PSD}(f) = \frac{1}{2\pi}\int\limits_0^{2\pi} \mathrm{PSD}_{2\mathrm{D}}(f,\phi)\mathrm{d}\phi. \tag{2.3}$$

In practice, every roughness measurement technique is confined to a certain spatial frequency range because of the finite instrumental resolution and the limited sample area. This can be partly overcome by combining the PSDs from various measurement techniques and different scan areas through geometrical averaging in the overlapping spatial frequency range [53]. In this way, also specific bandwidth-limited rms-roughness values can be obtained by numerical integration of the combined PSD:

$$\sigma = \left[2\pi \int\limits_{f_\mathrm{min}}^{f_\mathrm{max}} \mathrm{PSD}(f) f \mathrm{d}f\right]^{\frac{1}{2}}. \tag{2.4}$$

For EUV optical components, the most important bandwidth-limited roughness values are [56]: (i) the high spatial frequency roughness, HSFR, between $f_\mathrm{min} = 1\,\mu\mathrm{m}^{-1}$ and $f_\mathrm{max} = 50\,\mu\mathrm{m}^{-1}$ which determines scattering into large angles and thus the scattering loss; (ii) the mid spatial frequency roughness, MSFR, in the range of $f_\mathrm{min} = 0.001\,\mu\mathrm{m}^{-1}$ to $f_\mathrm{max} = 1\,\mu\mathrm{m}^{-1}$, leading to near angle scattering; and (iii) the low spatial frequency roughness, LSFR, between $f_\mathrm{min} = {}^{1}/_{\mathrm{clear\ aperture}}$ and $f_\mathrm{max} = 0.001\,\mu\mathrm{m}^{-1}$, which causes aberrations. In the limits of $f_\mathrm{min} \to 0$ and $f_\mathrm{max} \to \infty$, the total roughness according to Eq. (2.1) is obtained.

In Fig. 2.1, the three spatial frequency bandwidths are illustrated together with the bandwidths of the roughness characterization techniques primarily used in this thesis. According to this, a comprehensive analysis of the high- and mid-spatial frequencies can be achieved by atomic force microscopy[2] (AFM) and white light interferometry[3] (WLI), respectively. The vertical

---

[1] The PSD functions throughout this thesis are averaged in this manner, unless stated otherwise.

[2] All AFM measurements in this thesis were performed at the Fraunhofer IOF with a Dimension 3100 from the Digital Instruments Veeco metrology group. Single crystalline probes with a nominal tip radius of 10 nm were used and in order to minimize tip degradation, the AFM was operated in TappingMode™ in which the cantilever oscillates near its resonance frequency. The damping of the oscillation amplitude, because of the inter-atomic forces between sample and tip, can then be used to reconstruct the topography.

[3] All WLI measurements in this thesis were performed at the Fraunhofer IOF with a NewView™ 7300 from Zygo.

resolution of both techniques is better than 0.1 nm. The principally covered bandwidths of the two characterization methods, based on the number of sampling points and the scan area or magnification of the objective, are indicated by the hatched areas. In practice, the spatial frequency range is smaller, as delineated by the solid colored areas. Limitations at the upper end occur because of the low-pass behavior of the system transfer function, particularly the optical system of a WLI, the non-infinitesimal tip diameter of the AFM, or simply noise [57]. At the lower end, the PSD calculation is prone to statistical fluctuations because of the low number of data points as compared to higher spatial frequencies, as well as to corrections applied to the topography data in order to compensate sample tilt and the influence of scanner bow in case of the AFM measurements [58–60].

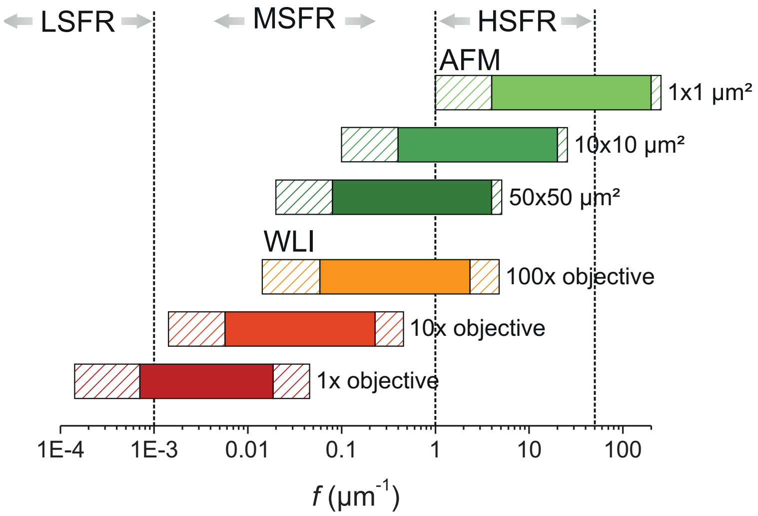

**Fig. 2.1:** Spatial frequency bandwidths covered by AFM and WLI. The hatched areas represent regions in which only qualitative structural information can be obtained.

For the characterization of the LSFR, there exists a large variety of instruments, such as long trace profilers [61, 62], tactile profilometers [63, 64], or various interferometers [65]. However, the more demanding challenge is obtaining a measurement accuracy of better than 0.1 nm on aspherical surfaces, required for EUV optical components. Such a breakthrough in measurement capabilities was achieved by visible light full-aperture phase-shifting diffraction interferometry in the late 1990s [66, 67]. This technique uses a circular aperture with a radius comparable to the light wavelength to achieve a nearly perfect spherical wavefront as a reference from diffraction. In this way, limiting figure errors from classical references, such as null lenses or computer generated holograms as well as auxiliary optics, can be avoided. For the characterization of wavefront errors of fully-assembled EUV lithography projections systems, actinic[4] phase-shifting point-diffraction [68] and shearing interferometers [69] have been developed with the introduction of the first EUV projection lithography test stands [70, 71].

---

[4] Meaning measurements at the application wavelength.

Theoretically equivalent to the surface PSD is the covariance function, $C$, as both functions form a Fourier transform pair [51]. Aside from the calculation of the auto-covariance function from a single surface ($i = j$), also the cross-covariance function ($i \neq j$) among different surface topographies can be determined. In one dimension, the covariance function is defined as [19, 49]:

$$C_{ij}(\tau) = \lim_{L_\mathrm{x} \to \infty} \frac{1}{L_\mathrm{x}} \int\limits_{-L_\mathrm{x}/2}^{L_\mathrm{x}/2} z_i(x) z_j(x + \tau) \mathrm{d}x, \tag{2.5}$$

with the lag length $\tau$. It is interesting to note that the auto-covariance function ($i = j$) is always symmetric and thus the corresponding PSD has to be purely real. In contrast, the cross-covariance functions ($i \neq j$) do not need to be symmetric and can lead to complex cross-correlation PSDs.

As will be shown in Sec. 2.4, the PSD is the most natural quantity for describing scattering from smooth surfaces and, in addition, enables a direct consideration of the bandwidth limits. Thus, in this thesis, the PSD is primarily used for the description of the roughness properties besides the bandwidth-limited rms-roughness.

## 2.2 Reflective multilayer optics

In the EUV spectral range, the refractive index of all materials is close to unity. This leads to a reflectance of less than one percent at best from a single interface at non-grazing incidence angles. It is not possible to use natural crystals either for a higher EUV reflectance; unlike in the x-ray spectral range[5], where high reflectances can be achieved as a result of the constructive interference of the waves reflected from the individual lattice planes, known as Bragg reflection [72]:

$$m\lambda = 2\Lambda \cos\theta_i, \tag{2.6}$$

the spacing between the lattice planes, $\Lambda$, is too small for EUV wavelengths [73]. The parameters $m$ and $\theta_\mathrm{i}$ describe the diffraction order and the angle of incidence which is measured with respect to the sample normal. However, by depositing a thin film stack of alternating materials with layer thicknesses such that the Bragg condition is fulfilled[6] this

---

[5] The associated spectral bandwidth ranges from 0.001 nm to 10 nm [1].

[6] More strictly speaking, Eq. (2.6) describes the path differences for constructive interference and, thus, an optical thickness. Since the refractive index is almost unity for x-ray wavelengths, the difference to the geometrical thickness is usually neglected for this spectral range. However, because of the minor refractive index differences, which are necessary for an EUV multilayer mirror, refraction inside the multilayer has to be considered which leads to a small modification of the Bragg equation as described in [74, 75]. As a consequence, the optimal layer period for constructive interference becomes slightly larger than predicted by Eq. (2.6) if the refractive index of the multilayer materials is smaller than unity, as is the case for EUV wavelengths.

limitation can be overcome. The main advantage of these artificial crystals is that they can be specifically tuned to the desired angle of incidence and wavelength.

In order to attain a large overall reflectance, the two layer materials should exhibit a maximum contrast in their optical indices, which can be achieved by a strong *absorber* and a less absorbing *spacer* material. For a large penetration depth of the EUV radiation and thus many contributing reflecting interfaces, the *absorber* is deposited in thin layers at the nodes of the standing wave field and the desired spacing is achieved by the *spacer* material [76]. The unequal layer thickness is described by the parameter $\Gamma$:

$$\Gamma = \frac{d_{\mathrm{absorber}}}{d_{\mathrm{spacer}} + d_{\mathrm{absorber}}}, \tag{2.7}$$

which expresses the ratio between the absorber thickness, $d_{\mathrm{absorber}}$, and the layer period, $\Lambda = d_{\mathrm{spacer}} + d_{\mathrm{absorber}}$. For an infinite, highly reflecting multilayer stack at $\lambda = 13.5\,\mathrm{nm}$, the optimal ratio is $\Gamma = 0.4$ [77]. For fewer layer periods, the optimal $\Gamma$-value becomes larger, while for narrow-band filters, smaller ratios are used. In principle, the multilayer design concept works even if the difference in the refractive index of both multilayer materials occurs solely in the imaginary part, while the real part of the refractive index is identical in all thin film layers, as first proposed by E. Spiller in the early 1970s [78].

For the EUV lithography wavelength 13.5 nm, reflectances of 75% at normal incidence can theoretically be obtained with multilayer coatings consisting of molybdenum and silicon, as first presented by T. W. Barbee in 1985 [17]. In practice, reflectivities of 70% are, however, hardly being achieved [79–81] as a result of scattering from interface imperfections and a reduced optical contrast at the multilayer interfaces due to intermixing between the two layer materials. This means that more than 97% of the generated EUV light and approximately 50% of the theoretically expected EUV light is lost in typical lithography systems consisting of more than ten mirrors [30, 82]. Hence, there exists an ongoing effort to continuously reduce these losses and raise the optical throughput as well as the image contrast. This can be achieved by introducing barrier and capping layers in order to keep the interference system intact and minimize oxidation of the uppermost layers. A novel approach to how light scattering can be reduced is presented in chapter 4.

## 2.3 Light scattering geometry and definitions

The basic geometry for the definition of specular and scattering quantities is illustrated in Fig. 2.2. The sample is illuminated at an angle of incidence, $\theta_{\mathrm{i}}$, and aside from the specularly reflected and transmitted light, part of the incident light is scattered into off-specular directions described by the polar and azimuthal scattering angles $\theta_{\mathrm{s}}$ and $\varphi_{\mathrm{s}}$. The polar scattering angle is measured with respect to the macroscopic sample normal and the azimuthal scattering angle is defined with respect to the incident plane. In the sketch, the angles $\beta$ and $\varphi_\mathrm{i}$ are introduced as well. The former describes the direction of a skewed roughness structure throughout the $N$ individual interfaces of the multilayer stack. The latter denotes the orientation of the sample with respect to the incident plane.

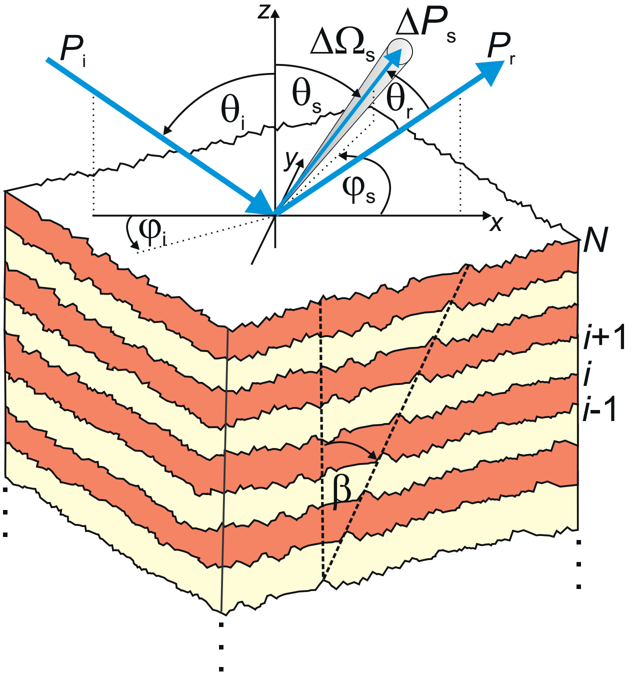

**Fig. 2.2:** Scattering geometry for the definition of specular quantities and scattering from a multilayer coating with associated nomenclature.

The reflectance, $R$, and transmittance of the sample is given as the ratio between the specular reflected, $P_\mathrm{r}$, or the transmitted light power and the incident light power, $P_i$. The angle resolved scattering, ARS, is defined as follows [83, 84]:

$$\mathrm{ARS}(\theta_\mathrm{s}, \varphi_\mathrm{s}, \theta_\mathrm{i}) = \frac{\Delta P_\mathrm{s}(\theta_\mathrm{s}, \varphi_\mathrm{s})}{P_\mathrm{i}\,\Delta\Omega_\mathrm{s}}, \tag{2.8}$$

where $\Delta P_\mathrm{s}$ describes the scattered light power into the detector solid angle, $\Delta\Omega_\mathrm{s}$, and thus enables a measurement system independent quantity, which can be directly compared to theoretical predictions.

Another widely used definition for angle resolved light scattering, in particular in the optical design community, is the bidirectional reflectance/transmittance distribution function, BRDF/BTDF, defined as the scattered radiance normalized by the incidence irradiance [85–87]. The link to the ARS is simply: $\mathrm{BRDF} = \mathrm{ARS}/\cos\theta_\mathrm{s}$. Because of the use of radiometric quantities that are specified with respect to the sample surface, the BRDF/BTDF is, however, only clearly defined for surface scattering and should not be used for the description of bulk scattering [88]. This limitation does not exist for the ARS.

In order to describe the scattering loss from a sample similar to an absorption loss, the encircled scattered energy around the specular reflex[7] can be determined:

$$S(\theta_r) = \int\limits_{0}^{2\pi} \int\limits_{0^\circ}^{85^\circ} \mathrm{ARS}(\theta_\mathrm{s}, \varphi_\mathrm{s}) \mathcal{H}\left(\theta_\mathrm{r} - \arccos\left[\cos\theta_\mathrm{s}\cos\theta_\mathrm{i} + \sin\theta_\mathrm{s}\sin\theta_\mathrm{i}\cos\varphi_\mathrm{s}\right]\right) \sin\theta_\mathrm{s} \mathrm{d}\theta_\mathrm{s} \mathrm{d}\varphi_\mathrm{s}. \tag{2.9}$$

The Heaviside step function, $\mathcal{H}(x)$, which is unity for $x \geq 0$ and zero for $x < 0$, ensures that all values above the polar angle, $\theta_\mathrm{r}$, from the specular beam, are neglected. According to the international standard ISO 13696 [89], the total scattering loss, TS, is then given by:

$$\mathrm{TS} = S(85^\circ + |\theta_\mathrm{i}|) - S(2^\circ). \tag{2.10}$$

By excluding the angular range up to 2° around the reflex, the specularly reflected light is not included in the calculation of the TS value[8].

## 2.4 Theoretical models for light scattering

The benefit of theoretical scattering models is twofold: on the one hand, appropriate scattering theories enable a detailed understanding of the scattering loss mechanisms by comparing simulation results and scattering measurements; on the other hand, the scattering behavior can be predicted prior to manufacturing and provides an early feedback during the manufacturing process of optical components. In this way, it becomes possible to derive roughness and deposition parameters that are sufficient for the application without the risk of over-specification. In the next sections, the theoretical background for light scattering from single surfaces and multilayer coatings is provided.

### 2.4.1 Single surfaces

Several scattering theories have evolved over the last century that describe light scattering from randomly rough surfaces. They can be split into three groups: (i) rigorous calculations [90], (ii) scalar [91, 92], and (iii) vector scattering theories [19, 93, 94]. Though approximative, the

---

[7] The encircled energy around the specularly transmitted light and the corresponding scattering loss can be defined analogously. However, due to the small penetration depth of EUV radiation of a few hundred nanometers, the scattering loss in transmittance will be, in practice, attributed to absorption.

[8] More strictly speaking, the standard requires that the polar scattering angles do not cover the specular reflex but should at least range from $\theta_\mathrm{r} = 2^\circ$ to 85°. However, it has become common practice, to use exactly these boundary values in order to avoid any confusion among various reported TS values.

latter two are very attractive from a characterization point of view, as closed form solutions can be obtained. This enables a direct determination of the roughness properties from scattering measurements as well as a detailed insight into the scattering mechanisms.

Scalar scattering theories are based on the Kirchhoff diffraction integral and describe light scattering as diffraction resulting from random phase variations induced upon the reflected or transmitted wavefront by the rough surface. Typically, a paraxial approximation is made and a Gaussian height distribution is assumed in order to retrieve an analytical solution. This limits the range of possible scattering angles but allows even rough surfaces to be modeled.

The basic procedure of vector perturbation approaches is to solve Maxwell's equations for the ideally smooth surface and replacing the interface roughness by plane surface current sheets, which act as sources of the scattered light. This does not limit the acceptable range of incidence and scattering angles and allows the polarization properties to be considered, but requires that $\sigma \ll \lambda$.

Originally, the vector scattering theory was developed to describe the scattering of radar signals by rough ground and sea levels by S. O. Rice [95], similar to the diffraction calculations of Lord Rayleigh [96]. That is the reason why the approach is also called Rayleigh-Rice scattering theory. In the mid-1970s, E. L. Church introduced this theory to the optics community [51, 97]. The first-order derivation yields a direct relation between the ARS and PSD, viz.:

$$\mathrm{ARS}(\theta_\mathrm{s}, \varphi_\mathrm{s}, \theta_\mathrm{i}) = \frac{16\pi^2}{\lambda^4} \cos\theta_\mathrm{i} \cos^2\theta_\mathrm{s} Q \mathrm{PSD}(f_\mathrm{x}, f_\mathrm{y}). \tag{2.11}$$

The ideal sample characteristics of the perfectly smooth interface, as well as the illumination and detection conditions (dielectric functions, polarization of the incident light and scattered light), are described by the dimensionless optical factor, $Q$. For brevity, the rather lengthy expressions for $Q$ are not repeated here. They can, however, be found in [19, chap. 5] or [51] for all polarization combinations between the incident and scattered light. The link between spatial frequencies and scattering angles is provided by the conical grating equations for first-order diffraction:

$$\begin{aligned} f_\mathrm{x} &= \frac{\sin\theta_\mathrm{s}\cos\varphi_\mathrm{s} - \sin\theta_\mathrm{i}}{\lambda} \\ f_\mathrm{y} &= \frac{\sin\theta_\mathrm{s}\sin\varphi_\mathrm{s}}{\lambda}. \end{aligned} \tag{2.12}$$

By integrating Eq. (2.11) according to Eq. (2.9) closed form solutions for the TS can be retrieved. For normal incidence and under the assumption that the scattered light is concentrated in the vicinity of the specular reflex, this yields:

$$\mathrm{TS} = R_0 \left(\frac{4\pi\sigma}{\lambda}\right)^2 , \tag{2.13}$$

where the optical factor, $Q$, is approximated by the ideal Fresnel reflection of the surface[9], $R_0$. Due to the transformation of the scattering differentials, $\mathrm{d}\theta_\mathrm{s}$ and $\mathrm{d}\varphi_\mathrm{s}$, to spatial frequency differentials based on Eq. (2.12) and the Jacobian determinant, the rms-roughness is explicitly contained in the formula, which has to be evaluated in the relevant scattering spatial frequency range ($f_\mathrm{min} = \sin 2°/\lambda$ and $f_\mathrm{max} = \sin 85°/\lambda$ for normal incidence).

Using scalar scattering theory, the same result as in Eq. (2.13) can be derived for smooth surfaces ($\sigma \ll \lambda$) as shown by H. Davies [98, 99]. In order to ease the mathematics, he used a Gaussian auto-covariance function for the surface roughness. However, as Eq. (2.13) was obtained without any assumptions on the surface PSD, this is not necessarily required. It is interesting to note that the interim result,

$$\mathrm{TS} = R_0 \left[1 - \mathrm{e}^{-\left(\frac{4\pi\sigma}{\lambda}\right)^2}\right] , \tag{2.14}$$

in the paper of H. Davies is also valid for rough surfaces ($\sigma \gg \lambda$), as was later demonstrated by P. Beckmann and A. Spizzichino [91, chap. 5], assuming a Gaussian auto-covariance function as well. However, in a recent publication [100], it was shown that for sinusoidal gratings, which obviously do not exhibit a Gaussian auto-covariance function, Eq. (2.14) provides a very good estimate even for large grating amplitudes by comparing the results to rigorous calculations. Hence, for a large range of surface roughnesses, Eq. (2.14) can be used to predict the scattering loss from single opaque surfaces. The formula also directly reduces to Eq. (2.13) in a second-order Taylor approximation.

### 2.4.2 Thin film coatings

Following from the previous section, the scattered electric field from a single, rough interface within a multilayer stack can be calculated analogously to the scattered light from an opaque substrate, if the interface roughness is small compared to the light wavelength. The only difference is that the incident and scattered light have to propagate to the rough interface or the ambient media. This can, however, easily be achieved by classical matrix propagation algorithms [101–103], assuming an ideal multilayer design and neglecting multiple scattering from other rough interfaces. From a first glance this might seem crude, but as the scattering

---

[9] In the case of s-polarized incident and scattered light in the plane of incidence, $Q$ is exactly given by the surface reflectance at the incident and scattering angle: $Q = [R_0(\theta_\mathrm{i}) R_0(\theta_\mathrm{s})]^{1/2}$ [19, Chapt. 5]. This allows $Q$ to be approximated by the Fresnel reflection at small scattering angles.

losses from the individual interfaces are limited by the perturbation approach, the specular quantities are not significantly altered and the contribution from multiply scattered light can be neglected. For rougher interfaces ($\sigma \geq \lambda$) and large scattering losses, this assumption is not valid anymore.

The final scattered light distribution in reflectance or transmittance is obtained by a superposition of the individual contributions from all interfaces and results in the following ARS for a multilayer consisting of $N$ layers [12, 104, 105]:

$$\mathrm{ARS}(\theta_\mathrm{s}, \varphi_\mathrm{s}, \theta_\mathrm{i}) = \frac{1}{\lambda^4} \sum_{i=0}^{N} \sum_{j=0}^{N} F_i F_j^* \mathrm{PSD}_{ij}(f_\mathrm{x}, f_\mathrm{y}). \tag{2.15}$$

Analogous to a single interface, all properties of the perfectly smooth multilayer and the conditions of illumination and observation (dielectric constants, multilayer design, polarization states, etc.) are described by the optical factors $F_i$. Interference between the scattered electric fields from the individual interfaces of the multilayer is considered by the cross-correlation PSDs ($i \neq j$), besides the individual interface PSDs ($i = j$).

In principle, it is possible to set up a linear system of equations between the individual PSDs of the multilayer and ARS measurements under different conditions (variation of incidence angles, polarization, and wavelength) to solve the inverse scattering problem. However, even for the most simple case of a single layer on an opaque substrate, D. Rönnow demonstrated that such a linear system quickly becomes ill-conditioned and can lead to enormous errors in the determined PSDs [106]. Hence, in practice, the inverse scattering problem cannot be solved without further information, in particular when considering the large number of layers typically encountered in EUV optics ($N > 100$).

## 2.5 Models for roughness evolution of thin films

As outlined in the preceding two sections, modeling of light scattering from interface imperfections requires detailed knowledge about the roughness properties. Even for the large number of interfaces in a multilayer, this information can be retrieved from experimental studies using AFM or cross-sectional transmission electron microscopy, as will be demonstrated in Sec. 4.2.2. This, however, usually results in a destruction of the sample and can be a tedious and time consuming task.

An alternative is given by modeling the thin film growth, which will be described in this section; rather than trying to characterize the deposition process on an atomic level, a continuum model of the thin film growth is presented. This approach was initially proposed in the 1980s for a single growing interface [107, 108] and in the subsequent years direct expressions for the evolving interface PSDs in a multilayer stack were derived [27,109]. An often overlooked characteristic is that, besides of the determination of the individual interface PSDs, the cross-correlation PSDs can be calculated with this model, which is of particular interest from a scattering point of view. Therefore, this aspect is treated in more detail in this section as well.

Furthermore, the structure zone model, initially presented by B. A. Movchan and A. V. Demchishin more than 45 years ago [110], is introduced towards the end of this section, which, in contrast to the continuum model, enables a more phenomenological description of the thin film morphology.

### Linear continuum model

In the absence of relaxation, that is, if the adatoms from the vapor phase stick to the place where they intersect with the already existing thin film, the interface profile of the substrate is exactly replicated throughout the multilayer, $z_i(x, y) = z_0(x, y)$. The simplest model beyond this ballistic growth is the linear continuum model (LCM) which also accounts for a relaxation of the growing surface [109,111,112]. The name of the model results from the fact that only linear terms of the surface derivatives are considered in the equation of motion which describes the evolution of the non-equilibrium growing surface. This is sufficient for high-energetic deposition processes such as magnetron or ion beam sputtering, as it gives very good agreement with experimental results [29,113–116]. In the frequency domain, the LCM can be written as [109,111]:

$$z_i(\boldsymbol{f}) = a_i(\boldsymbol{f}) z_{i-1}(\boldsymbol{f}) + \gamma_i(\boldsymbol{f}), \tag{2.16}$$

where the noise term, $\gamma_i$, describes the random placement and removal of the adatoms and, thus, leads to a continuous roughness increment. The spatial frequency dependent replication factor, $a_i(\boldsymbol{f})$, describes the tendency of the layer to relax to a flat surface. Hence, smoothing and roughening by the thin film can be described, depending on which of the two factors dominate the growth process.

The replication factor is essentially a low-pass filter that replicates the roughness components at low spatial frequencies while high spatial frequency components are damped out:

$$a_i(\boldsymbol{f}) = \mathrm{e}^{-\sum\limits_{n_i} \nu_{n_i} \left|2\pi \boldsymbol{f}\right|^{n_i} d_i}, \quad n_i \in \mathbb{N}. \tag{2.17}$$

The thickness of the $i^{\mathrm{th}}$ layer is described by $d_i$, the relaxation rate is characterized by $\nu_{n_i}$, and the relaxation mechanism is denoted by the integer $n_i$. Several characteristic relaxation mechanisms ($n_i = 1$ viscous flow, $n_i = 2$ evaporation-recondensation, $n_i = 3$ bulk diffusion, and $n_i = 4$ surface diffusion) were identified by W. M. Tong and R. S. Williams [111], which can also take place simultaneously.

By applying the recursion relation of Eq. (2.16) and assuming a constant minimal growth volume, $\Omega_i$, as well as a statistically independent deposition process, the PSD of the $i^{\text{th}}$ layer can be calculated as follows [109]:

$$\mathrm{PSD}_i(\boldsymbol{f}) = \lim_{L_\mathrm{x},L_\mathrm{y}\to\infty} \frac{1}{L_\mathrm{x}L_\mathrm{y}} \langle z_i(\boldsymbol{f}) z_i^*(\boldsymbol{f})\rangle = a_i^2(\boldsymbol{f})\mathrm{PSD}_{i-1}(\boldsymbol{f}) + \mathrm{PSD}_{i,\mathrm{int}}(\boldsymbol{f}) \tag{2.18a}$$

$$\text{where}\quad \mathrm{PSD}_{i,\mathrm{int}}(\boldsymbol{f}) = \lim_{L_\mathrm{x},L_\mathrm{y}\to\infty} \frac{1}{L_\mathrm{x}L_\mathrm{y}} \langle \gamma_i(\boldsymbol{f}) \gamma_i^*(\boldsymbol{f})\rangle = \Omega_i \frac{1-\mathrm{e}^{-2\sum\limits_{n_i} \nu_{n_i} \left|2\pi\boldsymbol{f}\right|^{n_i} d_i}}{2\sum\limits_{n_i} \nu_{n_i} \left|2\pi\boldsymbol{f}\right|^{n_i}}. \tag{2.18b}$$

The first term in Eq. (2.18a) describes the roughness replication of the underlying surface and the second term the intrinsic thin film roughness, $\mathrm{PSD}_{i,\mathrm{int}}(\boldsymbol{f})$, of the layer. As will be demonstrated in Secs. 4.1 and 6.2, the growth parameters ($\Omega_i$, $n_i$, and $\nu_{n_i}$) can be determined by fitting the model PSD to the actual measured top-surface PSD. Once these parameters are known, it is then possible to predict the roughness evolution for different initial substrate PSDs. This makes the LCM a very versatile tool because of the possibility to virtually coat the substrate.

As aforementioned, the recursion relation in Eq. (2.16) also enables the calculation of the cross-correlation PSDs:

$$\mathrm{PSD}_{\substack{i,j\\ i<j}}(\boldsymbol{f}) = \lim_{L_\mathrm{x},L_\mathrm{y}\to\infty} \frac{1}{L_\mathrm{x}L_\mathrm{y}} \left\langle z_i(\boldsymbol{f}) z_j^*(\boldsymbol{f})\right\rangle = a_j(\boldsymbol{f}) a_{j-1}(\boldsymbol{f}) ... a_{i+1}(\boldsymbol{f}) \mathrm{PSD}_i(\boldsymbol{f}). \tag{2.19}$$

Since the individual noise terms, $\gamma_i$, are assumed to be statistically independent, the cross-correlation PSDs become uncorrelated at high spatial frequencies for which the replication factors, $a$, tend to zero. This also agrees with the physical picture of the growth process, which assumes that over a short distance, and thus high spatial frequencies, the adatoms can move freely and the final end position is purely random, while the features over large distances are still reproduced. If the replication factor is close to unity, Eq. (2.19) can be approximated by a partial cross-correlation model [104, 117–119]:

$$\mathrm{PSD}_{i,j}(\boldsymbol{f}) = \min\left[\mathrm{PSD}_i(\boldsymbol{f}), \mathrm{PSD}_j(\boldsymbol{f})\right], \tag{2.20}$$

which is one of the most widely used cross-correlation models for scattering simulations because of its simplicity, besides the extreme cases of uncorrelated ($\mathrm{PSD}_{i,j} = 0$) and fully-correlated interfaces (identical surface and cross-correlations PSDs). Since the low-pass cut-off frequency of the replication factor is usually above $f = 10\,\mu\mathrm{m}^{-1}$, the partial correlation model can often still be successfully applied for EUV scattering simulations, as is demonstrated in [29, 114].

Due to oxidation of the uppermost layers of a multilayer or the formation of intermixing zones between the multilayer materials, the surface profile can contract or expand along the local surface normal. This can be included in the roughness modeling process by the following non-linear term to the LCM [108, 120]:

$$z_i(x,y) = \mathcal{F}\left\{a_i(\boldsymbol{f})z_{i-1}(\boldsymbol{f})\right\} + \delta\sqrt{1+\left[\nabla z_{i-1}(x,y)\right]^2}. \tag{2.21}$$

The contraction or expansion length is described by $\delta$, and $\mathcal{F}$ denotes the Fourier transform. For the samples considered in this work, the local surface gradient, $\nabla z_{i-1}$, will be in most cases very small, because of the use of highly polished substrates. Hence, in general, this non-linear growth can be neglected also because of the small contraction length typically encountered in Mo/Si multilayer coatings of less than $\delta = 1\,\mathrm{nm}$ per bi-layer [77, 120–122]. However, for structured substrates and large resulting surface slopes, as is the case in Sec. 5.4, this non-linear term has to be considered. This is also true when a strong oxidation of the thin film coating occurs, which will be addressed in more detail in Sec. 4.1.1.

### Structure zone model

For most metals and dielectrics, the activation energies for diffusion, required for smoother interfaces, is related to the melting temperature of the material, $T_\mathrm{m}$. Hence, it is expected that the morphology of the thin film depends on the ratio between the substrate temperature, $T_\mathrm{s}$, and the melting temperature of the thin film material, $T_\mathrm{s}/T_\mathrm{m}$. This is the concept of the structure zone model, initially proposed by B. A. Movchan and A. V. Demchishin, based on studies of the structure of thin films prepared by evaporation with electron beam heating [110]. An illustration of their thin film growth model is presented in Fig. 2.3, which highlights three different structure zones.

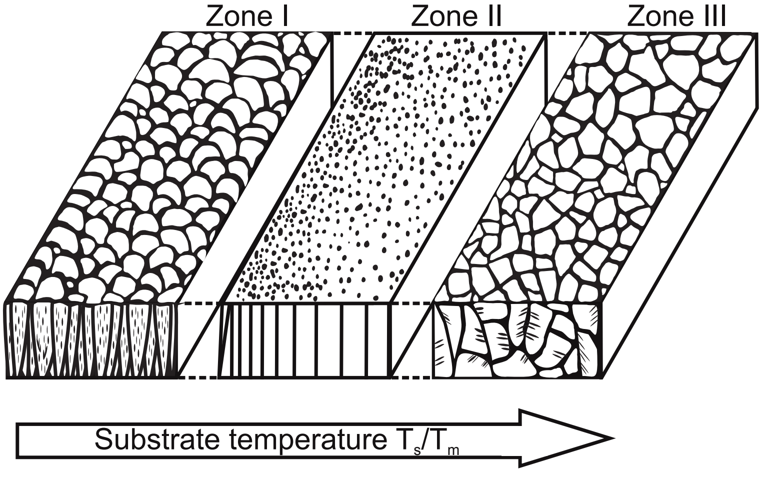

**Fig. 2.3:** Structure zone model of B. A. Movchan and A. V. Demchishin as a function of the normalized substrate temperature. Illustration adapted from [110].

In zone I ($T_\mathrm{s}/T_\mathrm{m} \lesssim 0.3$), the mobility of the adatoms is very low, which leads to a fine-grained porous columnar growth. With increasing surface diffusion in zone II ($0.3 \lesssim T_\mathrm{s}/T_\mathrm{m} \lesssim 0.5$), a dense columnar structure is obtained, and in zone III ($T_\mathrm{s}/T_\mathrm{m} \gtrsim 0.5$), an equiaxed grained structure can be observed. J. Thornton showed that this general trend is valid for sputtered thin films as well [123]. In addition, he demonstrated that with increasing inert gas pressure the transition to the next higher zone is shifted towards higher substrate temperatures. A good review of different structure zone models is given in [124].

Despite the rather simple description, many experimental observations during the thin film growth can be accurately described with the help of the structure zone model [125, 126]. However, the observation of vitreous amorphous, fully dense structures which can be achieved by ion and plasma assisted deposition processes, such as ion beam sputtering, pulsed laser deposition, or magnetron sputtering at low inert gas pressures, cannot be explained by this model. Therefore, K. H. Guenther extended the structure zone model to include a fourth zone and a generalized temperature axis [127]: instead of just the immediate thermal meaning, the parameter $T_\mathrm{s}$ now represents the thermal equivalent of the total particle energy (thermal, kinetic, electronic, chemical) and $T_\mathrm{m}$ is a measure for the activation energy of the thin film material. A schematic of this structure zone model is depicted in Fig. 2.4.

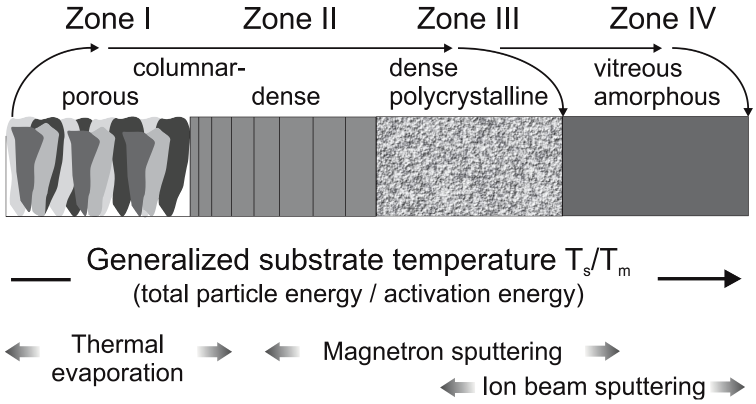

**Fig. 2.4:** Structure zone model of K. H. Guenther as a function of the generalized temperature ratio between the total particle energy of the adatoms and the activation energy of the thin film material. Schematic adapted from [127].

The columnar structure in zones I and II inevitably leads to a high surface roughness because of the cusp-shaped surface topography. Therefore, it is desirable if the thin film growth falls into zone III and IV.

# 3 Experimental set-ups for light scattering measurements

The investigation of light scattering properties of optical components relies on highly sensitive and dedicated light scattering measurement systems. As will be demonstrated in chapter 5, the best suited characterization wavelength does not necessarily have to be the application wavelength, if certain scattering sources are evaluated individually. Nonetheless, when the overall performance is assessed, the wavelength of choice is, of course, the final application wavelength. Therefore, in the following sections, the instrument ALBATROSS – *3D Arrangement for Laser Based Transmittance, Reflectance, and Optical Scatter Measurement* – which covers the ultraviolet, visible, and infrared spectral ranges [128] and the setup MERLIN – *Measurement of EUV reflectance and scattering* – which is dedicated to the EUV lithography wavelength 13.5 nm [129] are briefly introduced.

The combination of both custom built instruments offers the unique opportunity to characterize samples over a broad spectral range and also at the sparsely available wavelength $\lambda = 13.5\,\mathrm{nm}$; so far, light scattering measurements at this wavelength, aside from the system MERLIN, have only been reported from synchrotron facilities in the US [26], Japan [130] and recently Germany [131], as well as from a newly finished instrument at the Institute for Physics of Microstructures in Nizhni Novgorod, Russia, which uses an x-ray tube with a Si anode as light source [132].

For the visible and infrared spectral range, a large array of automated instruments (both angle resolved and hemispherical scattering setups) became available with the advent of the first compact computers in the late 1970s and early 1980s. While the first angle resolved measurement systems were limited to in-plane ($\varphi_\mathrm{s} = 0°$) measurement configurations [54, 133, 134], soon instruments with full three-dimensional (3D) measurement capabilities became available [135–138]. For total scattering measurements, either diffuse integrating spheres [139, 140] or reflective Coblentz spheres [141–144] are utilized.

## 3.1 Instrumentation for visible and infrared wavelengths

A schematic of the instrument ALBATROSS is shown in Fig. 3.1a. Among the various laser wavelengths implemented between $\lambda = 325\,\mathrm{nm}$ and $10.6\,\mu\mathrm{m}$, the most important ones for this thesis are: 395 nm (laser diode), 405 nm (laser diode), 442 nm (helium cadmium laser), 808 nm (laser diode), and 10.6 µm (carbon dioxide laser).

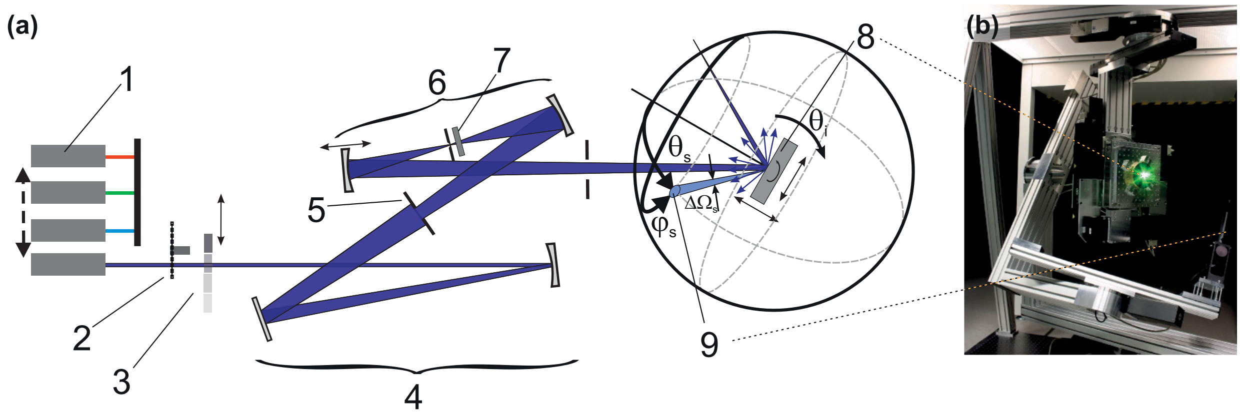

**Fig. 3.1:** Instrument ALBATROSS for light scattering measurements in the ultraviolet, visible, and infrared spectral ranges. **(a)** Schematic illustrating the individual laser light sources (1), mechanical chopper for lock-in amplification (2), attenuation filters (3), beam preparation optics (4), consisting of an iris (5) and spatial filter (6), polarizer (7), as well as the sample (8), and detector (9); **(b)** photograph of 3D goniometer.

Following the optical beam path in the schematic sketch, the light from the individual laser sources (1) passes a mechanical chopper (2) to enable lock-in amplification. Neutral density filters (3) are used to adjust the incident light power in order to operate the detector (9) in its linear response range, even for the large variations in signal powers between incident beam and low-level light scattering.

A clean core beam is achieved by several beam preparation optics (4), including an iris (5) to alter the beam size on the sample and a spatial filter (6). The incident polarization can be set by a polarizer – Glan-Taylor calcite or thin film polarizer (7), which is placed in the spatial filter to reduce stray light. The last focusing mirror can be slightly adjusted in position to compensate for a possible curvature of the sample being tested (8), so that the pinhole (diameter: 100 µm - 530 µm) of the spatial filter is imaged onto the detector aperture. This enables light scattering measurements in close vicinity to the specular reflex and leads to spot diameters of 1 mm to 7 mm on the sample. By using additional focusing lenses, illumination spot diameters of 100 µm can be realized in order to achieve a high resolution on the sample, as will be demonstrated in Sec. 5.4.2. The incident beam can be inclined to the sample normal and goniometer axis by 1° to prevent masking of the incident light by the detector in the retro-reflection direction.

In total, nine automated translational and rotational stages can be used to adjust the polarization properties and to freely position the detector as well as the sample with diameters of up to 700 mm. A photograph of the 3D goniometer is shown in Fig. 3.1b. For light scattering measurements in the ultraviolet, visible, and near-infrared spectral ranges, photomultiplier tubes (R2949 and R5108 from Hamamatsu) are used and a photoconductive mercury cadmium telluride detector from Kolmar Technologies is utilized for $\lambda = 10.6\,\mu\text{m}$.

A critical parameter for reflectance, transmittance, and diffraction measurements is the detector aperture. With a large aperture, also the near specular scattering is attributed to the measurement results, whereas too small apertures might clip off the specular beam. Therefore, the apertures of the detector can be changed to fit the specific requirements with diameters between 0.5 mm and 5 mm. The system itself is situated in an ISO class 7 clean room under additional laminar flow boxes (effective ISO class 5 clean room) [145].

The dominant sources of uncertainty in light scattering measurements based on goniometric setups are the effective size of the detector solid angle, fluctuations of the laser output power, the transmittance of the attenuation filters, and shot noise, as well as excess noise due to statistical fluctuations of the dynode gain in case of the photomultiplier tubes [146]. These effects are minimized by regularly checking the neutral density filter values. In addition, the incident light power and the scattering from a diffuse reflectance standard (Spectralon® for the ultraviolet, visible, near-infrared spectral range and Infragold® for infrared measurements [147]) is determined for the normalization of the detected scattered light. The relative uncertainty for ARS measurements, following error propagation, is 10% [128].

## 3.2 Instrumentation for 13.5 nm

The instrument MERLIN resembles in many aspects the setup ALBATROSS, as can be observed in the schematic in Fig. 3.2a. Yet, the short wavelength imposes several sophisticated, detailed solutions, such as the use of a xenon discharge plasma source (1).

Because of the broad emission spectrum, which ranges from a few nanometers to the visible spectral range, the incident beam has not only to be spatially but also spectrally filtered. The former is achieved similarly to the ALBATROSS system by using a spatial filter (6) with interchangeable pinholes (diameter: 0.1 mm and 0.5 mm); these also allow the incident light power to be adapted to the detected scattering level, as no attenuation optics are used. The latter is accomplished by the small spectral bandwidth of the five Mo/Si multilayer mirrors (full-width bandwidth at half maximum of reflectance: $\Delta\lambda_{\text{FWHM}} = 0.5\,\text{nm}$) used as beam preparation optics (4). However, these mirrors reflect light above $\lambda = 100\,\text{nm}$ comparable to, if not better than, the EUV radiation (see Fig. 5.15). Therefore, a 200 nm thick zirconium filter is positioned at the exit port of the light source (11) to suppress this out-of-band radiation. The Zr-filter also serves as a shield for the collector mirror by minimizing the bombardment with debris (mainly fast Xe ions and sputtered electrode material).

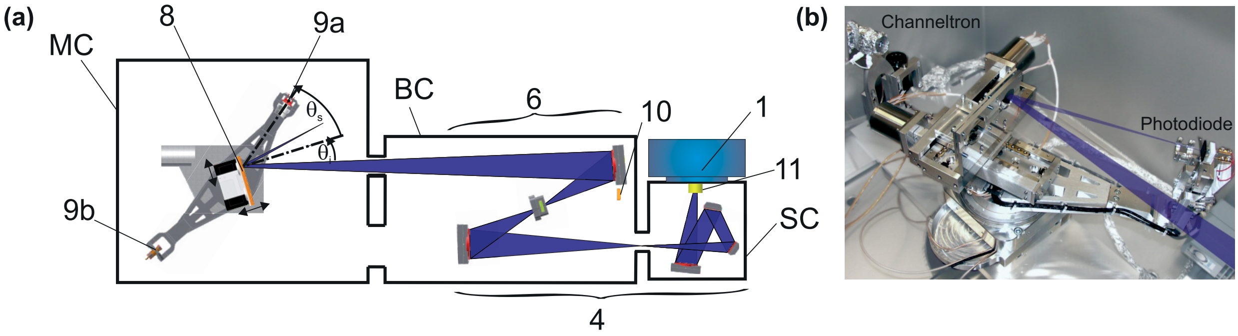

**Fig. 3.2:** Instrument MERLIN for light scattering measurements at $\lambda = 13.5\,\mathrm{nm}$. **(a)** Schematic showing the measurement vacuum chamber (MC), beam preparation vacuum chamber (BC), source vacuum chamber (SC), Xe discharge plasma source (1), beam preparation optics (4), spatial filter (6), sample (8), detectors (9a - photodiode, 9b - channeltron), reference detector (10), and Zr-filter (11); **(b)** photograph of 2D goniometer with indicated reflected light beam.

The EUV light source is based on a hollow cathode triggered pinch plasma [148], which emits a pulse energy of 2.5 mJ within a solid angle of $2\pi\,\mathrm{sr}$ in the EUV band of $\lambda = 13.5\,\mathrm{nm} \pm 2\%$. The pulse duration and repetition rate are 100 ns and 50 Hz, respectively. Taking into account the limited collection solid angle of the first mirror of 0.02 sr, the transmittance of the Zr filter of $< 50\%$, and the reflectance of the Mo/Si multilayers ($R < 65\%$) leads to a pulse energy of less than $0.5\,\mu\mathrm{J}$ at the sample. The spot diameters at the sample position are 1 mm and 2 mm for the smaller and larger pinhole. The polarization of the incident beam, as calculated by the theoretical reflectance characteristics of the beam preparation optics, is 67% s-polarized.

Because of the strong absorption of EUV light by all materials and thus likewise for air under atmospheric pressure (penetration depth $< 150\,\mu\mathrm{m}$), operation in high vacuum at pressures below $1 \times 10^{-4}$ mbar is mandatory to minimize absorption losses below a few tenths of a percent for the beam path length of $\sim$3.5 m. For the evacuation of the vacuum chambers, two turbomolecular pumps are employed, which enable the required system base pressures of $5 \times 10^{-6}$ mbar after a pumping time of 15 minutes.

Due to the low duty cycle of the EUV light source, the detector signal is processed by a digital oscilloscope (Le Croy Waverunner 6200) instead of a lock-in amplifier, after passing a vacuum compatible transimpedance amplifier. Signal triggering is accomplished by a reference detector (10), which detects part of the light that is not collected by the last focusing mirror.

This allows time jitter of the plasma discharge as well as pulse-to-pulse fluctuations to be corrected.

During the course of this work, the instrument was improved by implementing a channeltron (Burle Magnum 5900 EDR [149]) as an additional detector in order to increase the low-level light scattering measurement capabilities. The original uncoated photodiode (IRD AXUV 100 [150]) is still used for higher measurement signals, because of its better signal stability and more linear detector response. By aligning both detectors 165° apart from each other, the masking of the incident light beam during measurements of the incident light power can be avoided, which is necessary for the normalization of the detected scattered light power.

Shadowing of the incident beam in the retro-reflection direction is prevented for the photodiode by tilting the sample by 1° with respect to the goniometer axis and the use of an automated translation stage for the detector height. Since the angular spectrum in which masking occurs for the channeltron is covered by the photodiode, in case of small incidence angles, no automated height variation is implemented for the channeltron. A photograph of the two-dimensional (2D) goniometer with both detectors and the five rotational and translational stages for sample and detector positioning is shown in Fig. 3.2b.

A critically influential factor on the measurement signal of the channeltron is the ionization of residual gas molecules, which leads to afterpulsing and thus enhanced noise. Therefore, the operation pressure should be as low as possible. However, the Xe discharge light source requires an operational pressure of $\sim 10^{-4}$ mbar and constitutes a permanent artificial leak in the vacuum chambers. In order to solve these conflicting requirements, a differential pumping scheme is used. The source chamber and the beam preparation chamber are connected by a 2 mm hole. This enables pressures below $1 \times 10^{-5}$ mbar in the beam preparation and measurement chambers during operation of the discharge source.

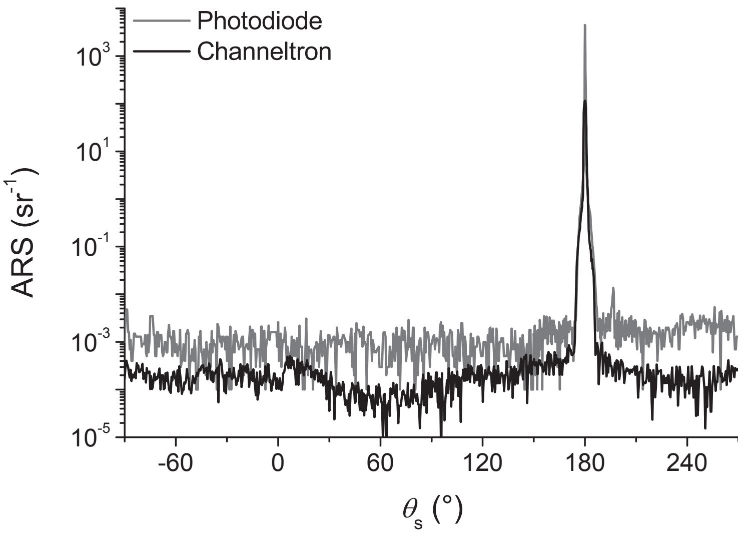

**Fig. 3.3:** Instrument signature at $\lambda = 13.5$ nm.

As can be observed by the instrument signature in Fig. 3.3, which is an ARS measurement without a sample, a dynamic range of more than 7 orders of magnitude and a noise equivalent ARS level below $10^{-3}\,\mathrm{sr}^{-1}$ can be achieved by combining the signals of both detector types.

The shape of the incident beam at a scattering angle of $\theta_\mathrm{s} = 180°$ results from a convolution of the detector aperture and the incident light beam, as well as scattering from the beam preparation optics. The dominating sources of noise are shot noise and, if the channeltron is used, also additional excess noise. In combination with goniometric and calibration errors, the total relative uncertainty of ARS measurements is 6% [151–153]. Compared to the uncertainty budget of the ALBATROSS system, the lower value is mainly achieved through the use of a reference detector and the avoidance of attenuation filters.

According to the Bragg equation [Eq. (2.6)], the condition for maximum reflectance for a given multilayer period depends on the incidence angle and the wavelength. This can be exploited to determine the EUV spectrum at the sample position after spectral filtering by reflectance measurements as a function of the incidence angle. To this end, a narrow-band Mo/Si multilayer with the following design: $(3.5\,\mathrm{nm}\ \mathrm{Mo}\ /31.5\,\mathrm{nm}\ \mathrm{Si})^{30}$, was utilized which has a spectral bandwidth of just $\Delta\lambda_\mathrm{FWHM} = 0.13\,\mathrm{nm}$ as a result of the high Bragg order of $m = 4$. The corresponding reflectance measurement and modeling results are plotted in Fig. 3.4a. The simulations are based on the classical matrix propagation algorithm described in [101] and the refractive index database[1] implemented in [154] which contains data from [155] and [156].

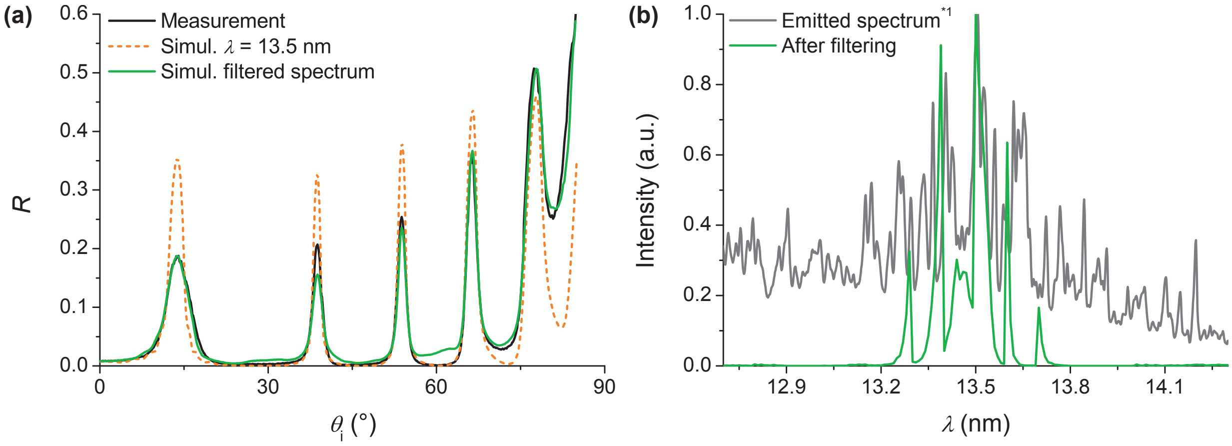

**Fig. 3.4:** Determination of EUV spectrum. **(a)** Reflectance measurements as a function of the incidence angle of a narrow-band reflector as well as simulations based on monochromatic irradiation and estimated spectrum; **(b)** filtered EUV spectrum at sample position compared to emitted spectrum.*1Data provided by source supplier.

Based on an iterative optimization algorithm which minimizes the difference between the

---

[1] All upcoming scattering and reflectance simulations use this database as well.

measured reflectance and the one obtained by weighted arithmetic averaging of the individual reflectance simulations between $\lambda = 1\,\mathrm{nm}$ and $25\,\mathrm{nm}$, the normalized EUV spectrum is attained, since this directly corresponds to the individual weighting factors. The results are plotted in Fig. 3.4b. As desired, the filtered spectrum is centered at 13.5 nm and exhibits several peaks in a bandwidth of ±0.25 nm which correspond to electronic transitions of tenfold ionized Xe [157, 158].

# 4 Light scattering and roughness of thin film coatings

As outlined in Sec. 2.4.2, light scattering from thin film coatings critically depends on the roughness of all interfaces. Therefore, highly polished substrates and deposition processes with high adatom mobilities are commonly used to reduce the surface roughness and to increase the specular reflectance. This can, however, lead to over-specifications; if, for instance, the scattering distribution results primarily from intrinsic thin film roughness, a smoother substrate does not lead to less light scattering. The same is true for the deposition process if the replicated substrate roughness determines the scattering properties.

Hence, identifying the contribution of the individual scattering sources becomes inevitable for improving the optical performance and avoiding excessive specifications. Therefore, in the first part of this chapter, the roughness of single Mo and Si layers as well as periodic Mo/Si multilayer mirrors is analyzed. This information is then used to model the roughness evolution of the multilayer stacks and the associated light scattering properties. In the second part of this chapter, a new approach for reducing light scattering from multilayer coatings, independently of the initial substrate and intrinsic thin film roughness or any modifications to the multilayer design, is presented.

## 4.1 Roughness evolution of EUV multilayer coatings

One approach to determine the roughness properties inside multilayer coatings is to produce multiple samples, each representing a different stage of the layer deposition process. The individual multilayer interfaces can then be directly characterized by stylus and interferometric profilometry. Even if only a few interfaces are characterized, this information is already sufficient to validate the feasibility of the linear growth model, which was presented in Sec. 2.5, and enables a determination of the associated growth parameters. These can then be employed to derive the remaining unknown interface PSDs.

However, when studying the roughness evolution of Mo/Si multilayer coatings, as has been done so far only for complete multilayer stacks [113, 151, 152, 159, 160], the retrieved growth parameters resemble primarily the multilayer period rather than the individual layer materials. Furthermore, because of the large number of fitting variables, often various parameter combinations can be found that describe the experimental PSDs equally well. For instance in [151] and [152], different growth parameter sets were determined for the same Mo/Si multilayer thin film. This ambiguity can be avoided by analyzing the roughness evolution of single thin films, which not only circumvents any coupling of the model parameters between different layer materials, but drastically reduces their total number during the individual modeling processes too. A critical question, however, is whether the observed roughness evolution is representative for the final multilayer stack.

### 4.1.1 Growth of single layers

The single Mo and Si thin films for these investigations were deposited by direct-current magnetron sputtering in an argon atmosphere at the optical coatings department of the Fraunhofer IOF, Jena [161]. As substrates, superpolished[1] Si-wafers were used because of their constant and uniform surface finish as well as low surface roughness (HSFR ∼0.1 nm). The layer thicknesses of ∼5 nm, ∼20 nm, and ∼30 nm for the Si and Mo thin films were chosen to be comparable to those in classical Mo/Si multilayer stacks. Thinner layers were not considered in order to avoid the sharp amorphous-to-crystalline transition for molybdenum, as well as the accompanying change in roughness at a thickness of ∼2 nm [162, 163].

Exemplary AFM topography images as well as the combined PSDs from different measurement positions (scan areas: 1 µm × 1 µm and 10 µm × 10 µm) for the Si thin films are shown in Fig. 4.1.

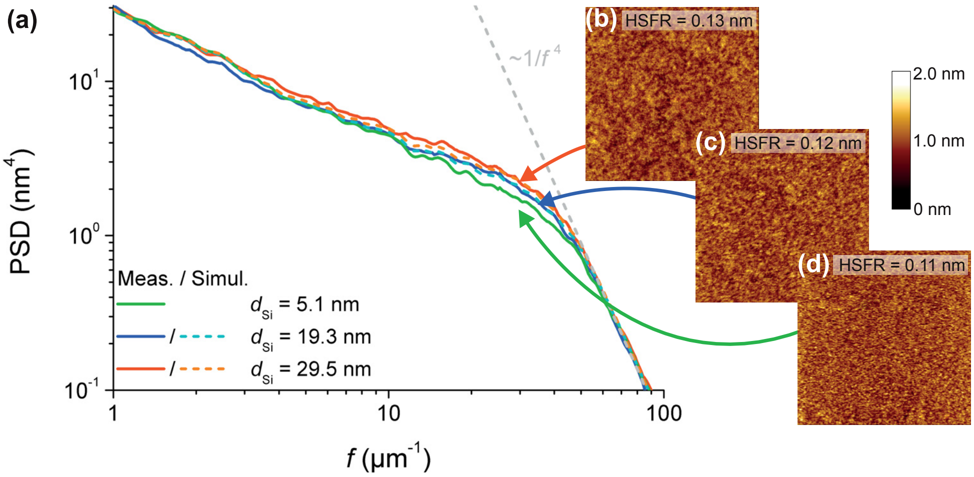

**Fig. 4.1:** Roughness evolution of single Si thin films with different layer thicknesses deposited on superpolished Si-wafers. **(a)** PSDs and **(b)** AFM topography images (scan area: $1 \times 1\,\mu m^2$) after a thin film thickness of ∼30 nm, **(c)** ∼20 nm, and **(d)** ∼5 nm.

---

[1] This colloquial term is often used to describe the surface finish of high quality optics. The associated roughness values, however, depend on the application. In this thesis, superpolishing, as it is common for the EUV community, refers to surfaces with an HSFR close to 0.1 nm.

In contrast to a Si layer in a multilayer stack, the single Si thin films considered here are exposed to air, which leads to an oxidation of the top-surface. Assuming that any associated volume change occurs solely in the direction of the surface normal, the resulting thickness variation can be estimated as follows:

$$\frac{d_{\mathrm{SiO_2}}}{\Delta d_{\mathrm{Si}}} = \frac{V_{\mathrm{SiO_2}}}{V_{\mathrm{Si}}} \approx 1.9, \tag{4.1}$$

based on the molar volumes [164] for Si ($V_{\mathrm{Si}} = 12.1\,\mathrm{cm^3/mol}$) and silicon dioxide ($V_{\mathrm{SiO_2}} = 23.1\,\mathrm{cm^3/mol}$).

Typical literature values for the native oxide layer thickness, as determined by Auger electron depth profiling spectroscopy [165], are $d_{\mathrm{SiO_2}} \sim 2\,\mathrm{nm}$. This leads to an expansion of the single Si layers by $\delta_{\mathrm{SiO_2}} = d_{\mathrm{SiO_2}} - \Delta d_{\mathrm{Si}} \sim 1\,\mathrm{nm}$ and thereby to a modification of the surface topography. Although it is possible to predict these changes by Eq. (2.21) based on the surface topography before oxidation, solving the reverse problem will not lead to a unique reconstruction of the interface profile and cannot be compensated for in the data evaluation. However, since the amplitudes of the roughness components decrease rapidly for larger spatial frequencies, surface features with spatial frequencies above

$$f_{\mathrm{c}} = \frac{1}{2\delta} \tag{4.2}$$

are only critically affected by oxidation. This means that for the small expansion length of $\delta_{\mathrm{SiO_2}} = 1\,\mathrm{nm}$, only extremely high spatial frequencies around $f_{\mathrm{c}} = 500\,\mathrm{\mu m^{-1}}$ are impaired, so that the PSDs before and after oxidation are identical in the spatial frequency range shown in Fig. 4.1. Thus, the slight increase of the PSDs at spatial frequencies around $f = 20\,\mathrm{\mu m^{-1}}$ as well as the topographical changes in the AFM measurements can be attributed to the growth of the single Si layers and are not caused by oxidation.

For the Mo thin films, the oxidation layer consists of molybdenum dioxide and molybdenum trioxide [166, 167], which leads to an expansion factor of:

$$2.1 = \frac{V_{\mathrm{MoO_2}}}{V_{\mathrm{Mo}}} < \frac{d_{\mathrm{MoO_x}}}{\Delta d_{\mathrm{Mo}}} < \frac{V_{\mathrm{MoO_3}}}{V_{\mathrm{Mo}}} = 3.3 \tag{4.3}$$

for the molar volumes of Mo ($V_{\mathrm{Mo}} = 9.3\,\mathrm{cm^3/mol}$), $\mathrm{MoO_2}$ ($V_{\mathrm{MoO_2}} = 19.8\,\mathrm{cm^3/mol}$), and $\mathrm{MoO_3}$ ($V_{\mathrm{MoO_3}} = 30.6\,\mathrm{cm^3/mol}$).

High-purity bulk Mo exhibits a passivation layer thickness between 10 nm and 50 nm [168]. In [77, 166], it was also observed that Mo/Si multilayer coatings terminated by Mo completely oxidize to the uppermost Si layer. Hence, the oxidation layer of the single Mo thin films is most likely not constant and the resulting expansion length is $\delta_{\mathrm{MoO_x}} = d_{\mathrm{MoO_x}} - \Delta d_{\mathrm{Mo}} > 5\,\mathrm{nm}$. According to Eq. (4.2), this leads to changes in the roughness components with spatial frequencies below $f_{\mathrm{c}} = 100\,\mu\mathrm{m}^{-1}$ which already overlap with the relevant spatial frequency range for EUV scattering.

In Fig. 4.2, exemplary AFM topography measurements of the three single Mo thin films are shown. At first glance, the roughness enhancement with increasing layer thickness fits perfectly to the classical multilayer roughness evolution model without contraction or expansion. However, the HSFR of the thinnest Mo layer ($d_{\mathrm{Mo}} \sim 5\,\mathrm{nm}$) already exceeds the roughness of a typical Mo/Si multilayer, with $N = 100$ layers and an accumulative Mo thickness of $> 100\,\mathrm{nm}$, by more than a factor of two (cf. Fig. 4.12). This roughness increase occurs at high and low spatial frequencies, indicating that the entire Mo layer was oxidized. The same is true for the two thicker Mo layers. The roughness evolution of the single Mo layers after oxidation thus substantially differs from those of the Mo/Si multilayer stacks, which prevents a determination of characteristic Mo growth parameters for a multilayer coating.

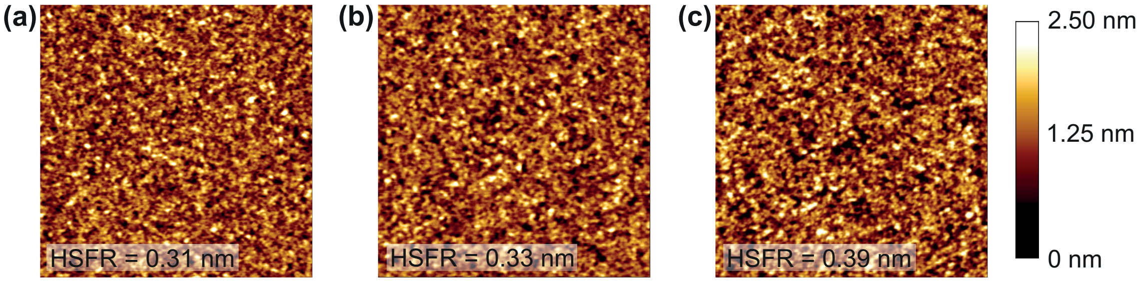

**Fig. 4.2:** AFM topography measurements (scan area: $1 \times 1\,\mu\mathrm{m}^2$) of magnetron sputtered single Mo thin films deposited on superpolished Si-wafers with layer thicknesses of **(a)** ~5 nm, **(b)** ~20 nm, and **(c)** ~30 nm.

In principle, the lower top-surface roughness of a Mo/Si multilayer could result from smoothing of the rough Mo interfaces by the Si layers. However, as should become clear by the data evaluation of the single Si layers in the following paragraphs, the smoothing capabilities of thin Si layers are limited towards the upper end of the high spatial frequency range. Hence, such a broadband roughness increase of the Mo layers cannot be compensated for by the Si layers in a Mo/Si multilayer stack.

As can be observed in Fig 4.1a, the PSDs of the three single Si layers are virtually identical above $f = 50\,\mu\mathrm{m}^{-1}$. This is in agreement with the LCM, which assumes a rapid decrease of the replication factor [see Eq. (2.17)] for high spatial frequencies so that the substrate roughness is not replicated. In this spatial frequency range, the intrinsic thin film roughness reduces to:

$$\mathrm{PSD}_{\mathrm{Si,int}}(2\sum_{n_{\mathrm{Si}}} \nu_{n_{\mathrm{Si}}} \left|2\pi \boldsymbol{f}\right|^{n_{\mathrm{Si}}} d_{\mathrm{Si}} > 1) \sim \frac{\Omega_{\mathrm{Si}}}{2\sum_{n_{\mathrm{Si}}} \nu_{n_{\mathrm{Si}}} \left|2\pi \boldsymbol{f}\right|^{n_{\mathrm{Si}}}} \tag{4.4}$$

and becomes independent of the thin film thickness [cf. Eq. (2.18b)]. Moreover, as the relaxation rates, $\nu_{n_{\mathrm{Si}}}$, do not vary by several orders of magnitude among different relaxation mechanisms, the course of the interface PSD depends primarily on the relaxation process with the smallest $n_{\mathrm{Si}}$ and becomes proportional to $|f|^{-n_{\mathrm{Si,min}}}$ at high spatial frequencies, as indicated by the gray dashed lines in Fig. 4.1a. The corresponding slope of $n_{\mathrm{Si,min}} = 4$ reveals that the most pronounced relaxation mechanism for the Si thin films is surface diffusion, as all other common relaxation mechanisms exhibit smaller integer values [111]. The asymptote also illustrates the smoothing potential of the Si layers; roughness components of the underlying interface that exceed the asymptote will be smoothed, while all other are enhanced.

In order to determine the two remaining growth parameters of the LCM for Si, an iterative optimization algorithm was developed to fit the theoretical top-surface PSDs [Eq. (2.18a)] to the PSDs obtained from the AFM measurements, $\mathrm{PSD}_{\mathrm{exp.}}$, based on the following merit function:

$$M = \sum_{d_{\mathrm{Si}}} \sum_{f=1\,\mu\mathrm{m}^{-1}}^{100\,\mu\mathrm{m}^{-1}} \left\{\log \mathrm{PSD}_{\mathrm{exp.}}(f) - \log\left[\left|a_{\mathrm{Si}}(f)\right|^2 \mathrm{PSD}_{\mathrm{Si,int}}(f) + \mathrm{PSD}_{\mathrm{Sub}}(f)\right]\right\}. \tag{4.5}$$

By taking the difference between the logarithm of the experimental and simulated data, instead of the difference directly, the individual data points are given equal weight although they cover several orders of magnitude.

The necessary Si layer thicknesses for the roughness simulations were estimated from grazing incidence x-ray reflectance measurements at $\lambda = 0.154\,\mathrm{nm}$ [169], assuming a 2 nm native oxidation layer in the subsequent data analysis. According to Eq. (4.1), the initial Si thickness before oxidation is then given by adding 1 nm to the determined Si thickness after oxidation. The Si thicknesses ascertained by this method are 5.1 nm, 19.3 nm, and 29.5 nm, which agree reasonably well with the envisaged values of ∼5 nm, ∼20 nm and ∼30 nm.

Since the LCM can be easily inverted to calculate the PSD of the underlying interface from the top-surface PSD, as contraction or expansion can be neglected in the examined spatial frequency range for Si, the substrate PSD was determined from one of the three measured top-surface PSDs. Using this method, also a simple estimate for the uncertainties of the LCM parameters could be obtained by permutation of the PSD from which the substrate PSD is calculated. The resulting growth parameters for the single Si layers are as follows: $\Omega_{\mathrm{Si}} = (0.026 \pm 0.011)\,\mathrm{nm}^3$, $\nu_{\mathrm{Si}} = (1.46 \pm 0.60)\,\mathrm{nm}^3$, and $n_{\mathrm{Si}} = 4$. Exemplary simulated PSDs for which the substrate PSD was derived from the thinnest Si layer are also displayed in

Fig. 4.1a.

The parameter $n_{\mathrm{Si}}$ can be precisely determined because of the discrete integer steps that describe the relaxation mechanism and the clearly observable asymptotic course of the PSDs at high spatial frequencies. In contrast, the uncertainty ranges of the two other growth parameters critically depend on the accuracy of the AFM measurements and a very smooth substrate, because of the small roughness increment with increasing layer thickness.

### 4.1.2 Growth of multilayer coatings

In order to determine the growth parameters for Mo without the influence from oxidation and to study the roughness evolution of the entire multilayer stack, two periodic thin film stacks with $p = N/2 = 60$ bi-layers, optimized for $\lambda = 13.5\,\mathrm{nm}$ and an angle of incidence of 5° ($\Gamma = 0.33 \pm 0.01$, $\Lambda = 6.91\,\mathrm{nm}$), were deposited onto two differently polished substrates. The substrate of sample A is a superpolished Si-wafer with an HSFR of 0.08 nm. For sample B, a moderately rough fused silica substrate with an HSFR of 0.33 nm was utilized. The same deposition parameters as for the single Si and Mo thin films of the previous section were chosen, so that the growth properties can be directly compared between single layers and multilayer coatings.

In order to enable the characterization of an intermediate interface of the multilayer stack, and not only the top-surface topography, a second specimen of sample A was fabricated in a separate deposition run. However, this time the deposition process was stopped after 40 bi-layers. The Si-wafers for both coatings were taken from the same batch to ensure a comparable substrate finish.

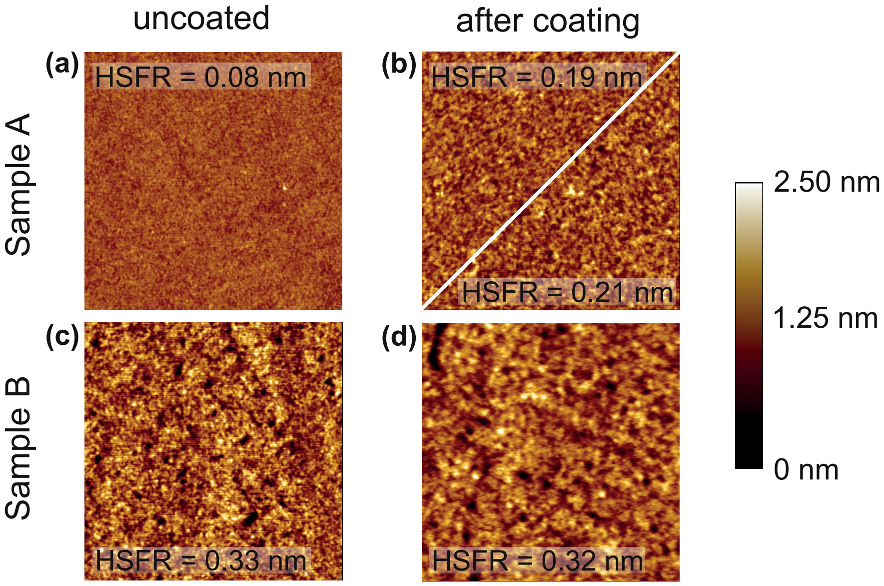

**Fig. 4.3:** AFM topography measurements (scan area: $1 \times 1\,\mu\mathrm{m}^2$) before and after coating of Mo/Si multilayer. **(a)** Substrate of sample A. **(b)** Top-surface of sample A after 40 bi-layers (upper left half) and after 60 bi-layers (lower right half). **(c)** Substrate of sample B. **(d)** Top-surface of sample B after 60 bi-layers.

For each sample, the surface topographies in several scan areas between 1 µm × 1 µm and 50 µm × 50 µm were determined by AFM before and after coating. The exemplary topography images in Fig. 4.3 reveal a roughness enhancement for sample A, whose average increase per bi-layer is more pronounced for the first 40 bi-layers than the top 20 bi-layers. In contrast, sample B exhibits a smoother top-surface than the initial substrate.

From the individual AFM scans, the PSDs were calculated and combined in the overlapping spatial frequency range. They are shown in Fig. 4.4 together with the results from the modeling process. For sample A, a systematic enhancement of the interface PSDs at spatial frequencies around $f = 20\,\mu\text{m}^{-1}$ can be observed, similar to the PSDs of the single Si thin films. At low spatial frequencies, the substrate roughness is replicated by all interface layers. For sample B, the substrate roughness exceeds the intrinsic thin film roughness. Therefore, the top-surface PSD is not significantly increased, and the substrate roughness is mainly replicated. At higher spatial frequencies, the roughness components are smoothed by the multilayer.

This partial replication of the substrate roughness, as well as the influence from the intrinsic thin film roughness at high spatial frequencies, has also been observed for coatings in the visible and deep ultraviolet spectral range [115, 170–172].

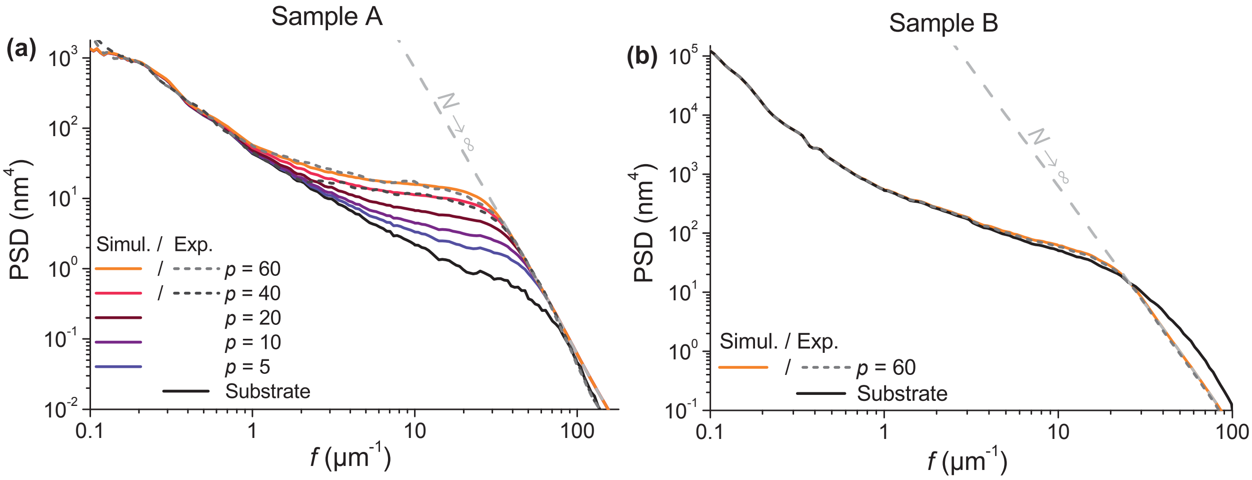

**Fig. 4.4:** Roughness evolution of Mo/Si multilayer on differently polished substrates. The gray dashed line illustrates the equilibration between intrinsic roughening and smoothing for an infinite number of layers. **(a)** Smooth substrate (sample A); **(b)** moderately rough substrate (sample B).

Analogously to the single Si layers, the top-surface PSDs of the LCM were fitted to the measured PSDs. Identical growth parameters were chosen for samples A and B, since they should not depend on the substrate roughness. The parameter space for the Si thin films of the multilayer coating was set around the LCM growth parameters determined from the single Si layers of the previous section, while a much larger but still reasonable parameter space was sampled for the Mo layers. Both multilayer coatings were terminated by Si. Thus, changes to the top-surface topography and PSD from oxidation will only occur outside the spatial frequency range of interest, as discussed earlier, and do not impair the modeling process.

The growth parameters for the best fitting results are as follows: $\Omega_{\mathrm{Si}} = 0.027\,\mathrm{nm}^3$, $\Omega_{\mathrm{Mo}} = 0.046\,\mathrm{nm}^3$, $\nu_{\mathrm{Si/Mo}} = 1.5\,\mathrm{nm}^3$, and $n_{\mathrm{Si/Mo}} = 4$. Hence, for the Mo layers, the main relaxation mechanism is surface diffusion as well. The results are in good agreement with the reported values in [27, 151, 152, 159], which were obtained from multilayer coatings only without any studies of the single layer properties. It could thus not be distinguished whether the assumed identical relaxation parameters of Mo and Si result from the modeling process itself or actually represent the real growth process of the individual layer materials. Now, with the study of the roughness evolution of the single Si thin films, the coupling between the individual growth parameters is avoided. The identical relaxation parameters for Mo and Si are thus not caused by the modeling procedure.

Also, the growth volumes of both materials could be separated. The estimated value for the Si thin films is close to the atomic volume of Si ($\mathcal{V}_{\mathrm{Si}} = 0.02\,\mathrm{nm}^3$), indicating an amorphous structure, in accordance with experimental observations from cross-section high resolution transmission electron microscopy (HRTEM) measurements [173]. The growth volume for Mo is considerably larger than its atomic volume ($\mathcal{V}_{\mathrm{Mo}} = 0.016\,\mathrm{nm}^3$), suggesting a polycrystalline structure.

This difference in the structure of the thin films can also be explained in the framework of the extended structure zone model proposed by K. H. Guenther (see Fig. 2.4). Provided that the thermal equivalent of the total particle energy of the Mo and Si adatoms, $T_{\mathrm{s}}$, is comparable during the deposition process, the different melting temperatures of both materials ($T_{\mathrm{m,\,Mo}} = 2895\,\mathrm{K}$, $T_{\mathrm{m,\,Si}} = 1683\,\mathrm{K}$) lead to a higher $T_{\mathrm{s}}/T_{\mathrm{m}}$ ratio for Si than for Mo. It is thus more likely that the Si thin films fall into the vitreous amorphous zone IV, while the Mo layers settle in the polycrystalline zone III. In addition to the pure structural differences between both layer materials, this influences the interface topography as well. Therefore, the Si-on-Mo interfaces should be rougher than the Mo-on-Si boundaries, which agrees with the higher LCM growth volume of Mo than for Si as well as the good smoothing capabilities of the Si layers at high spatial frequencies.

Based on the growth parameters, the hidden interface PSDs can be determined for the given substrate PSD as shown in Fig. 4.4a. They clearly illustrate the continuous roughness enhancement at high spatial frequencies. The experimental surface PSD of the intermediate interface of sample A after 40 bi-layers, which was not used during the fitting routine, is also precisely predicted over the entire characterized spatial frequency range, confirming the modeling procedure. Furthermore, this good agreement reveals that the growth parameters are characteristic to the deposition process and do not change among different deposition runs, provided that the deposition parameters are not changed. This allows the multilayer roughness evolution to be predicted for other substrate PSDs.

For an infinite number of layers, the substrate roughness eventually becomes irrelevant and the top-surface PSD converges to:

$$\lim_{N\to\infty} \mathrm{PSD}_N = \frac{\mathrm{PSD}_{\mathrm{Si,int}} + a_{\mathrm{Si}}^2 \mathrm{PSD}_{\mathrm{Mo,int}}}{1 - a_{\mathrm{Si}}^2 a_{\mathrm{Mo}}^2}. \tag{4.6}$$

This balance between the smoothing of the underlying interface and the roughening by the thin film is illustrated by the gray dashed lines in Fig. 4.4; for sample A, this limit is quickly approached at high spatial frequencies by roughening. Because of the higher substrate roughness of sample B, the interface PSDs converge towards the same limit by smoothing at high spatial frequencies. Hence, the limit of $\mathrm{PSD}_N$ provides a descriptive quantity for the amount of smoothing or roughening that can be expected at high spatial frequencies for a given substrate PSD.

The smoothing potential of a single layer within the coating can be portrayed by the replication factor and the intrinsic thin film roughness, which are plotted in Fig. 4.5. Above $f = 40\,\mu\mathrm{m}^{-1}$, the replication factors for Mo and Si quickly drop to zero. Hence, roughness components of the substrate or underlying interfaces are not replicated above this transition and the interface roughness can be attributed to just the intrinsic thin film roughness.

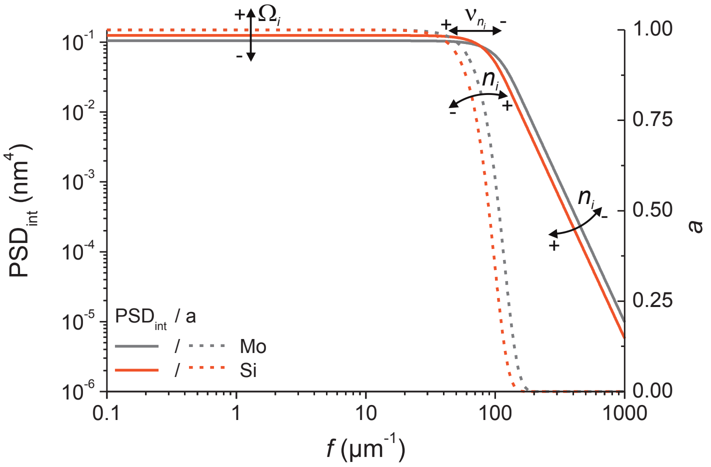

**Fig. 4.5:** Intrinsic thin film PSD and replication factor of single Si and Mo layers, based on the LCM parameters given in the text. The layer thicknesses are: $d_{\mathrm{Si}} = 4.63\,\mathrm{nm}$ and $d_{\mathrm{Mo}} = 2.28\,\mathrm{nm}$.

The vanishing replication of the interface roughness at high spatial frequencies also leads to uncorrelated interfaces above $f = 40\,\mu\mathrm{m}^{-1}$, while they are correlated below this transition. So, up to this change in correlation, which corresponds to a scattering angle of ∼20° from the specular reflex at $\lambda = 13.5\,\mathrm{nm}$ [cf. Eq. (2.12)], the partial cross-correlation model can still be used for multilayer scattering simulations.

In Fig. 4.5, the trend of the individual growth parameters is also indicated. According to this, it is desirable to achieve a low growth volume, $\Omega_i$, so that the intrinsic thin film PSD becomes smaller. The relaxation rate, $\nu_{n_i}$, should be as high as possible in order to shift the cut-off frequency of the replication factor to smaller spatial frequencies.

The layer thickness has the same influence as the growth volume and relaxation rate. That is why the curves of the two materials differ slightly from each other, although most of the growth parameters are identical. The different layer thicknesses also explain why the intrinsic thin film PSD for the Si layers is higher than the one for the Mo thin films, although the growth volume is larger for the latter.

The choice of a perfect relaxation mechanism seems to be a compromise because the intrinsic thin film roughness decreases for higher $n_i$, while the slope of the replication factor becomes more favorable for smaller $n_i$. However, as the highest spatial frequency that contributes to scattering at $\lambda = 13.5\,\mathrm{nm}$ at small incidence angles is below $f = 100\,\mu\mathrm{m}^{-1}$ [see Eq. (2.12)], this increase in the thin film roughness is of no relevance to the scattering properties. The greater influence of the parameter $n_i$ on the scattering characteristics thus originates from the change in the replication factor. Therefore, a low $n_i$ is desirable in order to smoothen the roughness components of the underlying interface at smaller spatial frequencies. This can be achieved by changing the deposition parameters. For instance, for the Mo/Si multilayer coatings, which are presented in Sec. 4.2.3, the characteristic relaxation process could be changed by varying the argon pressure and the substrate to target distance from surface diffusion ($n_{\mathrm{Si/Mo}} = 4$) to bulk diffusion ($n_{\mathrm{Si/Mo}} = 3$), while the growth volumes for Si and Mo are unchanged and the relaxation rate decreased only slightly from $\nu_{\mathrm{Si/Mo}} = 1.5\,\mathrm{nm}^3$ to $1.3\,\mathrm{nm}^2$. In this way, the top-surface roughness of the multilayer stack could be reduced by 30%.

## 4.2 Light scattering of EUV multilayer coatings

With the knowledge of all interface PSDs of the Mo/Si multilayer coatings from the LCM, the ARS can be predicted by first-order vector scattering theory. Moreover, the separation between roughness replication and roughness enhancement by the LCM enables an independent investigation of the influence of the substrate and the intrinsic thin film roughness. Surprisingly and in contrast to coatings for the visible and deep ultraviolet spectral range [170–172], only the first aspect, of determining the roughness evolution and scattering properties for the specific sample at hand, has been primarily considered in the literature on EUV coatings [29,113,116,160], while the latter has not yet received much attention. Therefore, the following sections focus in particular on the impact of the roughness properties of the substrate and the thin film coatings on the overall scattering characteristics of Mo/Si multilayer stacks. Furthermore, the influence of the roughness cross-correlation properties is examined.

## 4.2.1 Influence of the substrate and intrinsic thin film roughness

Based on the PSDs from the roughness modeling process, the ARS of both Mo/Si multilayer coatings were calculated, according to Eq. (2.15), for three different cases:

- *General model*: Both the substrate and the intrinsic thin film roughness are taken into account.
- *Perfect coating*: Only the substrate roughness is replicated through the multilayer stack, while intrinsic thin film roughness and smoothing effects are neglected.
- *Perfect substrate*: The roughness evolution starts from a plane substrate with no roughness. Only intrinsic thin film roughness is considered.

The corresponding results, as well as the scattering measurements at $\lambda = 13.5\,\text{nm}$, are presented in Fig. 4.6. For the description of the interference conditions, the linear continuum cross-correlation model according to Eq. (2.19) and the partial cross-correlation model based on Eq. (2.20) were used. As can be observed at large scattering angles, a better agreement between scattering measurements and modeling results is obtained for the linear continuum cross-correlation model than for the partial cross-correlation model. The latter underestimates the ARS at large scattering angles. Although these observations might imply that a partial correlation between the individual interfaces of the multilayer stack is more favorable, it should be noted that this interference effect strongly depends on the path differences between the individual contributing rough interfaces. For instance, close to the specular beam, the scattered light from most interfaces of the multilayer stack interferes constructively, in contrast to the destructive interference at large scattering angles.

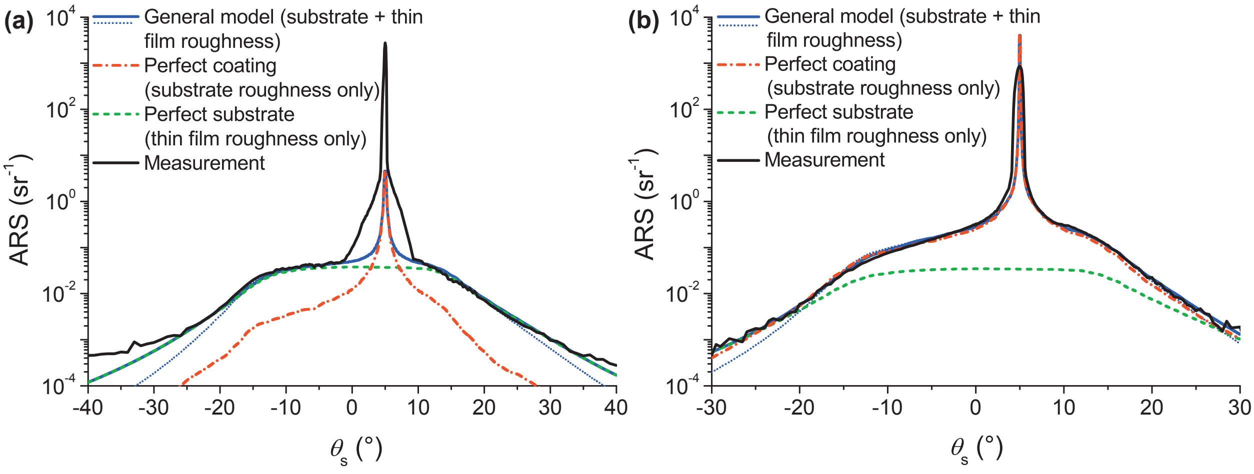

**Fig. 4.6:** Angle resolved light scattering of Mo/Si multilayer, measurement and modeling results. For all simulations, the EUV spectrum shown in Fig. 3.4b is considered. In case of the *general model*, the partial cross-correlation model (dotted blue curve) and the linear continuum cross-correlation model (solid blue curve) are used. All other simulations are based on the linear continuum cross-correlation model. **(a)** Smooth substrate (sample A); **(b)** moderately rough substrate (sample B).

The good agreement between measurements and simulations with the *general model* not only demonstrates the accuracy of the scattering measurements, but also proves the validity of the scattering theory used and corroborates the LCM. The deviations close to the specular beam of sample A can be attributed to scattered light of the beam preparation optics, as is shown in the instrument signature in Fig. 3.3. For sample B, this effect is not visible because of the higher scattering level.

With the possibility to switch off certain influencing factors in the scattering simulations, a detailed analysis of the individual scattering mechanisms can be obtained, which could otherwise not be accessed by scattering measurements on real coatings. With this additional information, it can easily be observed that the dominant scattering sources differ among both coatings. For sample A, the ARS from replicated substrate roughness is almost an order of magnitude lower than the ARS from intrinsic thin film roughness at most scattering angles, while it is exactly the opposite for sample B.

Close to the specular beam, the scattered radiation of both multilayer coatings can almost entirely be attributed to replicated substrate roughness. Hence, the imaging contrast in an optical system critically depends on the MSFR of the individual substrates.

The intrinsic thin film roughness affects large scattering angles and thus the overall scattering loss. A detailed overview of the angular ranges in which each of the two roughness components lead to scattering is illustrated in Fig. 4.7, which shows the encircled energy of the simulated ARS curves.

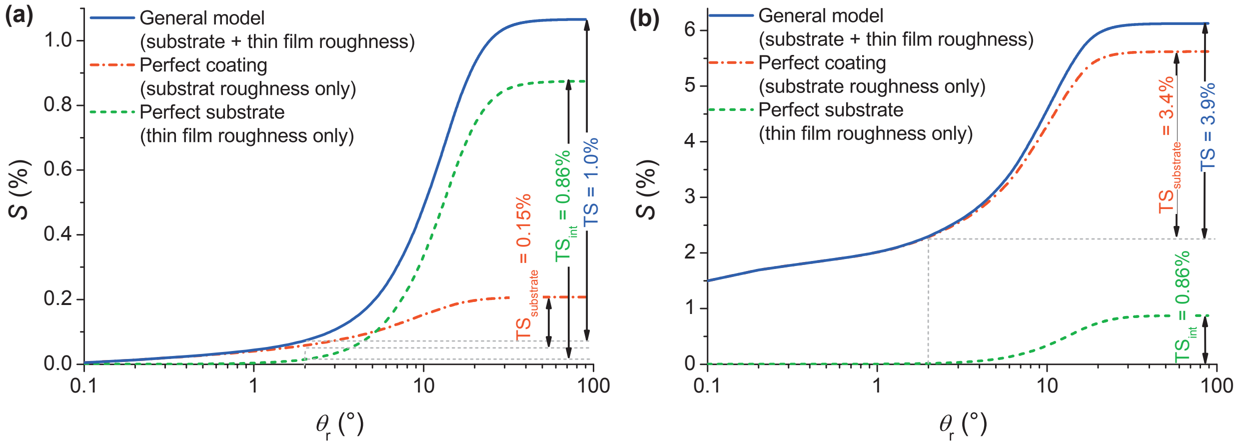

**Fig. 4.7:** Encircled scattered energy around specular reflex and scattering loss for s-polarized incident light at $\lambda = 13.5\,\mathrm{nm}$. **(a)** Smooth substrate (sample A); **(b)** moderately rough substrate (sample B).

For the multilayer design and deposition process used, the lowest achievable scattering loss is 0.86%, as is indicated by the encircled energy plot for the ideal substrate. The initial substrate roughness of sample A (HSFR = 0.08 nm) leads to an additional scattering loss of 0.15%. If the HSFR of the substrate would be 0.19 nm, the scattering loss from replicated substrate roughness is as high as from the intrinsic thin film roughness, which can be simply estimated by scaling the substrate PSD by $\mathrm{TS}_{\mathrm{int}}/\mathrm{TS}_{\mathrm{substrate}}$. Hence, in order to keep the scattering loss of EUV coatings and thus the specular reflectance at an acceptable level, the substrate roughness should be lower than this limit. Even slightly higher roughness values lead to a drastic increase in the scattering loss; for instance, for sample B, which exhibits a substrate roughness of HSFR = 0.34 nm, the TS is already 3.9%, even though the substrate roughness is partly smoothed at high spatial frequencies by the multilayer coating. However, as the results from sample A reveal, HSFR values below 0.1 nm do not lead to a significant improvement anymore and more light is scattered from the intrinsic thin film roughness. Therefore, a preferable range for the HSFR of EUV multilayer substrates is from 0.1 nm to 0.2 nm.

It is interesting to note that the scattered radiation at angles larger than 20° from the specular direction does not significantly influence the scattering loss of either sample because of the unfavorable interference conditions, in contrast to the resonant scattering at smaller scattering angles.

### 4.2.2 Roughness cross-correlation properties

Besides the pure interface roughness, the roughness cross-correlation properties are of equal importance to the overall scattering characteristics. Thus, several experimental studies have been devoted to determine the cross-correlation properties in thin film coatings.

For instance in [118], it was shown that the cross-correlation PSD of a single layer on a substrate can be ascertained from spectral reflectance and scattering measurements. Recently, another approach was presented in [174], which uses reference points applied to the substrate by a microindenter. By digitally positioning the measured topographies of the substrate and the top-surface with respect to the reference points, the same measurement area but at a different multilayer height can be analyzed. This method, however, critically relies on a non-oblique multilayer deposition. If the substrate surface is tilted with respect to the incoming particle flux, as is the case for curved sample geometries, the reference points are laterally shifted and the intended global coordinate system is lost. A further critical aspect is that an interruption of the deposition process and an exposure of the sample to air can change the thin film growth process. Therefore, the technique has only been applied to determine the cross-correlation properties between the substrate and the top-surface of the complete multilayer stack so far.

It is interesting to note that, while the knowledge about the exact location of the topography measurements becomes indispensable for the cross-correlation PSDs, this information is not critical for the determination of the interface PSDs. Therefore, along with the fact of the uniform substrate and multilayer finish, this aspect was not considered during the study of the roughness evolution of the Mo/Si multilayer coatings in Sec. 4.1.

In the following, the auto- and cross-correlation PSDs are determined from HRTEM measurements of Mo/Si multilayer cross-sections. In this way, a large number of interfaces and thus also many cross-correlation combinations can be analyzed. Furthermore, the same coordinate system for all interfaces enables the study of an oblique multilayer growth.

In Fig. 4.8a, an exemplary HRTEM image is shown. The Mo layers appear darker than the Si thin films because more electrons are scattered and do not reach the detector of the electron microscope as a result of the higher atomic number of Mo.

From the cross-section image, the individual interface profiles were extracted using the edge localization algorithm described in [175]. Even with the poor signal-to-noise ratio at the interfaces, a sub-pixel edge detection can be achieved by this algorithm. In this way, the fundamental clash of interests between: (i) a high magnification and (ii) a large field of view can be overcome. On the one hand, the image section should be large enough to enable the determination of the spatial wavelengths of interest in the range of several micrometers. On the other hand, the vertical resolution should be high enough so that the actual surface profiles, with height amplitudes of less than 1 nm, can still be resolved. The results of this analysis are presented in Fig 4.8b. In addition, in the inset, one of the profiles is displayed in more detail, which illustrates the high resolving power of the HRTEM measurements and the efficiency of the edge localization algorithm.

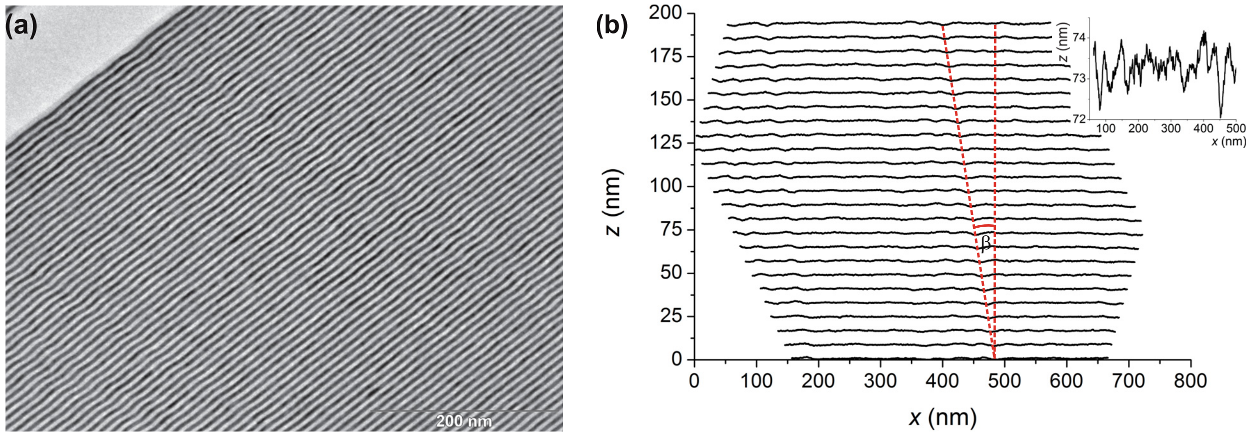

**Fig. 4.8:** Cross-sectional interface profiles of Mo/Si multilayer. **(a)** HRTEM image; the substrate, which is not shown, is oriented below the lower right corner of the figure; **(b)** extracted one-dimensional interface profiles. For clarity, only every second profile is plotted. The inset shows a zoomed view of one of the interface profiles.

From the extracted one-dimensional (1D) interface profiles, the replication of the main surface structures of the substrate through the entire multilayer stack can be clearly observed in accordance with the LCM.

The Mo/Si thin film stack was deposited under an oblique deposition angle of $\alpha = -39°$. This value can also be deduced from the angle of the propagation of small imperfections, as indicated by the red dashed lines in Fig. 4.8b ($\beta = -22°$) and the tangent rule for oblique multilayer deposition [176, 177]:

$$\tan\beta = {}^{1}\!/_{2}\tan\alpha. \tag{4.7}$$

A schematic showing the definition of the deposition and multilayer growth angle is presented in Fig. 4.9. The cross-section for the HRTEM measurements was prepared in the plane defined by the sample normal and the incoming flux direction. Therefore, a projection of the angles $\alpha$ and $\beta$ with respect to the cross-section plane does not have to be taken into account.

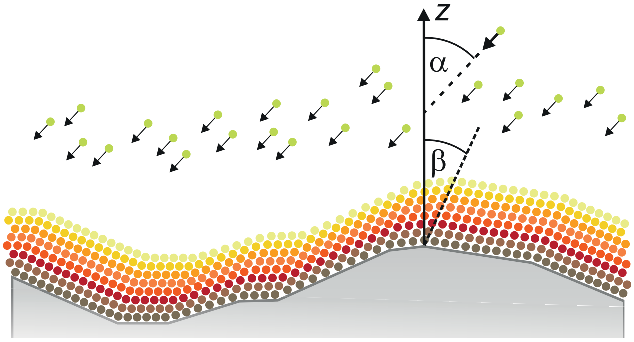

**Fig. 4.9:** Schematic of thin film deposition process under oblique incidence.

Based on the 1D interface profiles, all auto- and cross-covariance functions were calculated according to Eq. (2.5) and the corresponding 1D PSD functions were determined through Fourier transformation. Assuming an isotropic surface roughness, the 1D PSDs can then be transformed to 2D PSDs, using the inverse Abel transformation [178]:

$$\mathrm{PSD}(f) = -\frac{1}{\pi}\int_{f}^{\infty}\frac{1}{\sqrt{f_{\mathrm{x}}^{2}-f^{2}}}\frac{\mathrm{dPSD_{1D}}(f_{\mathrm{x}})}{\mathrm{d}f_{\mathrm{x}}}\mathrm{d}f_{\mathrm{x}}. \tag{4.8}$$

In a first analysis step, the shift of the individual interface profiles from the oblique multilayer deposition is compensated for in the calculations in order to focus on the principal cross-correlation properties, independently of the deposition angle. Exemplary results of these computations are shown in Fig. 4.10. Later, the oblique growth of the multilayer is considered.

Because of the limited amount of data (1D instead of 2D profiles), the PSDs exhibit strong but natural, statistical fluctuations compared to the previously presented PSDs from AFM topography measurements. Another parameter that should be kept in mind when analyzing HRTEM images is the non-infinitesimal small depth of the cross-section specimen, which leads to a depth-averaging of the interface profiles. The sample thickness is usually a few tens of nanometers, which can influence high spatial frequency components around $f_\mathrm{c} = 100\,\mu\mathrm{m}^{-1}$. However, the good agreement between the surface PSDs obtained by AFM and the HRTEM analysis in Fig. 4.10b reveals that this effect plays only a minor role and can be neglected in particular at lower spatial frequencies.

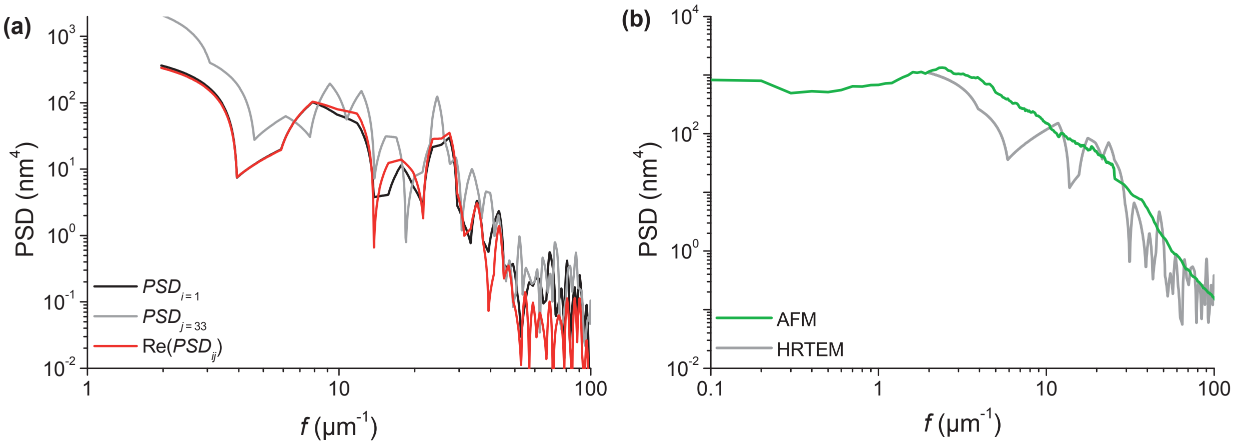

**Fig. 4.10:** PSDs retrieved from the interface profiles shown in Fig. 4.8b. **(a)** Interface and cross-correlation PSDs; **(b)** comparison to the PSD of the multilayer top-surface obtained by AFM.

The roughness enhancement with increasing number of layers, as studied in Sec. 4.1, can likewise be observed for the interface PSDs derived from the HRTEM analysis at spatial frequencies below $f = 50\,\mu\mathrm{m}^{-1}$ (see Fig. 4.10a). Above this spatial frequency, both PSDs begin to overlap, which is in agreement with the roughness evolution model and the experimental results from the periodic Mo/Si thin films.

The cross-correlation PSD almost perfectly follows the lower interface PSD up to a spatial frequency of $f \sim 60\,\mu\mathrm{m}^{-1}$, which is consistent with the partial and linear continuum cross-correlation model. Above this point, the cross-correlation PSD begins to deviate from the interface PSDs towards lower values. This is in favor of the linear continuum cross-correlation model, which predicts a rapid decay of the cross-correlation PSD at high spatial frequencies. In contrast, the partial cross-correlation model assumes that the cross-correlation PSD continues to follow the lower interface PSD. One possible explanation why the experimental cross-correlation PSD does not drop so rapidly towards zero as expected from the linear continuum cross-correlation model might be the depth averaging in the HRTEM image, which affects mainly these high spatial frequencies.

To the author's knowledge, this is the first direct experimental proof of the two cross-correlation models, in particular of the partial replication of the roughness structures in the high spatial frequency range. Also for all other cross-correlation PSDs of the multilayer stack, the partial roughness replication model approximates the experimental findings fairly well up to a spatial frequency of $f = 60\,\mu\mathrm{m}^{-1}$, as demonstrated in Fig. 4.11. Here the merit function,

$$M(i,j) = \sum_{f=2\,\mu\mathrm{m}^{-1}}^{60\,\mu\mathrm{m}^{-1}} \left|\log \mathrm{PSD}_{i,j;\,\mathrm{exp.}}(f) - \log \mathrm{PSD}_{i,j;\,\mathrm{model}}(f)\right|, \tag{4.9}$$

between the actually measured cross-correlation PSDs and different model PSDs is shown as a function of the interface index.

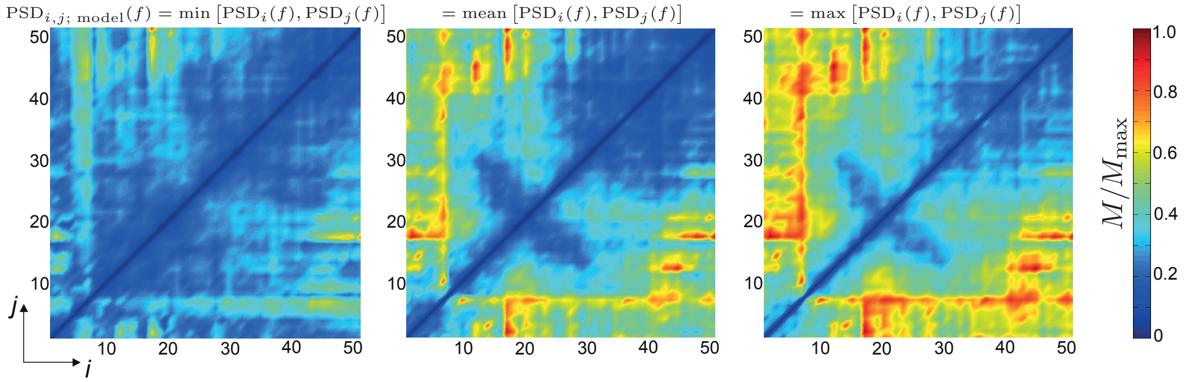

**Fig. 4.11:** Deviation between experimentally determined cross-correlation PSDs and model PSDs. All three plots are normalized to the same maximum deviation $M_{\max}$.

These plots illustrate that in particular for widely separated interfaces, a better agreement between experimental and theoretical cross-correlation PSDs can be achieved with the partial or linear continuum cross-correlation model, compared to the two other cross-correlation models. For nearby interfaces, the difference among the cross-correlation models is much less because of the small change in the interface PSDs. This is particularly true near the top-surface of the multilayer, where the relative contribution from intrinsic thin film roughness to the interface roughness becomes weaker (cf. Fig. 4.4a). Therefore, all three cross-correlation models in Fig. 4.11 exhibit only minor deviations in the top right corners of the plots.

If the oblique multilayer growth is taken into account, the individual cross-covariance functions are shifted according to the multilayer growth angle, $\beta$, and the distance between the interfaces, $z_i - z_j$. This leads to the following phase term in the cross-correlation PSDs after the Fourier transformation of the cross-covariance functions [179]:

$$\mathrm{PSD}_{i,j;\,\mathrm{oblique}}(f) = \mathrm{PSD}_{i,j;\,\mathrm{normal}}(f)\mathrm{e}^{-2\pi i f (z_i - z_j)\tan\beta\cos(\varphi_\mathrm{i}-\varphi_\mathrm{s})}. \tag{4.10}$$

Hence, the cross-correlation model used for multilayer coatings deposited under normal incidence can still be applied for scattering simulations of obliquely deposited thin films, if the correct phase terms are added. These can, however, easily be determined for all cross-correlation combinations from the multilayer design and deposition angle.

### 4.2.3 Scattering reduction through oblique multilayer deposition

There have been numerous attempts to reduce light scattering from multilayer coatings independently of their roughness properties. For instance, by changing the stationary electric field inside the multilayer stack, the electric field strength and thus the scattering at the individual interfaces can be reduced [180, 181]. In another attempt, the scattering from a substrate was successfully minimized by depositing an additional layer with an optical thickness of a quarter wavelength on the substrate [182]. In this case, the individual scattered electric fields from both interfaces interfere destructively, leading to the reduction of the scattered light. Although this technique could be applied to narrow-band filters, as described in [183], both methods require additional layers on top of the original multilayer, which impair the specular reflectance and transmittance properties.

An alternative approach, which was developed during the course of this thesis, is to modify the interference conditions for the scattered light from the individual interfaces by changing the multilayer deposition angle; as can be observed from Eq. (4.10), the skewed roughness structure does not influence the PSDs of the individual interfaces, unless the oblique deposition leads to structural differences itself. However, the cross-correlation PSDs and thus the interference conditions of the individually scattered electric fields inside the multilayer can be specifically changed by the growth angle, $\beta$, which can be used to minimize the overall scattering distribution. Hence, in contrast to the above described scattering reduction techniques, no modifications to the multilayer design or an exchange of the layer materials are required.

Previous scattering experiments on obliquely deposited thin films revealed an increase of the scattering loss for large deposition angles and characteristic arc- and lobe-shaped anisotropic scattering patterns were found [184, 185]. This could be attributed to a change from densely packed columns for thin films deposited under normal incidence to partially isolated needle-like columns for larger deposition angles. The resulting increased voids then mainly led to higher scattering levels [186]. Hence, in order to reduce the scattering from obliquely grown multilayer coatings, it is important that the individual layers do not exhibit distinct columnar structures from the oblique deposition process.

As can be observed in Fig. 4.8a, there exists no pronounced anisotropy in the HRTEM image of the obliquely deposited Mo/Si multilayer which would occur from columnar thin film growth. Because of these promising results, two Mo/Si multilayer coatings with identical design ($p = 50$, $\Gamma = 0.33 \pm 0.01$, $\Lambda = 7.03\,\mathrm{nm}$) but different depositions angles of $\alpha = 0°$ and 30° were deposited on superpolished Si-wafers. The top-surface topographies characterized by AFM revealed no significant differences between both coatings, as shown in Figs. 4.12a and b. Hence, the more favorable interference conditions of the obliquely deposited multilayer should not be compensated for by a degradation of the actual interface roughness.

In order to investigate to which extent the scattering can be reduced by the oblique multilayer deposition scheme, the scattering of the normally and obliquely deposited Mo/Si multilayers was modeled using the linear continuum cross-correlation model with the extension of the phase term according to Eq. (4.10). The necessary growth angle of $\beta = -16.1°$ was determined from Eq. (4.7) in combination with the multilayer deposition angle of $\alpha = -30°$. In Fig. 4.12c, the modeling results as well as the actual light scattering measurements at $\lambda = 13.5\,\mathrm{nm}$ are shown. It should be emphasized that the same roughness evolution was assumed for both coatings and the difference between the scattering simulations results just from the different growth angles.

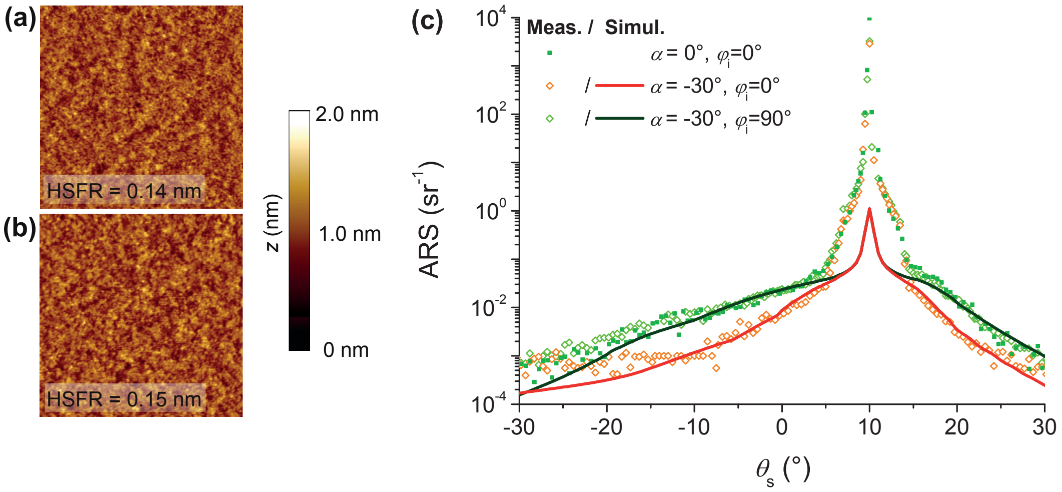

**Fig. 4.12:** Mo/Si multilayer coatings deposited under different deposition angles. **(a)** Top-surface topography (scan area: $1 \times 1\,\mu\mathrm{m}^2$) for $\alpha = 0°$ and **(b)** $\alpha = -30°$; **(c)** in-plane ARS measurements and simulations for the EUV spectrum presented in Fig. 3.4b.

Along the direction of the skewed multilayer interfaces ($\varphi_\mathrm{i} = 0°$), the ARS is significantly reduced. In contrast, if the obliquely grown multilayer is aligned perpendicular to the incidence and measurement plane ($\varphi_\mathrm{i} = 90°$), no difference can be observed to the normally deposited coating. This is expected, because in this direction the scattered light does not 'see' the oblique multilayer structure.

The reduction of the scattered light distribution, as a result of the more favorable interference conditions, is also not compensated for in other scattering directions, as is shown in the 3D scattering simulations in Figs. 4.13a and b. Here it appears as if the scattered light is simply ‘cut off’ for the obliquely deposited multilayer stack, which leads to an overall lower scattering loss.

Also the near angle scattering is minimized, as can be observed in the associated encircled scattered energy plots in Fig. 4.13c. In this diagram, further simulations for $\alpha = \pm 60°$ based on the same multilayer design and interface PSDs are included in order to demonstrate the potential of the scattering reduction technique. It should however be kept in mind that such a high deposition angle can lead to a reduction of the thin film density [187] and to a degradation of the interface roughness [188], which could outweigh the improvements in the scattering behavior.

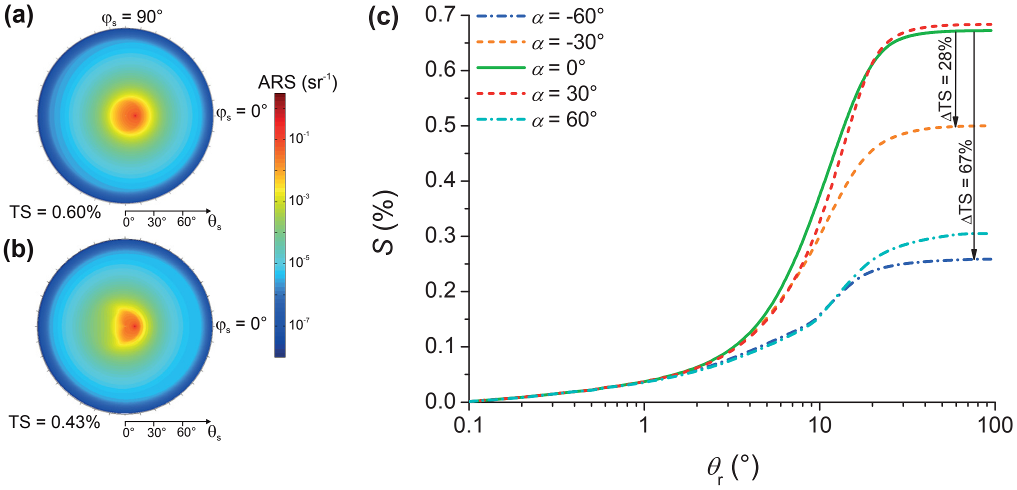

**Fig. 4.13:** 3D scattering simulation of Mo/Si multilayer for a deposition angle of **(a)** $\alpha = 0°$ and **(b)** $\alpha = -30°$ at $\lambda = 13.5\,\text{nm}$; **(c)** corresponding encircled scattered energy around specular reflex.

Because of the low substrate roughness of both coatings, the scattering distribution is mainly determined by intrinsic thin film roughness. The scattering loss of the normally deposited coating is TS = 0.61%[2]. For the deposition angles $\alpha = -30°$ and $-60°$, the overall scattering loss can be reduced by 28% and 67%, respectively. In this way, extremely low scattering losses below 0.45% can be achieved for deposition angles $\alpha < -30°$.

The interference conditions for the scattered electric fields in the multilayer stack strongly depend on the orientation of the sample. Only if the direction of the oblique multilayer structure faces towards the incident beam, the highest scattering reduction is obtained. Otherwise, it is possible that the scattering loss becomes larger for the obliquely deposited

---

[2] Compared to the previously presented Mo/Si multilayer coatings in Sec. 4.1.2, the scattering loss is slightly lower. On the one hand, this is because of the reduced number of layers ($p = 50$ instead of 60); on the other hand, this was achieved by the improved multilayer deposition parameters, as discussed at the end of Sec. 4.1.2.

multilayer than its normally deposited counterpart for small multilayer growth angles, as can be observed for $\alpha = \pm 30°$. For large deposition angles, a scattering reduction is achieved for both orientations of the sample. But also in this case, the higher scattering reduction occurs if the oblique multilayer structures face towards the incident beam.

An interesting question that still remains is whether the reduced light scattering leads to an increase of the specular reflectance. In order to answer this question without the limitation of the uncertainty in the reflectance measurements, a further Mo/Si multilayer coating with the identical design and the same deposition angle of $\alpha = -30°$ was deposited under equal deposition conditions. The substrate roughness was however increased by depositing a 70 nm thick chromium layer on the Si-wafer, which is known for its rapid increase of the high spatial frequency roughness for thin film thicknesses above 20 nm [189, 190]. The corresponding surface topographies and PSDs of the chromium layer as well as the top-surface of the multilayer coating are presented in Fig. 4.14. As expected, the Cr layer mainly enhances high spatial frequency roughness components above $f = 1\,\mu\text{m}^{-1}$. They are partly smoothed by the multilayer coating, while the roughness components below $f = 1\,\mu\text{m}^{-1}$ are enhanced by the multilayer stack.

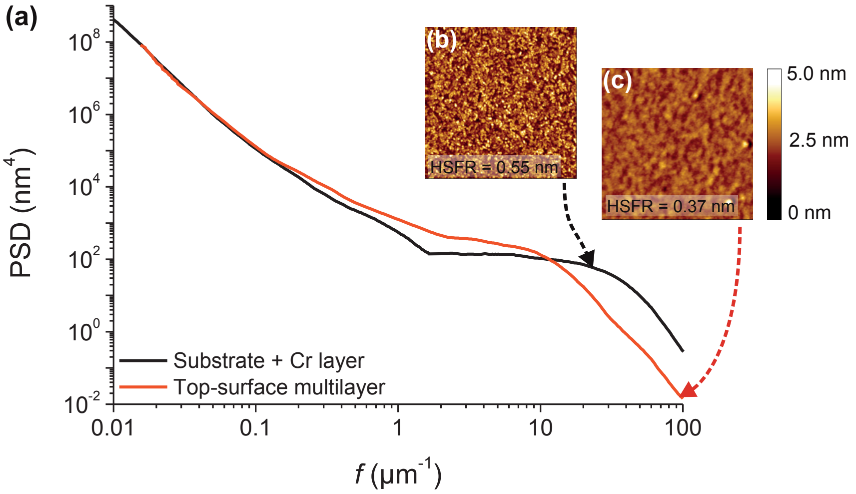

**Fig. 4.14:** Roughness evolution of obliquely deposited Mo/Si multilayer stack. **(a)** PSDs and **(b)** topography images (scan area: $1 \times 1\,\mu\text{m}^2$) obtained from AFM measurements of multilayer top-surface and **(c)** substrate after deposition of additional Cr layer.

Analogous to the previous Mo/Si multilayer coatings, ARS measurements at $\lambda = 13.5$ nm were performed under different azimuthal orientations $\varphi_\text{i}$. It turned out that while the scattering distribution is the same in the plane of incidence for $\varphi_\text{i} = 90°$ and 270°, as expected, the same relative scattering reduction as for the Mo/Si multilayer thin film without the additional Cr layer could be achieved for $\varphi_\text{i} = 0°$. In the unfavorable configuration when the oblique multilayer structure faces away from the incident beam ($\varphi_\text{i} = 180°$), also a slight increase in the ARS could be observed. These results could be precisely modeled as well, based on the PSD of the Cr layer and the LCM growth parameters obtained from the other obliquely deposited Mo/Si thin film.

The TS values of the 3D scattering simulations of the thin film coating with Cr layer are 3.0% ($\varphi_\mathrm{i} = 0°$) and 4.2% ($\varphi_\mathrm{i} = 180°$). The respective experimental in-band reflectance values between $\lambda = 13.5\,\mathrm{nm} \pm 2\%$, obtained from 100 independent measurements are $R = (54.26 \pm 0.29)\%$ ($\varphi_\mathrm{i} = 0°$) and $R = (54.32 \pm 0.30)\%$ ($\varphi_\mathrm{i} = 180°$). Although the scattering characteristics are significantly altered for these two configurations of the sample, the specular reflectance remains almost constant. From the viewpoint of the energy balance, the reduced scattered light is thus either transmitted or trapped in the multilayer coating by total internal reflection. In both cases, it will be absorbed, because of the short penetration depth of the EUV radiation. Hence, a reduction of the scattered light due to an oblique multilayer deposition does not necessarily improve the specular reflectance.

For the two Mo/Si multilayer coatings without additional Cr layer, the EUV in-band reflectances are $(58.76 \pm 0.28)\%$ for the normally and $(58.81 \pm 0.31)\%$ for the obliquely deposited thin film stacks. Thus, the oblique multilayer deposition scheme does not deteriorate the EUV reflectance either and is therefore perfectly suited to optimize the imaging properties in optical systems.

## 4.3 Summary

The roughness evolution and scattering properties of Mo/Si multilayer coatings can be precisely modeled with the LCM and first-order scattering theory. The corresponding roughness parameters of the LCM could be determined from the PSDs of the substrate and the multilayer top-surface for periodic Mo/Si multilayer coatings. By using additional single Si thin films, the growth parameters between both coating materials could also be successfully decoupled.

Furthermore, it was attempted to determine the growth parameters from single Mo thin films. However, the roughness evolution of these single layers substantially differed to the thin film growth of the Mo layers in a Mo/Si multilayer stack, which could be ascribed to a strong oxidation of the single Mo coatings.

For a Mo/Si multilayer with 60 bi-layers, the typical scattering loss, induced by intrinsic thin film roughness, is ∼0.9%. Without thin film roughness, the same scattering loss is obtained from replicated substrate roughness if the HSFR of the substrate is ∼0.2 nm. Thus, with both influencing factors, the scattering loss quickly becomes higher than 1% even for high quality substrates. For instance, a scattering loss of ∼4% was determined for a substrate roughness of HSFR = 0.34 nm. For smoother substrates with an HSFR below 0.1 nm, the total scattering does not significantly improve anymore as most of the light is scattered from intrinsic thin film roughness. Hence, a desirable range for the substrate roughness is from HSFR = 0.1 nm to 0.2 nm, which limits the scattering loss to $(1 - 2)\%$.

A new approach to even further reduce the scattering loss is possible by modifying the roughness cross-correlation properties of the multilayer stack which can be achieved by an oblique multilayer deposition. For instance, for a deposition angle of $\alpha = -30°$, the overall scattering can be reduced by 28% without any degradation of the multilayer reflectance. For larger deposition angles, the scattering reduction is even more pronounced. For instance, for a deposition angle of $\alpha = -60°$, a scattering reduction of 67% was predicted. Hence, with the oblique multilayer deposition approach, it is possible to reduce the total scattering well below 1%. The scattering reduction not only occurs at large scattering angles, but can be observed as close as 2° from the specular reflex, which is favorable for imaging optics. It is important to note that this technique is not just limited to Mo/Si multilayer coatings, but can be used to minimize light scattering from multilayer coatings for other spectral wavelengths as well.

# 5 Light scattering-based roughness characterization of substrates

In the previous chapter, it was shown that the scattering of EUV multilayer coatings critically depends on the substrate roughness, because of the replication of most of the roughness components throughout the entire multilayer stack. In order to minimize the overall scattering loss to less than 1%, the substrate roughness should approach an HSFR of 0.1 nm. While such a low substrate roughness can today be achieved on plane polished substrates, such as Si-wafers [191], this becomes a huge challenge for large-area aspherical substrates required for EUV imaging optics [56, 192, 193].

The finish characterization of these large substrates is usually accomplished by AFM. However, because of the small sampling area, only a few isolated regions of the entire sample surface can be characterized. This bears the risk that the measurement results do not resemble the actual surface finish of most of the substrate area.

A prominent example where this was the case is the second, improved projection optics set for the EUV engineering test stand – a prototype, full-field EUV lithography system – developed by collaboration between the Virtual National Laboratory (Lawrence Livermore, Sandia, and Lawrence Berkeley National Laboratories) and a consortium formed by several integrated circuit manufactures (AMD, IBM, Infineon, Intel, Micron, and Motorola) in the late 1990s and early 2000s [70, 194]. Before the actual multilayer deposition, the HSFR of the substrates of all projection optics was determined by AFM at several different positions. The HSFR values for these optics ranged from 0.17 nm to 0.24 nm, which leads to an acceptable reflectance loss of less than 2% from scattering, according to the results from the previous chapter. However, the final EUV reflectance measurements revealed an additional reflectance variation by up to 2.5% within the clear aperture on some of these optics [195]. According to Eq. (2.14), this means that the substrate roughness most likely reached an HSFR of up to 0.3 nm in these areas, which was not apparent from the isolated AFM measurements. It was thus concluded that it is essential to quantify and control the substrate finish uniformity in order to circumvent any apodization related problems in the lithographic performance in future generation lithography optics. So far, this has only been accomplished by more, closer spaced AFM measurements. However, the long measurement time of approximately 20 minutes for one AFM scan quickly limits the total number of measurements. For instance, the currently largest substrate in an EUV lithography stepper – the collector mirror close to the EUV emitting plasma source – has a diameter of more than half a meter. Even if only one representative AFM scan is performed in every $5 \times 5\,\mathrm{mm}^2$ of the substrate surface, the total AFM characterization time would be longer than half a year.

A novel approach to overcome this characterization problem is provided by angle-resolved light scattering measurements, which will be outlined in this chapter. In particular the high sensitivity towards surface imperfections and the fast data acquisition enables the characterization of such large optics in a few hours, without the need to increase the grid area [196, 197]. As will be demonstrated in Sec. 5.3.2, the lower roughness detection limit is comparable to an AFM. Moreover, vibrations of the sample under test can be easily tolerated as they do not alter the scattering direction significantly. In contrast, even small vibrations of the sample or the measurement system itself can easily limit the sensitivity of an AFM, which becomes particularly challenging for such large optics.

## 5.1 Analysis at 13.5 nm

In principle, the easiest and most natural way to characterize the substrate finish by light scattering measurements is to use the later application wavelength because then the relevant spatial frequency range for the multilayer stack is already covered during the light scattering measurements of the substrate. However, as the refractive index of all materials is close to unity at EUV wavelengths, the reflectance and thus also the scattering becomes very low for small incidence angles. For instance, the widely used substrate material Si has a refractive index of $0.9990 + 0.0018\mathrm{i}$ at $\lambda = 13.5\,\mathrm{nm}$, which leads to a reflectance of $R_0 = 1.1 \times 10^{-6}$ at $\theta_\mathrm{i} = 0^\circ$. According to Eq. (2.14), this yields an overall scattering loss of $\mathrm{TS} = 9.4 \times 10^{-9}$ for an HSFR of 0.1 nm. This is far beyond the detection limits of even synchrotron based light scattering setups [27]. Moreover, for this wavelength range, there exist no integrating spheres. Therefore, only a fraction of the TS value would be measured during an actual ARS measurement.

This situation can be relaxed by grazing incidence scattering measurements because of the total external reflectance at large incidence angles. However, because of the almost negligible refractive index contrast between the substrate and vacuum, it is possible that other scattering sources, such as subsurface damage (SSD) [14, 198–200], can have a higher impact on the scattering distribution than the actual surface roughness. This is elucidated in Fig. 5.1, which shows ARS measurements and simulations at $\lambda = 13.5\,\mathrm{nm}$ at an angle of incidence of 80° of two $\mathrm{CaF_2}$ substrates. Sample 1 was polished by a conventional polishing process, whereas a specially adapted polishing process was used for sample 2 in order to minimize SSD as much as possible. The ARS simulations are based on Eq. (2.11) and the measured surface PSDs from AFM.

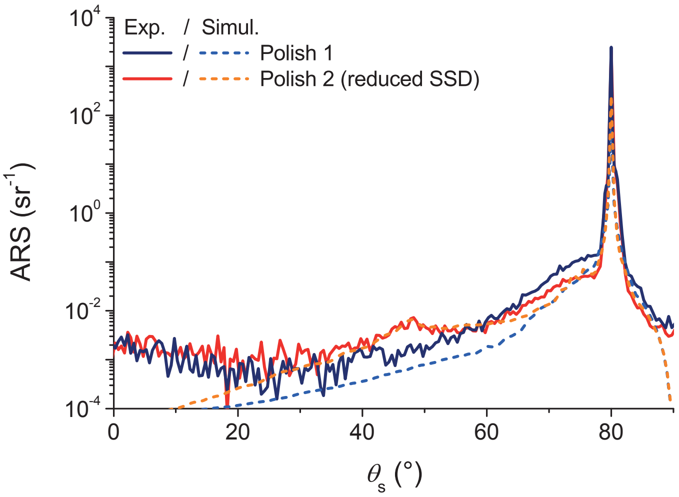

**Fig. 5.1:** ARS measurements and simulations of two differently polished $CaF_2$ substrates at $\lambda = 13.5\,\mathrm{nm}$.

For the sample with reduced SSD, a good agreement between measured and simulated ARS can be observed, indicating that the scattering distribution is primarily caused by surface roughness. However, for sample 1, the simulated roughness-induced ARS is much lower than the measured one, suggesting that the higher amount of SSD is responsible for most of the scattering distribution.

Any changes in the scattering pattern from other scattering sources, such as surface contaminations and point defects, were excluded as much as possible, by keeping both samples under equal environmental conditions at all times. During the AFM measurements, also no surface contaminations or singular defects were detected. Furthermore, in order to remove optically absorbing contaminations on the sample surface, standard ultraviolet ozone (UVO) cleaning was applied to both samples immediately before the light scattering measurements for 60 minutes. Bulk scattering can be neglected because of the short penetration depth of just 4.4 nm of the EUV radiation at this large incidence angle.

Besides the prediction of the ARS from the PSDs obtained by AFM, also the opposite way of determining the PSDs from the light scattering data was performed between $\theta_s = 40°$ and $76°$, where the scattering signal is above the electronic noise floor. The associated rms-roughness values integrated between $f_{\min} = 1\,\mu\mathrm{m}^{-1}$ and $f_{\max} = 25\,\mu\mathrm{m}^{-1}$ are 0.7 nm (sample 1) and 0.77 nm (sample 2). While the agreement with the AFM measurements in the same spatial frequency range is quite good for sample 2 ($\sigma_{\mathrm{AFM,\,sample\,2}} = 0.75\,\mathrm{nm}$), a large deviation of 75% can be observed for sample 1 ($\sigma_{\mathrm{AFM,\,sample\,1}} = 0.4\,\mathrm{nm}$). Considering that the substrate roughness of these two $CaF_2$ substrates is rather high for EUV optics, it is likely that the difference can become even larger for smoother substrates. Thus, deducing the roughness properties from EUV light scattering measurements based on Eq. (2.11) can lead to a severe overestimation of the surface roughness, in particular for the range of roughness values aspired for EUV optical components.

Another obstacle, observed during the evaluation of scattering and reflectance measurements of metal surfaces at $\lambda = 0.154\,\text{nm}$ and $4.47\,\text{nm}$ in [201–203], is the necessity to assume a gradually decreasing refractive index profile instead of a step-like boundary in order to obtain a good agreement between actual measurements and theoretical predictions. This is explained by the electron density, which diminishes gradually into the vacuum, because the conducting electrons are only loosely bound to the individual atoms. The data evaluation critically depends on the thickness of the transition layer and thus introduces further unknown parameters besides the surface roughness. Surprisingly, even for the same sample, the optimal transition layer thickness for the simulations differed by up to 40%, depending on whether reflectance or scattering measurements are used as a reference [201, 203]. Hence, these uncertainties in combination with the deviations from scattering by SSD can quickly lead to large, unacceptable errors in the determined roughness values.

## 5.2 Analysis at visible wavelengths

At visible wavelengths, the refractive index contrast between the substrate material and air is much larger than in the EUV spectral range, which leads to a pronounced roughness-induced scattering level. Even for highly polished surfaces, other scattering sources, such as SSD or bulk scattering, are much lower and require dedicated measurement schemes so that they can be observed [200, 204]. At infrared wavelengths, this trend is reversed again; for instance, at $\lambda = 1064\,\text{nm}$ and $10.6\,\mu\text{m}$, non-topographical scattering was often experienced for many solid and sputtered materials [134, 205, 206], while the scattering behavior of the same samples could be explained by just surface roughness at visible wavelengths. Thus, a preferable spectral range for the characterization of surface roughness by light scattering measurements is the visible spectral region.

This is exemplified in the following for the currently used collector mirror generation in the ASML NXE:3100 – a so called pre-production EUV lithography tool – which is already used at chipmaker's sites [82, 207, 208]. The collector mirror substrate, depicted in Fig. 5.2a, has a diameter of more than 660 mm and enables a collection solid angle of approximately 5 sr. The final collector mirror is aligned in the EUV lithography stepper such that the laser produced plasma is located in the first focus of the elliptically shaped surface. In this way, the emitted EUV light can be focused to the second, so called intermediate focus of the ellipse, from where it is relayed to the EUV mask and eventually to the wafer by further beam preparation and imaging optics [8, 209].

### 5.2.1 Measurement and modeling principles

In Fig. 5.2b, the PSDs obtained from ARS measurements at a wavelength of $\lambda = 442\,\text{nm}$ of the collector substrate, based on Eq. (2.11) and the theoretical refractive index of the substrate material, are shown. Because of the longer characterization wavelength compared to the later application wavelength, the effective spectral bandwidth of the PSDs is shifted towards smaller spatial frequencies [cf. Eq. (2.12)]. One way to minimize this effect is provided by increasing the incidence angle, which enables spatial frequencies up to $f = 4\,\mu\text{m}^{-1}$ to be characterized.

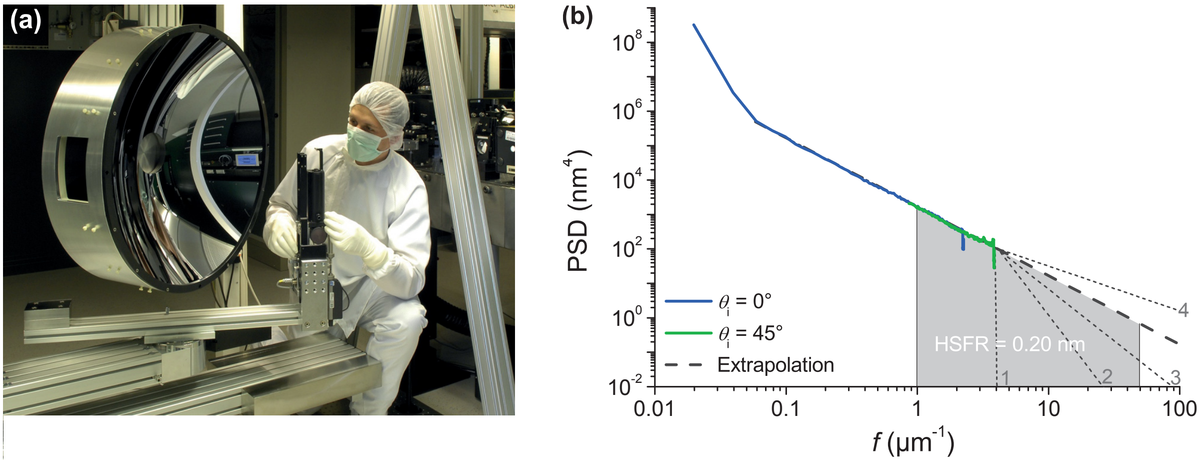

**Fig. 5.2:** Roughness characterization of EUV collector mirror substrate. **(a)** Photograph of collector substrate mounted to light scattering measurement system ALBATROSS; **(b)** data evaluation and PSDs obtained from ARS measurements at 442 nm.

As studied in [210], polished surfaces exhibit a fractal surface finish so that regardless of the magnification, the surface topography appears similar. In terms of the PSD, this scale invariance and self-similarity translates to a straight line in a double-logarithmic plot over all spatial frequencies, which can be described by an inverse power law of the form:

$$\text{PSD}(f) = \frac{\mathcal{B}}{f^{\eta}}. \tag{5.1}$$

Such a fractal behavior can also be observed for the PSDs of the collector mirror substrate; the deviation at small spatial frequencies can be attributed to the specular beam. Hence, fitting the spectral strength $\mathcal{B}$ and spectral index $\eta$ of the model PSD to the experimental PSD from the light scattering measurements allows the determination of the HSFR by extrapolation, as indicated in Fig. 5.2b. The resulting HSFR is 0.20 nm.

Of course, sub-wavelength features, albeit untypical for highly polished surfaces [178, 211], are not resolved by this technique, which can lead to deviations in the roughness values. These constraints can, however, be relaxed to a large extent because of the rapid decay of the PSD towards high spatial frequencies. Even for the unphysical case where the PSD drops directly to zero after the highest measured spatial frequency, as indicated by the dashed line (1) in Fig. 5.2b, the HSFR deviates by less than 40% to the directly extrapolated HSFR. For the other hypothetical, indicated PSDs the HSFR values are: 0.14 nm (2), 0.16 nm (3), and 0.29 nm (4), which leads to a difference of less than 45% to the fractal model PSD. These deviations strongly depend on the initial slope of the measured PSD. For this reason, a slowly decreasing PSD with a spectral index of $\eta = 2$ was chosen as an example. For a larger spectral index, the deviations would be even smaller. Moreover, instead of the instant change of the local slope of the PSD at the highest measured spatial frequency, the change would be more gradual for real surfaces, which leads to a further reduction of the differences.

In order to demonstrate the agreement of the extrapolated PSD with AFM and WLI measurements, as well as the fractal PSD course at high spatial frequencies, the surface finish of a smaller sample with a diameter of 40 mm was characterized by all three characterization techniques. The results are shown in Fig. 5.3. The sample is a single point diamond turned substrate made of an aluminum alloy that was plated with electroless nickel and subsequently polished [212–214]. Several different sample positions were characterized by all three methods.

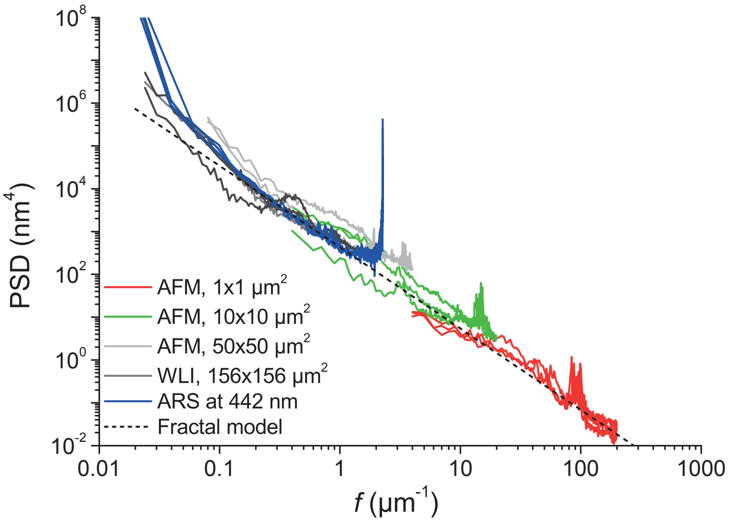

**Fig. 5.3:** PSDs of polished substrate from AFM, WLI, and ARS measurements at 442 nm.

Because of the inherent ensemble averaging within the illumination spot of typically 2 mm during the light scattering measurements, the corresponding PSDs exhibit almost no fluctuations and appear very smooth, while the individual PSDs from the AFM and the WLI measurements vary significantly among the different measurement positions.

As discussed before, the deviations at low spatial frequencies of the scattering PSDs can be attributed to the specular beam. The hook at the upper end of the PSD is caused by Rayleigh scattering from air molecules within the detector field of view, which will be addressed in more detail in Sec. 5.3.2. This hook can thus be neglected during the extrapolation. Similar spikes can be found in the PSDs from the AFM measurements in both scan areas. They result from vibrations during the measurements, which illustrates the difficulties of measuring very smooth surfaces even with moderate sample dimensions.

In principle, it is possible to extrapolate the PSDs of the WLI measurements analogously to the PSDs from the light scattering measurements, as they cover almost the same spatial frequency range. However, because of the strong fluctuations of the PSDs obtained from the WLI measurements, the fractal trend is not clearly visible without the PSDs from the other characterization techniques. In contrast, the fractal course is directly apparent in the PSDs from the light scattering measurements, which enables a robust extrapolation that agrees very well with the PSDs from the AFM measurements. The HSFR for this sample is 0.11 nm.

The fast surface roughness characterization by light scattering measurements further enables a complete mapping of the substrate surface. Hence, in contrast to a few isolated measurement positions, a complete 100% mapping of the substrate surface becomes possible. The non-contact data acquisition during the light scattering measurements also provides a large flexibility on the sample geometry and shape.

In Fig. 5.4a, the results of such a characterization are shown for the collector mirror substrate depicted in Fig. 5.2a. The HSFR map consists of more than 34 000 individual roughness measurements and enables a very detailed overview about the surface roughness; no severe defect areas and a homogeneous surface finish that improves slightly towards the inner edge of the sample can be observed. Most of the substrate surface has an HSFR of better than 0.17 nm, as demonstrated in the bar chart and corresponding cumulative roughness sum in Fig. 5.4b. Thus, according to the results from Sec. 4.2.1, the scattering loss of the final mirror should be below a TS value of 2%.

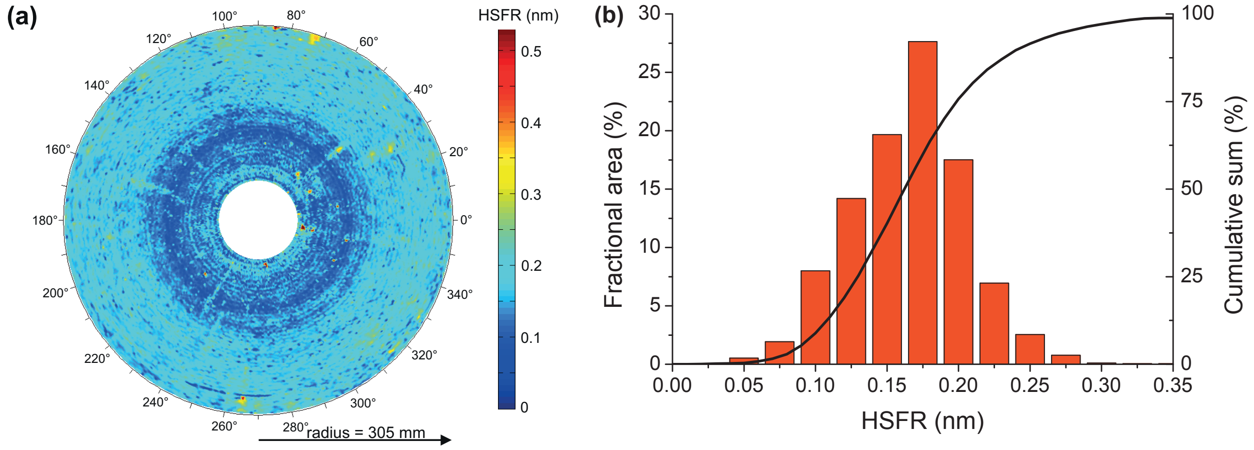

**Fig. 5.4:** Roughness characterization of EUV collector substrate. **(a)** HSFR map based on ARS measurements at $\lambda = 442\,\mathrm{nm}$; **(b)** corresponding histogram and cumulative roughness sum.

### 5.2.2 Refinement of measurement procedure

A widely used data communication technique applied in Wi-Fi systems or digital terrestrial audio and TV broadcasting (DVB-T) is orthogonal frequency-division multiplexing (OFDM) because of its high spectral efficiency and lower sensitivity to timing offsets even at high data rates [215, 216]. The basic idea of this approach is to split the communication data among several sub-carriers that have overlapping but non-interfering frequency spectra [217]. In particular the latter property is very attractive for light scattering measurements, as it enables a parallel detection of different scattering signals (various wavelengths, polarizations, or incidence angles) with just one detector at the same time.

In the following, it is described how this concept can be practically implemented for light scattering measurements by using digital lock-in amplifiers. By parallelizing the data recording, the number of different scattering angles and thus the measurement time for characterizing the surface roughness of optical components can be reduced by the reciprocal value of the parallel measurement channels. This enables the characterization of an entire collector mirror substrate in less than 6 hours based on a grid area of $5 \times 5\,\mathrm{mm}^2$, which corresponds to a measurement time of approximately 1.5 s per measurement position.

The detected signal voltage, $U$, as a function of the measurement time, $t$, of two superimposed rectangularly and periodically modulated light sources with amplitudes $A_1$ and $A_2$, different modulation frequencies, $\zeta_1$ and $\zeta_1$, as well as arbitrary phase terms, $\psi_1$ and $\psi_2$, can be described by:

$$U(t) = \frac{4A_1}{\pi} \sum_{v=1}^{\infty} \frac{\cos\left[2\pi(2v-1)\zeta_1 t + \psi_1\right]}{2v-1} + \frac{4A_2}{\pi} \sum_{w=1}^{\infty} \frac{\cos\left[2\pi(2w-1)\zeta_2 t + \psi_2\right]}{2w-1}. \tag{5.2}$$

In the following calculations, the individual phase terms are set to zero without any loss in generality, as modern dual-phase lock-in amplifiers can easily determine them by using two shifted reference signals. The demodulation itself is accomplished by multiplying $U(t)$ with an internally generated reference signal based on the modulation frequency of the light source. The lock-in signal, $\mathcal{S}(t)$, for sub-channel 1 then yields:

$$\begin{aligned} \mathcal{S}_1(t) &= U(t)\cos(2\pi\zeta_1 t) \\ &= \frac{2A_1}{\pi}\left\{1 + \cos(4\pi\zeta_1 t) + \sum_{v=2}^{\infty} \frac{\cos(4\pi v\zeta_1 t) + \cos\left[4\pi(v-1)\zeta_1 t\right]}{2v-1}\right\} \\ &\quad + \frac{2A_2}{\pi} \sum_{w=1}^{\infty} \frac{\cos\left\{2\pi\left[(2w-1)\zeta_2 - \zeta_1\right]t\right\} + \cos\left\{2\pi\left[(2w-1)\zeta_2 + \zeta_1\right]t\right\}}{2w-1}. \end{aligned} \tag{5.3}$$

Another way of looking at this formula is given by assuming that the second sub-channel resembles noise at a specific frequency. Because of the usually much lower amplitude of the noise term than the actual measurement signal, the second sum in Eq. (5.3) can then be neglected and the time-independent factor $2A_1/\pi$, which is proportional to the amplitude of the measurement channel, can be acquired by a low-pass filter. Assuming a time constant of $2\kappa$, the corresponding transfer function of a first-order low-pass filter is:

$$|H(\zeta)| = \frac{1}{\sqrt{1+(4\pi\zeta\kappa)^2}}. \tag{5.4}$$

However, in the case of two comparable signal amplitudes, the second sum in Eq. (5.3) can no longer be neglected and the low beating frequency, $\zeta_2 - \zeta_1$, between both sub-channels can lead to significant signal distortions because of the limited slope of a first-order low-pass filter. Of course, by using a higher order low-pass filter[1], these distortions can be reduced. But, this leads to an unwanted increase in the measurement time.

An alternative is provided by digital lock-in amplifiers, which use a moving average filter of duration $2\kappa$ instead of a low-pass filter [218]. The corresponding transfer function is:

$$|H(\zeta)| = \frac{\sin(4\pi\zeta\kappa)}{4\pi\zeta\kappa}, \tag{5.5}$$

which exhibits several discrete minima, as shown in Fig. 5.5a. These can be exploited to achieve a perfect attenuation of other modulation frequencies even for a low filter order. Moreover, the modulation frequencies at these minima fulfill the orthogonality condition required for the OFDM technique. Hence, by separating the individual modulation frequencies of the sub-carriers according to:

$$\zeta_2 = \zeta_1 \pm \frac{\xi}{2\kappa} \quad , \ \xi \in \mathbb{N}, \tag{5.6}$$

several parallel non-interfering measurement channels can be obtained. Furthermore, because of the small spacing between the individual optimized modulation frequencies, a large number of parallel sub-channels can be realized.

In Fig. 5.5b, measurements and simulations of the cross-talk between two sub-channels are plotted. For this experiment, the modulation frequency of the actual measurement channel (sub-carrier 1) was set to 1 kHz while a continuous frequency sweep from 100 Hz to 1.1 kHz was performed for sub-channel 2. No light was transmitted through measurement channel 1. Hence, the ideal detection signal should tend towards zero and higher measurement signals just result from cross-talk of sub-channel 2, whose light source has not been blocked during the measurements. As lock-in parameters, a moving average filter with a slope of 6 dB/oct

---

[1] A higher order filter can simply be achieved by a sequential application of a first-order filter.

and a time constant of $\kappa = 50\,\mathrm{ms}$ were used.

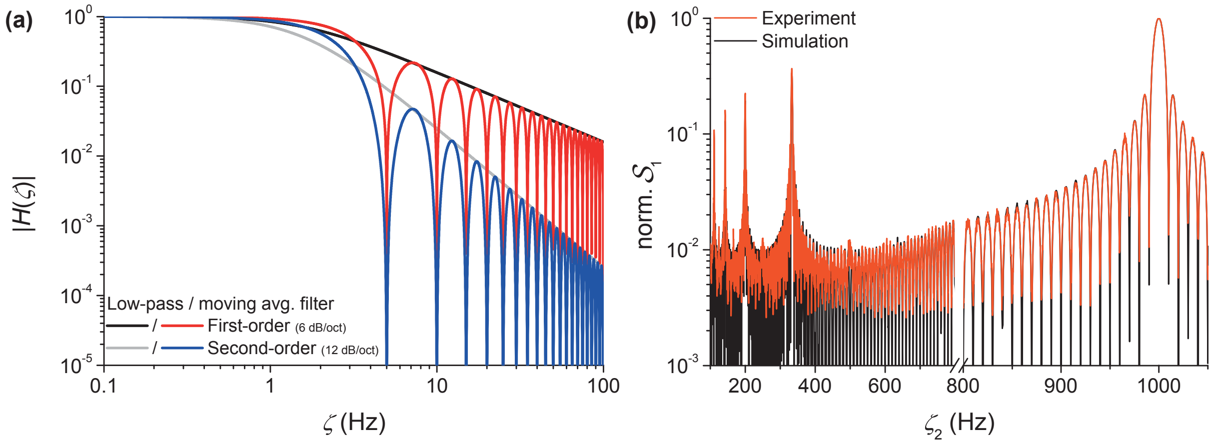

**Fig. 5.5:** Simultaneous light scattering measurements with a single detector but several channels. **(a)** Frequency response of low-pass and moving average filter; **(b)** cross-talk signal between two channels as a function of the modulation frequency ($\zeta_1 = 1000\,\mathrm{Hz}$, $A_1 = 0\,\mathrm{V}$, $A_2 = 1\,\mathrm{V}$).

At $\zeta_2 = 1\,\mathrm{kHz}$, the modulation frequency is identical with the measurement frequency, $\zeta_1$. Hence, the actual signal from sub-channel 2 is measured. The other distinctive peaks at uneven reciprocal harmonics of the frequency $\zeta_1$ result from higher orders of the rectangularly modulated sub-channel 2, which are also precisely predicted by the simulation. Similar spikes, though much lower in their peak value, can be found at the even reciprocal harmonics of $\zeta_1$ in the actual measurements, while no such peaks occur in the simulation. This slight disagreement is caused by the deviations between the experimentally modulated signal and the perfect rectangular modulation signal assumed in the simulation.

Otherwise, a good agreement between simulation and experimental results can be observed. At the orthogonal modulation frequencies, the cross-talk is drastically reduced even in close vicinity of the modulation frequency of sub-channel 1 which leads to characteristic oscillations in the entire cross-talk function. A comparison between the cross-talk and signal noise for two closely spaced orthogonal ($\zeta_1 = 1000\,\mathrm{Hz}$, $\zeta_2 = 980\,\mathrm{Hz}$) and two non-orthogonal ($\zeta_1 = 1000\,\mathrm{Hz}$, $\zeta_2 = 985\,\mathrm{Hz}$) modulation frequencies is shown in Figs. 5.6a and b. Here, the deviation between the actually measured and the ideal signal of sub-channel 1, $\mathcal{S}_{1,\mathrm{ideal}}$, which corresponds to a measurement without further sub-channels, is plotted as a function of the signal ratio between both sub-channels and different filter orders. For each data point, 100 individual measurements were performed and averaged to $\overline{\mathcal{S}}_1$. This is also considered in the simulations by assuming different timing offsets for the moving average filter.

Although the non-orthogonal and orthogonal modulation frequency pairs differ by just 5 Hz, a much lower cross-talk up to a signal ratio of 100 between both sub-channels can be achieved for the latter configuration. This upper boundary is primarily set by the limited mechanical stability of the chopper wheels utilized to modulate the two light sources. Hence, by making use of the higher modulation stability of directly power modulated light sources [219], the upper limit can still be improved.

For the non-orthogonal modulation frequencies, the maximal tolerable signal ratio is already achieved with the mechanical choppers, as demonstrated by the good agreement between the experimental results and simulations of both the cross-talk and the signal noise. Only a higher filter order improves the cross-talk behavior, which increases the measurement time. For the optimized modulation frequencies, the difference between the two filter orders is less pronounced in the cross-talk signal (see Fig. 5.6a). However, the advantages can be clearly observed in the relative standard deviation of the measurement signal in Fig. 5.6b.

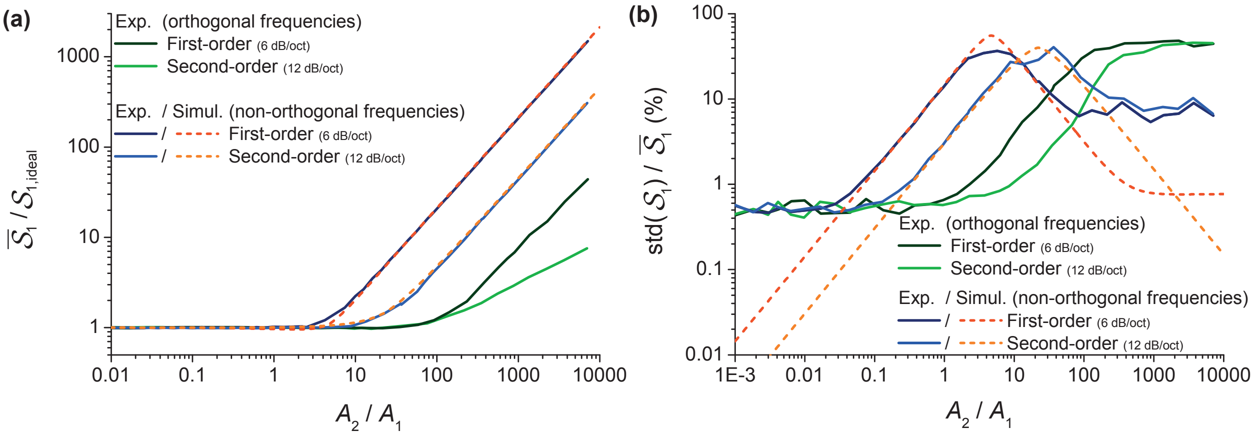

**Fig. 5.6:** Influence of filter orders and modulation frequencies on the detector signal during parallelized scattering measurements with one detector. **(a)** cross-talk and **(b)** signal noise as a function of the signal ratio of both channels ($\zeta_1 = 1000\,\mathrm{Hz}$, $\zeta_{2,\ \mathrm{non-orthogonal}} = 985\,\mathrm{Hz}$, $\zeta_{2,\ \mathrm{orthogonal}} = 980\,\mathrm{Hz}$).

The application of the OFDM measurement scheme for the characterization of a collector mirror substrate is shown in Fig. 5.7a. Here, ARS measurements at the lower ($\lambda = 405\,\mathrm{nm}$) and upper ($\lambda = 808\,\mathrm{nm}$) end of the spectral response band of the detector were performed at the same time for the two orthogonal modulation frequencies. The signal difference between both channels is less than an order of magnitude. Hence, cross-talk between the parallel measurement channels can be neglected according to the cross-talk analysis in Fig. 5.6. This is also apparent from the good agreement of both PSDs in the overlapping spatial frequency range, shown in Fig. 5.7b.

In these graphs, the spatial frequencies corresponding to the scattering angles $\theta_s = -5°$ and $-40°$ are indicated by different markers. They are equally spaced over the entire covered spatial frequency range of the PSDs and are already sufficient to deduce the fractal model

PSD. Hence, it is possible to reliably determine the HSFR of the substrate with just two detectors at fixed scattering angles and two characterization wavelengths. If required, more data points can be easily obtained by increasing the number of: (i) wavelengths and (ii) detectors without any drawbacks on the measurement time. In particular the multiplicative nature of both quantities on the total number of data points enables a fast and efficient characterization of different spatial frequencies in contrast to a sequential measurement scheme.

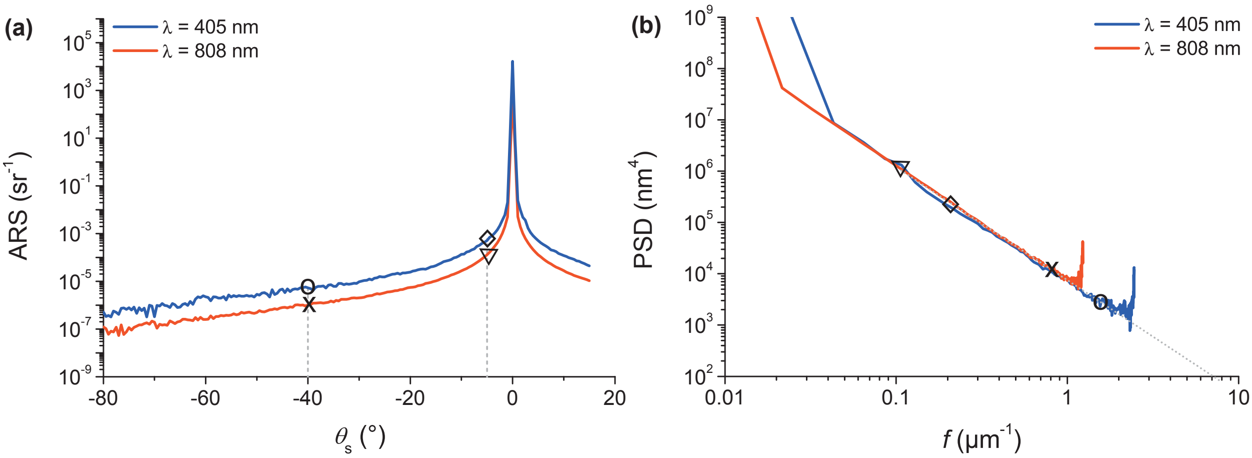

**Fig. 5.7:** Roughness characterization at two wavelengths with one detector. **(a)** ARS measurements; **(b)** corresponding PSD functions.

### 5.2.3 Prediction of EUV reflectance

Based on the detailed roughness maps of the substrate and the knowledge about the roughness evolution of the Mo/Si multilayer coatings, the next logical step is to combine this information in order to determine the scattering loss and the EUV reflectance of the final mirror prior to the coating process. This enables an early feedback during the manufacturing process and helps to reduce costs, as the substrate can be easily re-polished at this point, if the final reflectance specifications cannot be expected to be fulfilled. Furthermore, the re-polishing process can be specifically directed towards the critical sub-areas in the roughness map and does not have to be applied blindly to the entire substrate surface. Implementing the characterization technique into the manufacturing process could also substantially reduce the optimization cycles and manufacturing time [220].

In order to illustrate the prediction of the EUV reflectance, two substrates with lateral dimensions of $190 \times 220\,\mathrm{mm}^2$ were characterized by angle resolved light scattering measurements at $\lambda = 442\,\mathrm{nm}$ as described in Sec. 5.2.1. The resulting HSFR maps are shown in Fig. 5.8a. Substrate 1 exhibits a homogeneous surface finish with an average HSFR of $\sim$0.2 nm. On the second substrate, an extended defect can be observed near the lower edge. Even though the roughness is rather large at this sub-area (HSFR ∼1 nm), the course of the PSD is still perfectly fractal, as demonstrated in Fig. 5.8b. Otherwise, the remaining sample area of sample 2 exhibits a slightly worse substrate finish than sample 1, in particular in the center where HSFR values of 0.3 nm are reached.

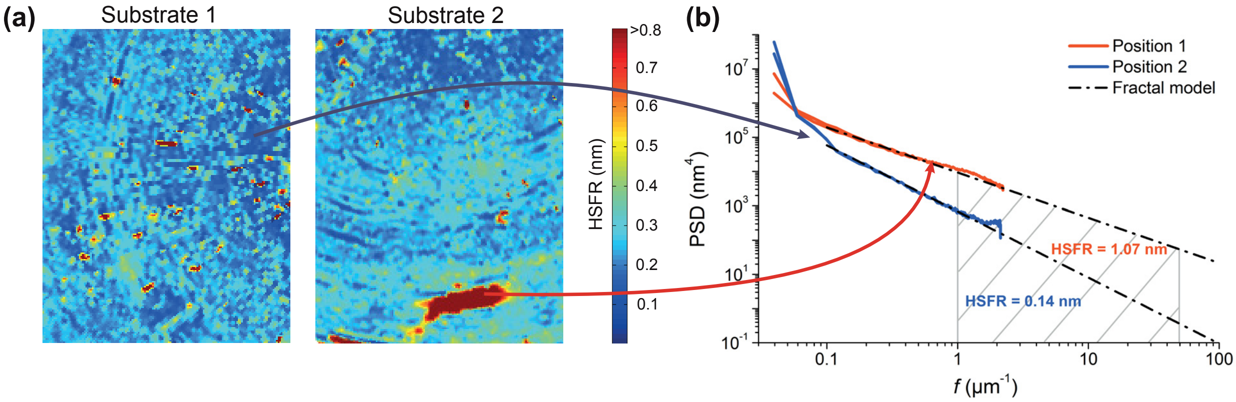

**Fig. 5.8:** Roughness characterization of two polished substrates. **(a)** HSFR map (measurement area: $190 \times 220\,\mathrm{mm}^2$) obtained from ARS measurements at $\lambda = 442\,\mathrm{nm}$; **(b)** local PSDs from rough and smooth sub-areas as indicated in the HSFR maps.

As delineated in Sec. 4.2.1, resonant scattering in Mo/Si multilayer coatings occurs primarily for scattering angles $\theta_\mathrm{r} < 30°$ which corresponds to a spatial frequency $f < 40\,\mathrm{\mu m}^{-1}$. Up to this spatial frequency, the substrate PSD is mainly replicated through the entire Mo/Si multilayer stack, and the intrinsic thin film roughness simply adds to the substrate roughness (cf. Fig. 4.4) if the substrate PSD is not too high. Thus, for a fast and easy approximation of the scattering loss of the multilayer, the contributions of both influencing factors can be treated separately. Furthermore, the scattering characteristics from the replicated substrate roughness can be approximated by a single surface which exhibits the reflectance of the thin film coating. According to Eq. (2.14), the EUV reflectance of the final mirror can then be estimated as follows:

$$R = R_0 \mathrm{e}^{-\left(\frac{4\pi \mathrm{HSFR}}{\lambda}\right)^2} - \mathrm{TS}_\mathrm{int}. \tag{5.7}$$

For rough substrates, it should be kept in mind that the substrate roughness can be partially smoothed by the multilayer coating at high spatial frequencies. Hence, Eq. (5.7) tends to overestimate the scattering loss with increasing surface roughness. However, this occurs very gradually because of the limited smoothing capabilities of the multilayer stack below $f = 40\,\mathrm{\mu m}^{-1}$ (cf. Fig. 4.5). For instance, for the rougher of the two previously analyzed Mo/Si multilayer coatings in Sec. 4.2.1, which exhibited a rather rough substrate surface (HSFR = 0.33 nm), the difference between the scattering simulation with and without any smoothing of the roughness components of the substrate is just $\Delta\mathrm{TS} = 0.36\%$ (cf. Fig. 4.7b).

If a more accurate prediction is required, the LCM in combination with first-order scattering theory can always be used.

So far, the loss in reflectance from intermixing and the native oxide layer of the uppermost layer of the thin film stack has not been taken into account in this simple reflectance model. One way to implement this is given by exchanging the theoretical reflectance, $R_0$, in Eq. (5.7) by the experimental reflectance of a reference sample, $R_{\text{ref}}$, of identical design which is preferably deposited on a superpolished Si-wafer. The scattering loss from intrinsic thin film roughness and replicated substrate roughness of the reference sample can then be compensated by:

$$R = (R_{\text{ref}} + \text{TS}_{\text{int}} + \text{TS}_{\text{substrate, ref}})\mathrm{e}^{-\left(\frac{4\pi\text{HSFR}}{\lambda}\right)^2} - \text{TS}_{\text{int}}, \tag{5.8}$$

and the values for the different TS-terms can be directly taken from Fig. 4.7a. The resulting reflectance maps at $\lambda = 13.5\,\text{nm}$, based on the HSFR maps of the two characterized substrates (see Fig. 5.8) and a reference EUV reflectance of $R_{\text{ref}} = 66\%$ from a similar Mo/Si multilayer deposited on a Si-wafer, are displayed in Fig. 5.9a. In Fig. 5.9b, also the corresponding reflectance maps after the deposition of the multilayer stack are shown, which were obtained by EUV reflectance measurements at the Bessy II electron storage ring of the Physikalisch-Technische Bundesanstalt (PTB) in Berlin [221, 222].

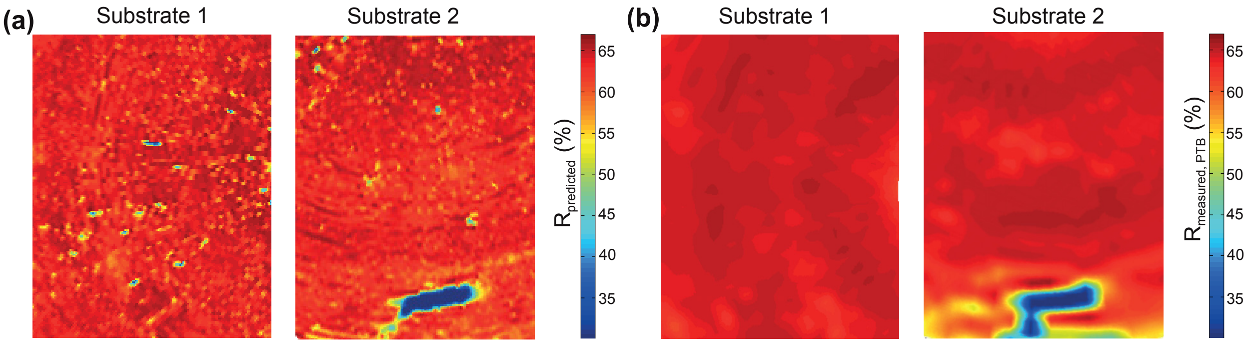

**Fig. 5.9:** EUV reflectance of Mo/Si multilayer at $\lambda = 13.5\,\text{nm}$ for s-polarized light and normal incidence. **(a)** Prediction prior to multilayer deposition based on HSFR maps presented in Fig. 5.8a; **(b)** measured reflectance at PTB, Berlin. The finer resolved structure in the predicted reflectance maps is due to the 15 times higher resolution of the HSFR maps.

The predicted EUV reflectance is in excellent agreement with the experimental results. Both the average reflectance of 65% and the severe reflectance drop of more than 40% at the extended defect area are accurately predicted. The lower reflectance in the center of sample 2 was also accurately foreseen.

Nevertheless, there are sub-areas in which the measured reflectance is lower than the predicted one, such as in the lower left corner of substrate 2. This disagreement does not necessarily need to be caused by an incorrect determination of the substrate roughness or EUV reflectance but can simply result from the processing steps and sample handling between the roughness characterization and the reflectance measurements.

## 5.3 Limitations

As an essential precondition for the light scattering based finish characterization of single surfaces, the scattered light needs to be primarily caused by surface roughness. An example, when this was not the case, was already presented in Sec. 5.1, where SSD led to an increased scattering level and thus to an overestimation of the surface roughness. Other limiting scattering sources include discrete surface defects and Rayleigh scattering from air molecules, which are discussed in more detail in the following two sections.

### 5.3.1 Light scattering from discrete defects

The scattering distribution from surface roughness is usually relatively independent of the illumination spot size once a spot diameter of 1 mm is reached so that a sufficient ensemble averaging takes place [223]. In contrast, the scattering distribution from isolated defects, such as particles, bumps, or pits, critically depends on the illumination spot size because of the limited defect dimensions; thus, by increasing the illuminated surface area, the influence of the defect on the scattering signal decreases, and vice versa.

One way to consider this effect in the scattering simulations is possible by limiting the surface area during the PSD calculation to the illumination spot size. In this manner, the already known scattering theories for surface roughness can be used, if shadowing can be neglected and if the vertical extension of the defects is small compared to the light wavelength.

Neglecting any surface roughness for the moment and approximating the defects by cylinders of height, $h_k$, which can either be positive to describe protrusions and particles, or negative in case of pits, the surface topography can be described by:

$$z(\boldsymbol{r}) = \sum_{k=1}^{\mathcal{N}} h_k \mathcal{H}\left(\rho_k - |\boldsymbol{r} - \boldsymbol{r}_k|\right), \tag{5.9}$$

where $\boldsymbol{r}_k$ is the location of the $k^{\text{th}}$ defect of radius $\rho_k$. The total number of defects is described by $\mathcal{N}$ and $\mathcal{H}$ denotes the Heaviside step function as before. For just one discrete defect, the corresponding PSD becomes [224]:

$$\mathrm{PSD}_{\text{particle}}(f) = \frac{h^2\rho^4}{\mathcal{A}} \left| \frac{J_1(2\pi f\rho)}{2\pi f\rho} \right|^2, \tag{5.10}$$

where $J_1$ is the Bessel function of the first kind and $\mathcal{A}$ the illuminated surface area.

Because of the numerous roots of the Bessel function, the angular scattering distribution exhibits distinctive oscillations, as shown in Fig. 5.10a. Although these oscillations prohibit a determination of the surface roughness, it is possible to deduce the defect radius via:

$$\rho = \frac{\omega_q}{2\pi f_q}, \tag{5.11}$$

where $\omega_q$ is the $q^{\text{th}}$ zero position of the Bessel function $J_1(\omega)$ and $f_q$ is the spatial frequency for which the minimum can be observed. In order to resolve at least one minimum in the spatial frequency range covered by the light scattering measurement, the defect radius has to be larger than $\lambda/2$.

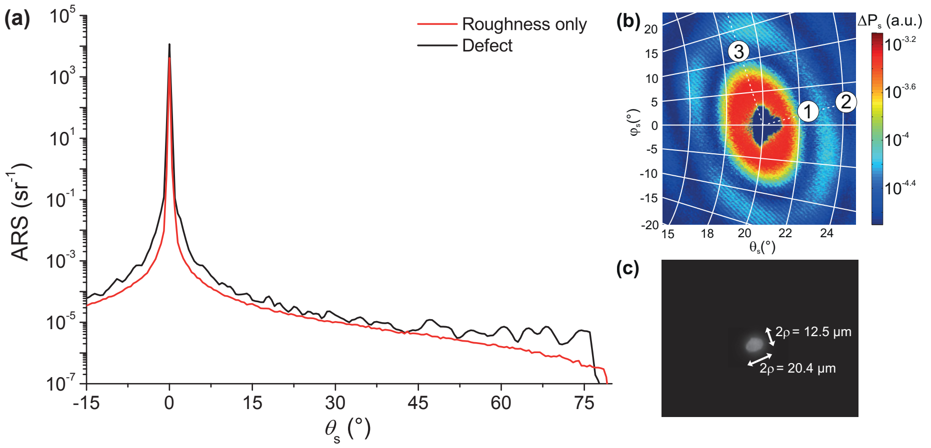

**Fig. 5.10:** Light scattering from isolated defects. **(a)** 2D-ARS of a defect-free area and a sub-area with isolated defects at $\lambda = 442\,\text{nm}$; **(b)** 3D scattering distribution of a single defect obtained by light scattering measurements with the compact roughness sensor *horos* at $\lambda = 650\,\text{nm}$. The exact angles of the marked minima are listed in table 5.1. **(c)** Differential interference contrast microscopy image (magnification: $50\times$) of the same particle [21].

By performing 3D scattering measurements, it is further possible to determine the lateral shape of the defect, as demonstrated in Fig. 5.10b. Here, the compact roughness sensor *horos* was utilized, which enables a fast determination (measurement time: $< 1\,\text{s}$) of the near specular 3D scattering distribution ($\theta_\text{r} \lesssim 5°$) at $\lambda = 650\,\text{nm}$ and a fixed incidence angle of 20° with a matrix detector. A detailed description of the sensor is given in [225].

In the scattering distribution, the oscillations caused by the defect are clearly visible as ellipses around the specular reflex and the lateral defect dimensions can simply be derived from the scattering minima.

Table 5.1 summarizes the scattering angles for the marked positions in Fig. 5.10b. According to Eq. (5.11), these minima correspond to lateral dimensions of 12.3 μm for the minor and 20.6 μm for the major defect axis. These values are in good agreement with the directly determined defect dimensions obtained from the in Fig. 5.10c depicted differential contrast microscopy image of the same defect [21].

**Table 5.1:** Defect radii determined from 3D light scattering measurements shown in Fig. 5.11b.

| position | $\theta_\mathrm{s}$ (°) | $\varphi_\mathrm{s}$ (°) | $q$ | $2\rho$ (µ$m$) |
|---|---|---|---|---|
| ① | 22.3 | 1.6 | 1 | 20.5 |
| ② | 24.2 | 2.8 | 2 | 20.6 |
| ③ | 19.2 | 10.8 | 1 | 12.3 |

For $\mathcal{N}$ arbitrary, isolated defects the PSD becomes [13]:

$$\begin{aligned}\mathrm{PSD}_{\mathcal{N}\text{-defects}}(\boldsymbol{f}) = &\sum_{k=1}^{\mathcal{N}} \frac{h_k^2\rho_k^4}{\mathcal{A}}\left|\frac{J_1(2\pi f\rho_k)}{2\pi f\rho_k}\right|^2 \\ &+ 2\sum_{k=1}^{\mathcal{N}-1}\sum_{\iota>k}^{\mathcal{N}} \frac{h_k h_\iota \rho_k^2\rho_\iota^2}{\mathcal{A}}\left|\frac{J_1(2\pi f\rho_k)}{2\pi f\rho_k}\frac{J_1(2\pi f\rho_\iota)}{2\pi f\rho_\iota}\right| \cos\left[2\pi\boldsymbol{f}(\boldsymbol{r}_k-\boldsymbol{r}_\iota)\right].\end{aligned} \tag{5.12}$$

Similar to multilayer stacks, the first term is simply the sum over all individual defects, and the second term describes the interference between them. If the radius of all defects is the same, it is still possible to deduce the defect dimension from the oscillations in the scattering distribution. However, for different defect radii, the minima become smeared out which prevents a determination of the lateral defect size.

Although not a general problem of the manufacturing process, such large amounts of isolated defects can occur in electroless nickel plated and polished metal mirrors as reported in [226, 227] or as shown in Fig. 5.11a. This fabrication process is very attractive for EUV optics [197, 228–230] as it enables a fast and economical manufacturing of large and complex shaped substrates made from aluminum alloys in combination with single point diamond turning. Because of the inherent softness of aluminum, single point diamond turned aluminum substrates can only be polished to a MSFR of ∼ 1 nm [231, 232], which would be unacceptable for EUV optics. However, by plating electroless nickel on top of the aluminum substrate, this additional layer can be polished to the required HSFR of better than 0.2 nm by conventional polishing processes [228].

The pinhole dimensions in the AFM topography image in Fig. 5.11a have a diameter of $\rho = (125 \pm 50)$ nm and a depth of typically $h \approx 50$ nm. On average, at least one pinhole is observed within a scan area of $10 \times 10\,\mu\mathrm{m}^2$. Hence, more than 30 000 pinholes influence the scattering characteristics within an illumination spot with a diameter of 2 mm.

In order to investigate the impact of these defects on the scattering distribution, the PSD according to Eq. (5.12) was calculated for different defect radii. The results are shown in Fig. 5.11b. For the positions of the individual defects, a uniform distribution was assumed. In this graph, the 2D PSDs along $f_y = 0\,\mu m^{-1}$ are plotted, as opposed to the azimuthally averaged PSDs used until now, because the PSDs become anisotropic for more than one defect.

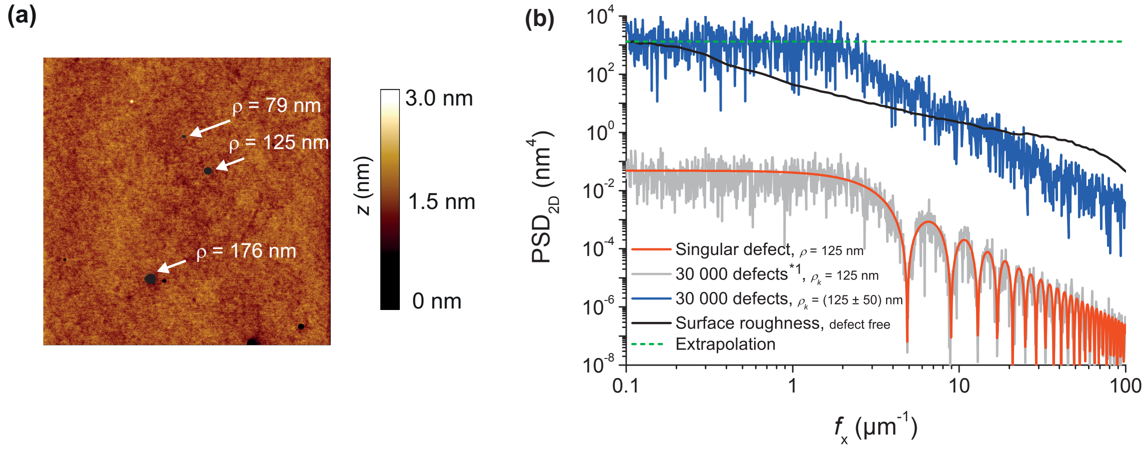

**Fig. 5.11:** Influence of defects with lateral dimensions below the characterization wavelength. **(a)** AFM image of a polished nickel-phosphorous layer on an aluminum substrate (scan area: $10 \times 10\,\mu m^2$); **(b)** PSDs of small defects in comparison to the roughness PSD from a superpolished Si-wafer with an HSFR of 0.08 nm. The defect height is 50 nm and in case of $\mathcal{N} = 30\,000$ isolated defects, a normal distribution was assumed for the defect positions and radii. The defect PSDs were all normalized to the same illumination spot size (diameter: 2 mm).$^{\star 1}$Divided by the total number of defects for a better comparison to a single isolated pit. Otherwise, the PSD would be on top of the blue curve.

For only one isolated pinhole, the defect PSD is several orders below the PSD of even a superpolished Si-wafer with an HSFR of 0.08 nm, as indicated by the red and black solid curves. Consequently, the scattering distribution is not significantly altered by just this single defect and is only determined by the surface roughness[2]. However, if the number of defects reaches the density observed in the AFM measurements of the electroless nickel surface, the defect PSD exceeds the roughness PSD at low spatial frequencies. Extrapolating the PSD from the spatial frequency range relevant for ARS measurements at visible wavelengths, as indicated by the green dashed line, thus leads to an overestimation of the HSFR, because of the low slope of the PSD. However, because of this uncommon small slope, it is possible to identify these small defects even without the observation of any oscillations in the scattering distribution so that the calculated HSFR values can be discarded.

---

[2] This discussion, of course, neglects interference between the surface roughness and the actual defect shape, which becomes important if both quantities contribute equally to the overall PSD. Nevertheless, if one of the two terms has a much lower amplitude than the other one, the interference term, as well as the lower term itself, can be neglected.

## 5.3.2 Rayleigh scattering from air molecules

Usually Rayleigh scattering from air molecules within the laser beam path is neglected at visible wavelengths because of the much higher scattering levels from surface roughness of even well-polished surfaces. However, if the HSFR approaches values of better than 0.1 nm, Rayleigh scattering from air molecules within the laser beam of the incident and reflected beam can lead to a strong increase of the measured scattering distribution. This is analyzed in the following in more detail with the aim to also identify a lower boundary for the detectable surface roughness by the light scattering based characterization approach.

As air molecules are much smaller than the characterization wavelength, they can be treated as point polarizable dipoles, which leads to the typical radiation pattern of a Hertzian dipole and a strong influence of the incident polarization on the scattered light, as shown in Fig. 5.12a. For a light path length of $l$ captured during the scattering measurements, the ARS in the plane of incidence becomes [233]:

$$\mathrm{ARS}_{\mathrm{air}} = \frac{9 l \pi^2 V_{\mathrm{air}}}{\lambda^4 k_{\mathrm{A}}} \left(\frac{\varepsilon - 1}{\varepsilon + 2}\right)^2 P \qquad \text{with } P = \begin{cases} 1 & \text{for s-polarized light} \\ \cos^2 \theta_{\mathrm{s}} & \text{for p-polarized light.} \end{cases} \tag{5.13}$$

Here, $V_{\mathrm{air}}$ denotes the molar volume of air ($V_{\mathrm{air}} = 24.06 \times 10^3\,\mathrm{cm}^3/\mathrm{mol}$ at 20°C), $k_{\mathrm{A}}$ represents the Avogadro constant, and $\varepsilon$ the relative permittivity of air.

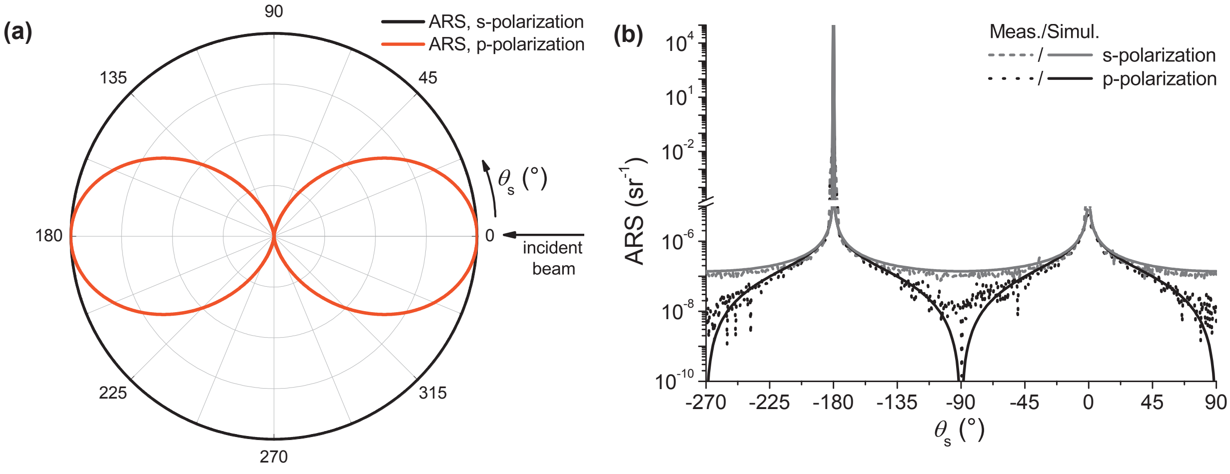

**Fig. 5.12:** Light scattering from air molecules for different polarizations in the plane of incidence. **(a)** Scattering characteristics of a single molecule; **(b)** instrument signature of the system ALBATROSS at $\lambda = 405\,\mathrm{nm}$.

Even though the detector field-of-view stays constant during an ARS measurement, the length, $l$, of the detected light beam changes with the scattering angle. For instance, if the incident light is measured, the detector ‘looks’ along the entire beam path, while in the direction perpendicular to the incident beam, the observed beam length reduces to the diameter of the detector field-of-view at the sample position, $l_{\mathrm{Det}}$. This leads to the following instrument signature [234, 235]:

$$\mathrm{ARS}_{\mathrm{Signature}} = \frac{\mathrm{ARS}_{\mathrm{air}}(l = l_{\mathrm{Det}})}{\sin\theta_s}. \tag{5.14}$$

In Fig. 5.12b, the corresponding simulation results based on the dielectric constants for air, given in [233], as well as actual measurements of the instrument signature of the system ALBATROSS at $\lambda = 405\,\mathrm{nm}$ are shown for both incidence polarizations.

The good agreement between the simulations and measurements affirms that the instrument signature is primarily caused by Rayleigh scattering from air molecules. The spike at $\theta_{\mathrm{s}} = -180°$ corresponds to the transmitted beam and the peak at $\theta_{\mathrm{s}} = 0°$ occurs when the detector 'looks' along the beam path towards the beam dump.

In principle, the signature for both incidence polarizations and thus the low-level roughness measurement capabilities can be reduced by minimizing $l_{\mathrm{Det}}$. However, the detector field-of-view has to be larger than the illumination spot at the sample so that the entire scattered light is detected [87]. In order to fulfill this requirement for large incidence angles of up to $\theta_{\mathrm{i}} = 85°$ and a beam diameter of 2 mm at the sample position, the detector field-of-view of the ALBATROSS is set to $l_{\mathrm{Det}} = 22.7\,\mathrm{mm}$. With these parameters, the lowest measurable scattering level for s-polarized incident light in the plane of incidence is $\mathrm{ARS} = 10^{-7}\,\mathrm{sr}^{-1}$. Due to the electric dipole nature of the gas molecules, the experimental instrument signature for p-polarized light is an order of magnitude lower along the direction of the introduced dipole moment near $\theta_{\mathrm{s}} = \pm 90°$. For an out-of-plane measurement configuration at $\varphi_{\mathrm{s}} = \pm 90°$, the instrument signatures simply switch between both polarizations because now the induced dipole moment becomes more favorable for s-polarized incident light.

Hence, for low-level light scattering measurements of extremely smooth samples the preferred incident polarization is parallel to the measurement plane. This is illustrated in Fig. 5.13, which shows the PSDs obtained from in-plane ARS measurements at $\lambda = 405\,\mathrm{nm}$ for s- and p-polarized light of an unstructured EUV mask.

The EUV mask blank is coated with 40 bi-layers of Mo and Si and exhibits a capping layer of ruthenium. Although this leads to an increase of the interface roughness as observed for the Mo/Si multilayer coatings studied earlier, the roughness enhancement occurs predominantly only above $f = 1\,\mu\mathrm{m}^{-1}$ (cf. Fig. 4.4a) and thus outside of the spatial frequency range covered by the light scattering measurements. In the spatial frequency range of interest for the ARS measurements, the substrate roughness is almost perfectly replicated throughout the entire multilayer stack. Hence, the HSFR of the substrate can still be determined by extrapolation even though the final multilayer stack is analyzed. In Fig. 5.13, the combined PSD from several different AFM measurements (scan areas: $1 \times 1\,\mu\mathrm{m}^2$ and $10 \times 10\,\mu\mathrm{m}^2$) of the multilayer top surface is shown as well.

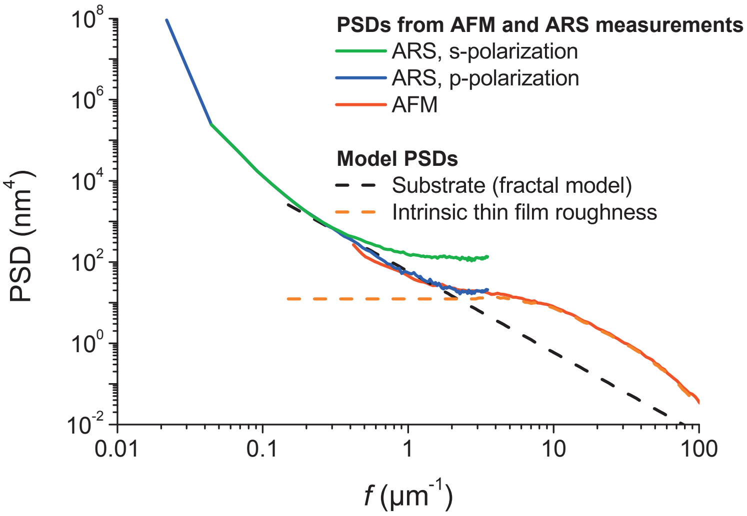

**Fig. 5.13:** PSDs from AFM and in-plane ($\varphi_\mathrm{s} = 0°$) ARS measurements at $\lambda = 405\,\mathrm{nm}$ of an unstructured, coated EUV mask blank.

While the PSDs from both ARS measurements are virtually identical at low spatial frequencies, the PSD obtained from the s-polarized ARS measurement begins to deviate from the actual surface PSD due to Rayleigh scattering from air molecules if the surface PSD falls below a value of $5 \times 10^2\,\mathrm{nm}^4$. This divergence occurs already at a spatial frequency of $f = 0.4\,\mu\mathrm{m}^{-1}$, which corresponds to a scattering angle of $\theta_\mathrm{r} = 10°$ from the specular beam. In contrast, the PSD from the p-polarized scattering measurement still follows the PSD obtained from the AFM measurements over the entire characterized spatial frequency range.

Nonetheless, it should be noted that this discrepancy between both polarizations requires an extremely smooth surface. For instance, the roughness values retrieved by integrating the scattering PSDs between $f_\mathrm{min} = 0.05\,\mu\mathrm{m}^{-1}$ and $f_\mathrm{max} = 3.5\,\mu\mathrm{m}^{-1}$ are only 0.08 nm (s-polarization) and 0.06 nm (p-polarization).

Neglecting the small tip at the very end of the PSD obtained from the p-polarized ARS measurement, which is obviously caused by the intrinsic thin film roughness of the multilayer stack, allows the PSD of the substrate at high spatial frequencies to be determined by extrapolation, as indicated by the black dashed line. The corresponding HSFR is 0.038 nm, which is not uncommon for EUV mask blanks [236].

As a comparison, the vertical instrument noise of an AFM without any lateral movement of the cantilever is between $\sigma = 0.03\,\mathrm{nm}$ and 0.04 nm [237]. Hence, characterizing the substrate prior to the coating process becomes more than challenging with an AFM, considering that even small sample vibrations can easily lead to large deviations. In contrast, during the light scattering measurements, no special attention was paid to the sample vibrations which are unavoidably caused by the fast movements of the motorized stages, particularly when scanning the sample surface.

Another perspective to look at this low surface roughness is given when considering that the fundamental building blocks of the substrate – the silicon-oxygen tetrahedron – exhibit a distance of 0.160 nm and 0.262 nm between the individual ions [238]. Hence, in order to achieve such a remarkably low surface roughness, the actual surface topography has to be very close to an atomically flat surface. This becomes even more impressive when looking at the HSFR map and the corresponding histogram in Figs. 5.14a and b, which demonstrate that this low substrate roughness has been achieved over almost the entire sample surface of $140 \times 140\,\mathrm{mm}^2$.

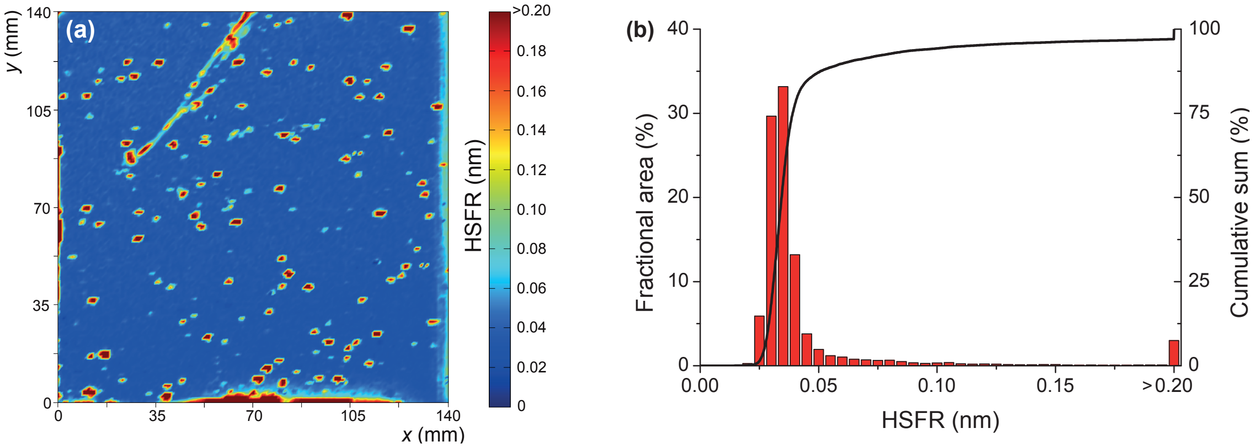

**Fig. 5.14:** Roughness characterization of EUV mask. **(a)** HSFR map obtained from ARS measurements at $\lambda = 405\,\mathrm{nm}$ and p-polarized incident light; **(b)** corresponding histogram and cumulative roughness sum.

Although the substrate characterization has been performed using the final multilayer stack, it should be noted that the same roughness sensitivity can be achieved on the uncoated substrate, because the roughness contributions from the multilayer stack occur outside the observed spatial frequency range.

## 5.4 Grating-like substrates

One of the current key challenges for EUV lithography in high-volume manufacturing is the available source power. Without a sufficient source power, the manufacturing costs per wafer are simply too high because of a low throughput. For instance, cost of ownership simulations estimate that the wafer throughput has to be at least 100 wafers per hour in order to be financially and logistically effective [239]. In contrast, the EUV pilot tools at chipmaker's sites produced only two to three wafers per hour in the last year [9].

Originally, when EUV lithography was proposed, the introduction into high-volume manufacturing was planned for feature sizes with a half-pitch of 100 nm [6]. However, because of the major advancement of optical lithography at $\lambda = 193\,\mathrm{nm}$, with the implementation of immersion lithography and double patterning [7], the insertion of EUV lithography into full-production was constantly postponed. In order to keep up with the higher printing resolution requirements of the ever decreasing semiconductor dimensions, the number of projection and illumination optics in an EUV stepper had to be increased, pushing the requirements on the source power even further [240].

At the time of writing this thesis, the envisaged half-pitch for the full-scale adoption of EUV lithography was planned beyond 22 nm [9, 239]. For an exposure throughput of 100 wafers per hour, the required average EUV source power at the intermediate focus then needs to be approximately 250 W, assuming a resist sensitivity of $15\,{}^{\mathrm{mJ}}/_{\mathrm{cm}^2}$ [241, 242]. As a comparison, the light sources for the currently used lithography wavelength 193 nm have power levels of 90 W which support the exposure of 200 wafers per hour [82].

But, even aside from this purely economic factor, it is expected that shot noise and resist performance issues will arise as the feature sizes are further decreased, which also demand for higher source powers. The same is true for the next generation EUV lithography scanner concepts that require six instead of four projection optics in order to continuously push the printing capabilities towards smaller feature sizes by increasing the numerical aperture of the projection optics [23, 24].

Nevertheless, with already five EUV pre-production tools running at chipmaker's sites [243] and the recent developments in EUV source power scaling of laser produced plasma (LPP) sources by using higher drive laser powers [244] and the introduction of preliminary prepulses for the conditioning of the target material [82, 245], the full-scale introduction of EUV lithography is more promising than ever before. So far, the highest reported EUV source powers at the intermediate focus are 70 W in a stabilized operation mode [82] and up to 200 W in a non-stabilized, open-loop configuration [243, 246]. The best suited wavelength and target material combination for a high conversion efficiency is a $CO_2$ laser operating at $\lambda = 10.6\,\mu\mathrm{m}$ and tin droplets (diameter: $20 - 30\,\mu\mathrm{m}$), respectively [247].

However, besides the required EUV light, a large amount of the drive laser radiation is reflected and scattered by the plasma. As shown in Fig. 5.15, this IR light is even better reflected by the Mo/Si multilayer coatings than the EUV light, which leads to an undesirable heating of the optics and eventually to a lower resolution. A high reflectance can also be observed between $\lambda = 100\,\mathrm{nm}$ and $400\,\mathrm{nm}$, which can influence the printing capabilities as well because of the sensitivity of EUV photo resists to this out-of-band radiation [246].

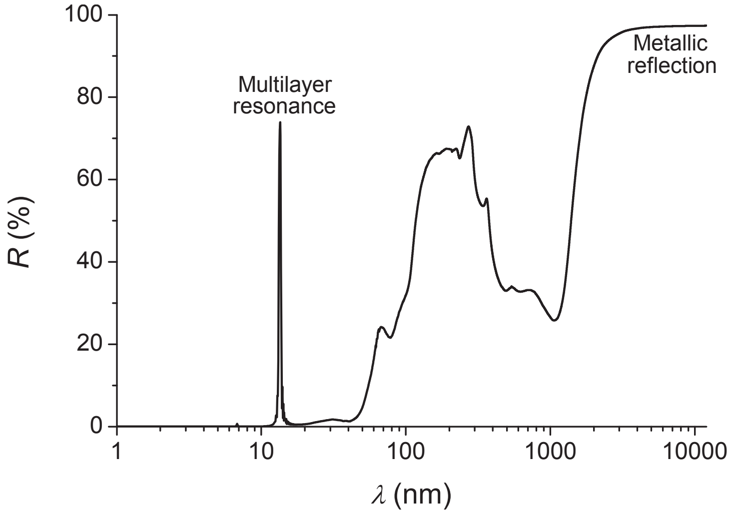

**Fig. 5.15:** Theoretical reflectance of Mo/Si multilayer without capping layer for normal incidence.

In order to suppress the unwanted out-of-band radiation, different spectral purity filters have been proposed, which include: (i) gas absorbers [248], (ii) foil filters [249], (iii) grid filters [250], (iv) anti-reflection coatings [251], (v) Si pyramids [252], and (vi) grating-like optics [197,253,254]. Among these, the latter three are very favorable because of the possibility to cool the mirror substrate so that the optic can withstand high energy loads. Furthermore, these techniques can be applied to already existing components, such as the collector mirror, which helps to keep the impact on the overall optical throughput of an EUV stepper as small as possible. In the following sections, the design, manufacturing, and characterization of grating-like substrates are discussed in more detail.

### 5.4.1 Design and manufacturing

The working principle of grating-like EUV optics is to shift the unwanted radiation out of the specular direction into higher diffraction orders so that it can be blocked by an aperture stop. A sketch of this principle is shown in Fig. 5.16a. The grating itself consists of a Mo/Si multilayer in order to obtain a high reflectance for the EUV radiation. For the IR radiation, the metallic Mo in the multilayer stack automatically leads to a high reflectance.

Using scalar diffraction theory, the diffraction efficiency of the $\mathrm{m}^{\mathrm{th}}$ order of a binary grating of height, $h_{\mathrm{g}}$, illuminated by a plane wave at normal incidence, is given by [255]:

$$R_m = R\left|\mathrm{sinc}(\pi m) + \Gamma_{\mathrm{g}}\,\mathrm{sinc}(\Gamma_{\mathrm{g}}\pi m)\left(\mathrm{e}^{\frac{4\pi \mathrm{i} h_{\mathrm{g}}}{\lambda}} - 1\right)\right|^2, \qquad (5.15)$$

where $\Gamma_\mathrm{g}$ describes the ratio between the width of the grooves and the grating period, $\Lambda_\mathrm{g}$. For the $0^\mathrm{th}$ order, Eq. (5.15) reduces to:

$$R_{m=0} = R\left\{1 + 2\Gamma_\mathrm{g}(\Gamma_\mathrm{g} - 1)\left[1 - \cos\left(\frac{4\pi h_\mathrm{g}}{\lambda}\right)\right]\right\}. \tag{5.16}$$

As can be observed from this equation, the diffraction efficiency of the $0^\mathrm{th}$ order can only be zero for $\Gamma_\mathrm{g} = 0.5$ and $h_\mathrm{g} = \lambda/4 + c\lambda/2$ $(c \in \mathbb{N})$. For this configuration, the diffraction efficiencies of all even diffraction orders become zero as well, so that the IR light is distributed among all higher uneven diffraction orders. From a practical point of view, $c$ is set to zero in order to keep the grating height as small as possible.

The direction of the individual diffraction orders is independent of the grating height, $h_\mathrm{g}$, and filling factor, $\Gamma_\mathrm{g}$, and only depends on the grating period, $\Lambda_\mathrm{g}$. On the one hand, the diffraction angle should be large so that the IR radiation can be easily blocked at the intermediate focus which requires short grating periods [$\Lambda_\mathrm{g} = {}^{m\lambda}/_{(\sin\theta_\mathrm{s} - \sin\theta_\mathrm{i})}$, cf. Eq. (2.12)]. On the other hand, the grating period should be large in order to keep the total number of grating edges on the sample surface that can impair the EUV reflectance as low as possible. A good compromise is $\Lambda_\mathrm{g} = 1\,\mathrm{mm}$, which leads to a diffraction angle of $\theta_\mathrm{s} = 0.6°$ for the first diffraction order at $\lambda = 10.6\,\mu\mathrm{m}$. This grating period also leads to almost no changes in the direction of the EUV light because the angular separation of the different diffraction orders is proportional to $\lambda/\Lambda_\mathrm{g}$, as shown in Fig. 5.16b. For these simulations, a non-commercial computer code was used which is based on the rigorous coupled wave analysis (RCWA) presented in [256]. In this way, the multilayer stack could be considered, while Eq. (5.15) is only valid for a single substrate material.

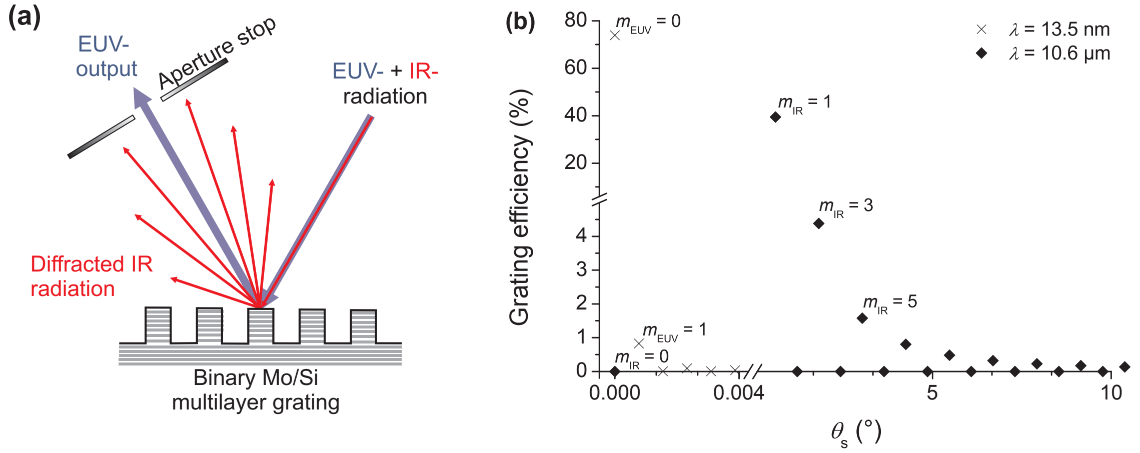

**Fig. 5.16:** Diffraction from grating-like Mo/Si multilayer. **(a)** Working principle for separating EUV and IR light; **(b)** grating efficiencies and diffraction angles for EUV and IR radiation. The grating parameters are as follows: $\Lambda_\mathrm{g} = 1\,\mathrm{mm}$, $\Gamma_\mathrm{g} = 0.5$, and $h_\mathrm{g} = 2.65\,\mu\mathrm{m}$.

The grating efficiencies for the EUV light quickly drop below 1% even for the $\pm 1^{\text{st}}$ diffraction orders. Therefore, almost the same EUV reflectance as from an unstructured substrate can be achieved. In contrast, the IR light is distributed among the higher uneven diffraction orders and can be blocked at the intermediate focus.

In a real application scenario, the varying angle of incidence on a collector mirror must be taken into account. This can be realized by adapting the grating height as a function of the collector radius so that an optical path difference of $\pi$ between the light reflected from the grooves and lands can always be ensured. But, even without any changes to the grating height, the IR light suppression still stays below 1% for incidence angles up to $\theta_{\mathrm{i}} = 20°$ as demonstrated in Fig. 5.17a, which relaxes the adaptation of the grating height for each radius.

A further aspect that has not been considered so far is the spatial and temporal coherence of the light source. At the illumination spot, the coherence length can be estimated by the relation for the radius of spatial coherence:

$$\varrho = \frac{\lambda \Delta z_{\mathrm{p}}}{D_{\mathrm{p}}}, \tag{5.17}$$

where $D_{\mathrm{p}}$ denotes the radiation source size and $\Delta z_{\mathrm{p}}$ describes the distance between the plasma and the grating. The diameter of the EUV emitting region is in the order of $D_{\mathrm{p}} = 100\,\mu\mathrm{m}$ [257] and $\Delta z_{\mathrm{p}}$ ranges from 100 mm to 200 mm [258].

As illustrated in Fig. 5.17b, the spatial coherence length for the EUV radiation is much smaller than the grating period. This destroys the EUV diffraction pattern and no diffraction losses should occur. For $\lambda = 10.6\,\mu\mathrm{m}$, the spatial coherence length is on average an order of magnitude above the grating period and thus will not degrade the diffraction pattern.

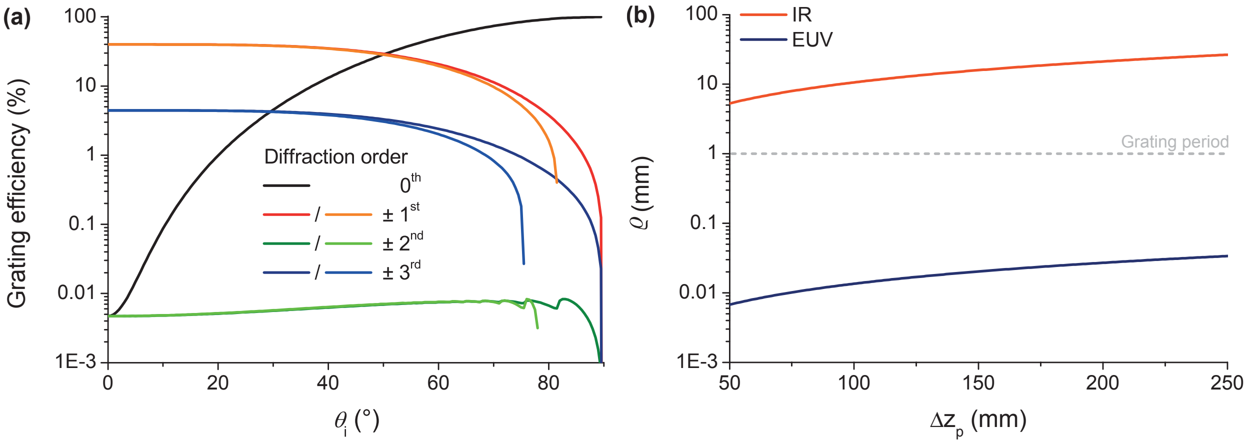

**Fig. 5.17:** Diffraction from grating-like Mo/Si multilayer. **(a)** Influence of the angle of incidence on the IR diffraction efficiency for fixed grating parameters ($h_{\mathrm{g}} = 2.65\,\mu\mathrm{m}$, $\Gamma_{\mathrm{g}} = 0.5$, $\Lambda_{\mathrm{g}} = 1\,\mathrm{mm}$); **(b)** spatial coherence as a function of the distance between the tin plasma and the grating. The assumed source size for the simulations is $D_{\mathrm{p}} = 100\,\mu\mathrm{m}$.

In principle, the structuring of Mo/Si multilayer coatings is well known from the mask manufacturing process for EUV lithography; besides the etching of thin absorber stacks on top of the multilayer stack [259–261], partly [262] and entirely [263, 264] etched Mo/Si multilayer masks have been successfully fabricated by reactive ion etching. The achieved sidewall angles of 84° – 88° [265, 266] would also be sufficient for the IR grating.

However, by simply scaling an EUV mask to the desired grating height of $h_\mathrm{g} = 2.65\,\mu\mathrm{m}$, more than 400 Mo/Si bi-layers have to be deposited, of which only the upper 60 contribute to the EUV reflectance. Unfortunately, these are the ones with the highest surface roughness because of the continuous increase in the interface roughness from intrinsic thin film roughness. For instance, the LCM predicts an HSFR of 0.36 nm after 400 bi-layers for the growth parameters of Mo and Si derived in Sec. 4.1.2. One way to avoid such rough interfaces is possible by using Si as spacing layer, which is illustrated in Fig. 5.18a. Because of the smaller growth volume of Si thin films compared to Mo layers, the HSFR at the grating ridges can then be reduced to values below 0.2 nm. At the grating grooves, an interface roughness comparable to an unstructured substrate can be achieved. Even if the top-interface is slightly degraded from the etching process, the EUV performance should not be significantly impaired because of the limited reflectance and scattering from just this single interface.

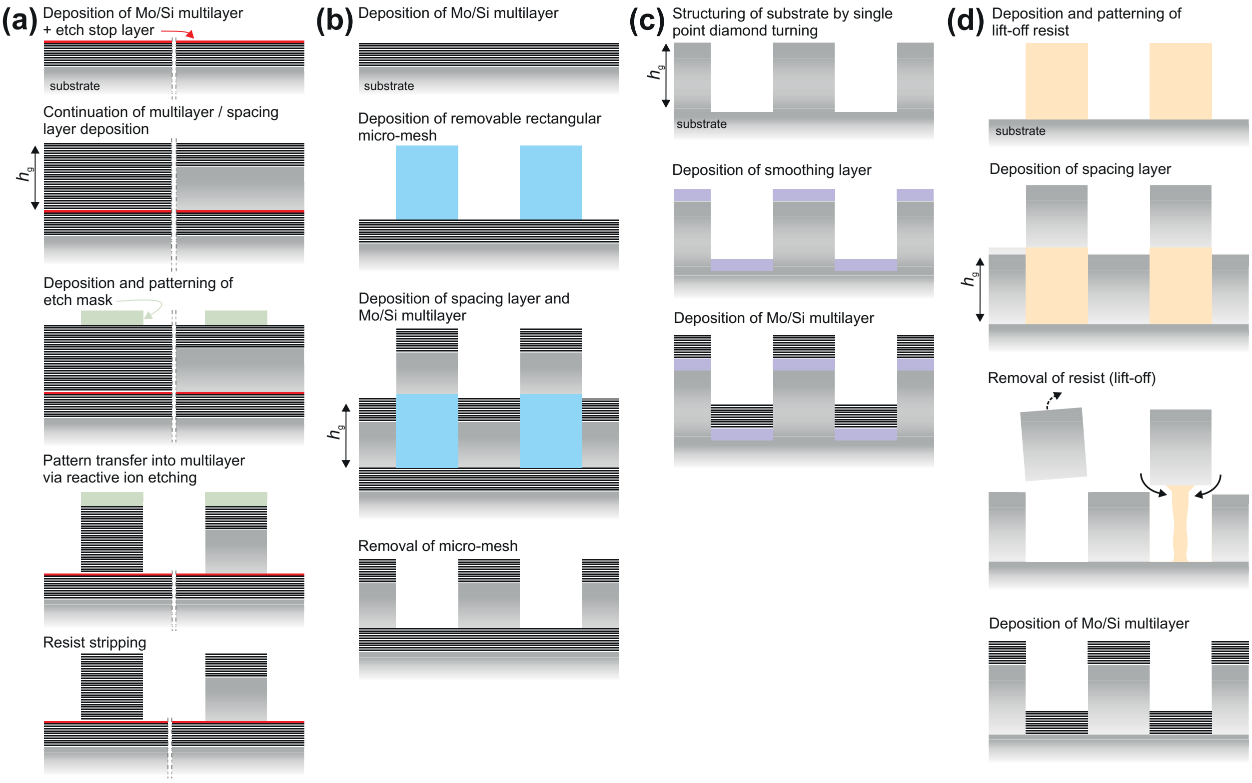

**Fig. 5.18:** Step by step process description of various structuring techniques for grating-like Mo/Si multilayer coatings. **(a)** Etching of multilayer stack; **(b)** contact mask deposition with micro-mesh; **(c)** single point diamond turning with smoothing layer; **(d)** lift-off process.

The etching reactivity in the typically used fluorine plasma is much lower for Mo than for Si [267]. Thus, the natural passivation of the Mo/Si multilayer sidewalls during the etching process is lost for just a single Si spacer layer, which can degrade the grating edges. Furthermore, because of the lower etching reactivity of Mo, the etching process most likely comes to an end at a Mo layer, despite the much smaller thickness of the Mo layers compared to the Si layers. This would lead to a severe increase of the surface roughness in the grating grooves because of the strong oxidation of Mo, as discussed in Sec. 4.1.1. However, by using an etch stop layer, this can be easily circumvented. This additional layer may also be used as a protective capping layer for the multilayer stack. Possible etch stop layer materials include boron carbide, zirconium, silicon oxynitride, nickel-iron alloy, chromium, and ruthenium [265].

Another possible structuring technique, presented in [268] and schematically depicted in Fig. 5.18b, is the use of a removable micro-mesh during the deposition process. In this way, the grating height just depends on the deposition process and the etch stop layer can be prevented. However, the 2D mesh structure leads to more grating grooves and edges then required in the plane perpendicular to the drawing.

A further approach, illustrated in Fig. 5.18c, is the structuring of the substrate surface by single point diamond turning. Because of the concentric cutting process, the technique is perfectly suited for the required circular grating on a collector mirror substrates. However, the intrinsic turning structure within the grating grooves and ridges severely degrades the EUV reflectance. One way to mitigate this effect at least for the HSFR is possible by depositing a glassy smoothing layer prior to the multilayer stack, as demonstrated in [230]. In this manner, an HSFR of ~0.2 nm can be achieved which, in combination with the standard Mo/Si multilayer stack, is fundamental for a low overall scattering loss.

Fig. 5.18d depicts how the grating-like Mo/Si multilayer can be manufactured with a standard lift-off process. The main advantage of this procedure is the low substrate roughness; in the grating grooves, the surface roughness is naturally not affected if the resist residuals can be removed entirely. At the grating ridges, a similar, low interface roughness can be achieved as it is possible with a Si spacer layer. However, a critical aspect of this pre-deposition structuring process is the smoothing and broadening of the grating edges during the multilayer deposition. Therefore, this effect is analyzed in the following in more detail, by simulating the growth of the Mo/Si multilayer stack at the grating edge based on the LCM growth parameters derived in Sec. 4.1.2. Because of the large surface slopes of the grating, a contraction length of $\delta = 0.8\,\mathrm{nm}$ per bi-layer, due to the formation of silicide interlayers between the Mo and Si layers [120], was considered in the simulations. As an initial profile for the grating, a logistic function was chosen:

$$z(x) = \frac{h_\mathrm{g}}{1 + \mathrm{e}^{\frac{-4x\tan\gamma}{h_\mathrm{g}}}}, \tag{5.18}$$

in order to avoid any singularities in the derivative of the surface profile. The grating height was set to $h_g = 2.65\,\mu\text{m}$ and a slope angle of $\gamma = 88°$ was assumed for the grating edge. The simulation results are shown in Fig. 5.19.

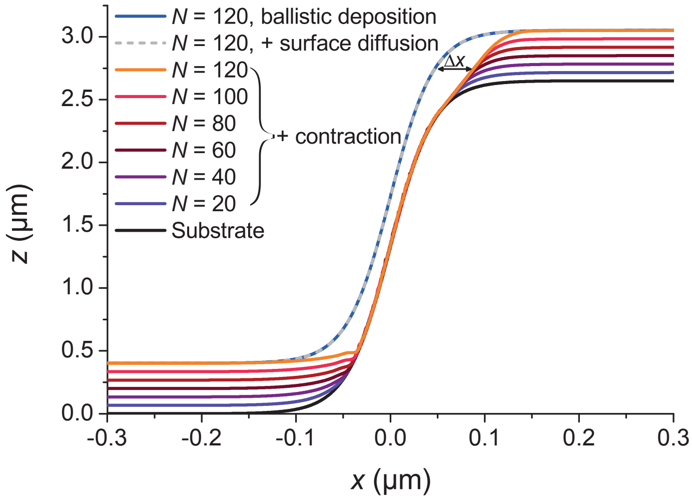

**Fig. 5.19:** Modeling of thin film growth at grating edge.

In the absence of multilayer contraction, with only surface diffusion considered, the surface profiles are not significantly changed compared to a purely ballistic deposition, as illustrated by the gray dashed and blue solid curves. In both cases, the profile is perfectly replicated except for a different height in the multilayer stack.

The same behavior can be observed at the grating ridges and grooves if the bi-layer contraction is taken into account. However, at the grating edge, it appears as if the deposition of the additional layers is directly compensated by the multilayer contraction which leads to a shift of the original grating edge by $\Delta x < 50\,\text{nm}$ after the deposition of 60 bi-layers. This is in agreement with experimental observations of HRTEM multilayer cross-section studies [268].

The fraction of the substrate area for which the multilayer is partly or entirely missing due to the multilayer contraction accounts for less than 0.04% of the sample surface. Thus, the EUV reflectance of the final multilayer should only be marginally reduced. Because of the limited contraction of the bi-layers, this effect does also not increase significantly for larger grating angles. For smaller grating angles, the multilayer contraction quickly vanishes. The almost negligible changes to the surface topography from the bi-layer contraction for smaller grating angles also justify the non-consideration of this effect during the roughness modeling.

A photograph of a test sample (diameter: 40 mm) structured by the lift-off approach and coated with a Mo/Si multilayer stack is shown in Fig. 5.20a. The coating consists of 60 bi-layers and exhibits a thin capping layer to protect the multilayer stack from the harsh EUV source environment. All layer thicknesses were optimized for an incidence angle of 20°.

In Fig. 5.20b, the corresponding grating profile, obtained from WLI measurements, is shown. As desired, the grating height is $h_\mathrm{g} = 2.65\,\mu\mathrm{m}$, the grating period is $\Lambda_\mathrm{g} = 1\,\mathrm{mm}$, and the filling factor is $\Gamma_\mathrm{g} = 0.5$.

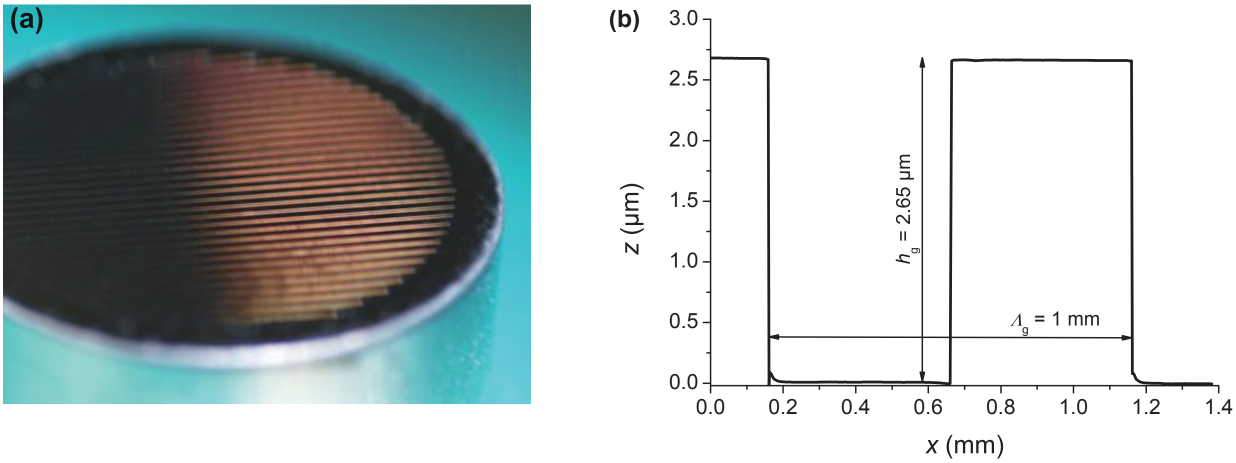

**Fig. 5.20:** Grating-like Mo/Si multilayer for suppression of IR light in laser produced EUV plasma sources. **(a)** Photograph of test sample (diameter: 40 mm); **(b)** grating profile extracted from WLI measurements.

## 5.4.2 Characterization

Only under ideal process conditions, it is possible to achieve an HSFR of 0.2 nm at the grating ridges. This already corresponds to the upper roughness boundary for which the scattering loss stays below 2% (see Sec. 4.2.1). An area covering substrate characterization thus becomes even more important than for unstructured substrates. Unfortunately, the IR grating leads to several higher-order diffraction peaks at visible wavelengths, as shown in Fig. 5.21a. This limits the applicability of first-order scattering theories for a light scattering based roughness characterization. However, as will be described in this section, this limitation can be overcome in two different ways.

The first approach is to use focused illumination; by focusing the incident beam directly onto the sample surface, instead of the detector aperture, a spot size of $\sim$100 µm can be realized at the sample surface, which is smaller than the grating period. Hence, no diffraction occurs and Eq. (2.11) can still be applied for the roughness analysis. In the second approach, no additional focusing element is used so that the illumination spot size at the sample position is larger than the grating period, which usually causes a pronounced diffraction pattern. However, if the sample or detector is rotated by 90°, so that the measurement plane is parallel to the grating grooves, no diffraction pattern is measured and the ARS is virtually identical with the ARS obtained by focused illumination, as shown in Fig. 5.21a. Hence, with both techniques the surface roughness can be determined analogously to an unstructured substrate.

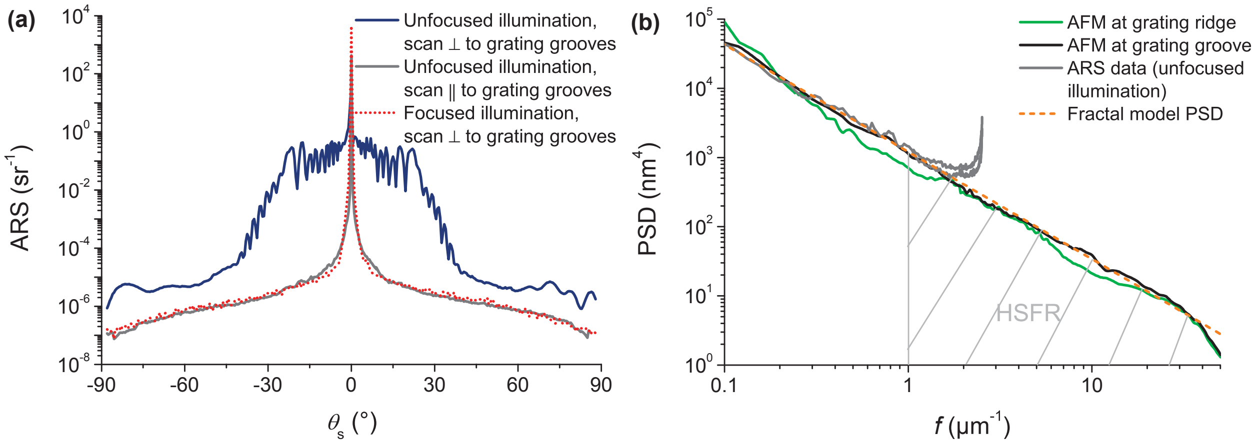

**Fig. 5.21:** Light scattering based roughness characterization of grating-like Mo/Si multilayer. **(a)** ARS measurements at $\lambda = 395\,\text{nm}$ for different orientations of the sample and illumination spot sizes; **(b)** PSDs derived from scattering data and AFM measurements.

From the scattering data, the corresponding PSDs were calculated. The results for the unfocussed illumination approach are plotted in Fig. 5.21b together with the PSDs obtained from AFM topography measurements. In the overlapping region, a good agreement between both measurement techniques, as well as the typical fractal trend, can be observed. The hook at the upper end of the scattering PSD can again be attributed to Rayleigh scattering from air. During the unfocused scattering measurements, the surface roughness from the grating grooves and ridges is averaged. Therefore, the corresponding PSD tends towards the rougher of these two areas.

With the focused illumination approach, the different grating areas can still be completely resolved, as demonstrated by the HSFR map in Fig. 5.22a.

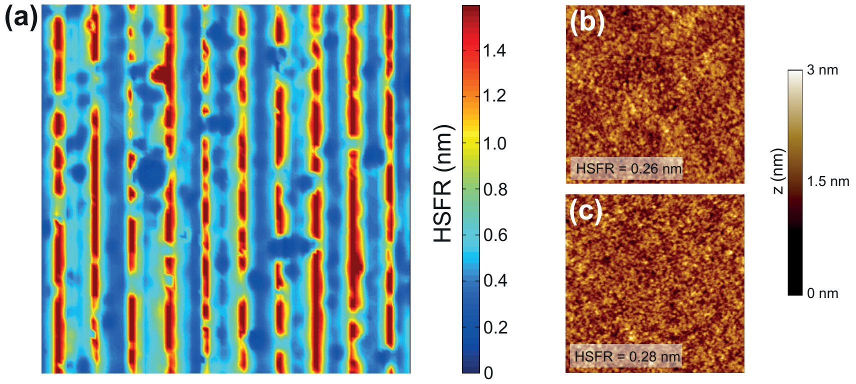

**Fig. 5.22:** Roughness characterization of structured Mo/Si multilayer coating. **(a)** HSFR map retrieved from ARS measurements at $\lambda = 395\,\text{nm}$ using focused illumination (illumination spot diameter: $\sim 100\,\mu\text{m}$); sample area: $5 \times 5\,\text{mm}^2$. **(b)** AFM topography images (scan area: $1 \times 1\,\mu\text{m}^2$) of grating ridge and **(c)** grating groove.

In the mapping, the edges of the grating are clearly visible as periodic red vertical lines. For the other areas, the HSFR values are in good agreement with the roughness values derived from the AFM measurements, shown in Figs. 5.22b and c. At the grating grooves and on the grating ridges, the surface roughness is comparable. Hence, the thick Si spacer layer for the required grating height as well as the lift-off process have not significantly altered the initial substrate roughness of the sample. Only a few sub-areas with a higher HSFR can be identified close to the grating edges in the HSFR map. Both the unfocused and focused illumination approach have also been successfully applied to large collector mirror substrates.

In Fig. 5.23, the measured diffraction efficiencies at $\lambda = 10.6\,\mu\text{m}$ of the small test sample are shown. In order to resolve the $0^{\text{th}}$ diffraction order, an out-of-plane angle of 1° was chosen. The illumination spot at the sample position was set to a diameter of 7 mm in order to irradiate several grating periods, and the detection solid angle of $2.7 \times 10^{-5}\,\text{sr}^{-1}$ was chosen such that it fits to the size of the aperture at the intermediate focus of the current EUV lithography steppers. Thus, the light observed at the $0^{\text{th}}$ diffraction order corresponds to the IR light which would actually pass the intermediate focus in a final application scenario.

Due to the low-level light scattering measurement capabilities of the ALBATROSS, diffraction orders above $m = 40$ can still be completely resolved. Although they are not of particular concern for the later application, they provide a direct feedback about the structuring process, especially the grating edges. Usually all even diffraction orders are suppressed. However, resist residuals from the lift-off process can alter the grating profile so that these diffraction orders begin to show up at high diffraction orders. The non-occurrence of this effect in the measurements, thus, corroborates the steep grating edges of the WLI measurements presented in Fig. 5.20b.

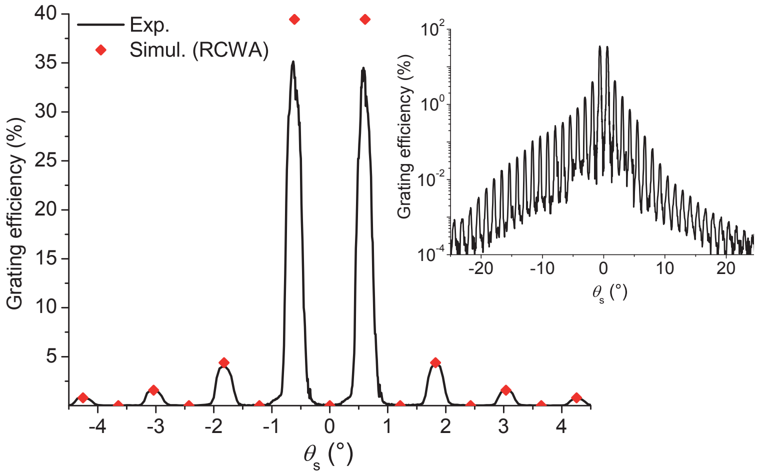

**Fig. 5.23:** Measured and simulated grating efficiencies at $\lambda = 10.6\,\mu\text{m}$. The inset shows the same measurement data on a logarithmic scale.

As shown in the inset in Fig. 5.23, the IR reflectance of the 0th diffraction order is reduced by more than three orders of magnitude compared to the reflected light from an unstructured surface. The ±1st diffraction orders exhibit a diffraction efficiency of 35.2%, which is slightly lower than the theoretically expected value of 40%. This difference might be caused by surface roughness or waviness since they have not been considered in the simulations. For higher diffraction orders, the agreement between measurements and simulations is better because the influence from interface roughness is proportional to the individual diffraction efficiencies.

Besides the angle resolved diffraction efficiency measurements, also mappings of the 0th and 1st diffraction orders were performed analogously to the roughness maps of the substrate. Over the entire structured sample, a very homogeneous diffraction efficiency could be observed with an absolute standard deviation of 0.5%, which illustrates the high precision of the structuring process over extended areas.

### 5.4.3 Influence on EUV properties

Finally, ARS measurements of the grating-like Mo/Si multilayer were performed at $\lambda = 13.5\,\text{nm}$ at an angle of incidence of 20° for two orientations of the grating in order to analyze the influence of the grating structure on the EUV performance. The results are shown in Fig. 5.24. Near the scattering angle $\theta_s = -20°$, the incident light is blocked by the channeltron, which leads to a masking of the measurement curve.

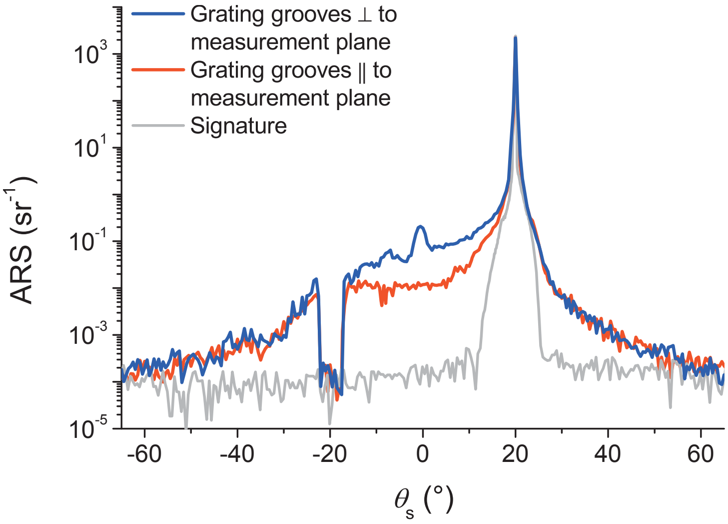

**Fig. 5.24:** ARS measurements of grating-like Mo/Si multilayer at $\lambda = 13.5\,\text{nm}$ for different orientations of the sample.

Similar to the scattering measurements at $\lambda = 395\,\text{nm}$, an enhanced scattering level can be observed if the grating ridges are aligned perpendicular to the measurement plane. However, in contrast to the ARS measurements at $\lambda = 395\,\mathrm{nm}$, this increase cannot be explained by diffraction because of the long grating period (cf. Fig. 5.16). Also, the roughness analysis in the previous section did not reveal any anisotropic surface roughness, which could explain this behavior. The higher scattering level can thus be attributed to scattering at the grating edges. Assuming an isotropic scattering distribution, the total scattering loss is TS = 2.3% and 5.6% for the parallel and perpendicular grating orientation, respectively. As the higher scattering level for the perpendicular orientation occurs most likely only in a small azimuthal scattering range, the actual scattering loss will be closer to 2.3%. This value would also be expected from the top-surface roughness (HSFR = 0.26 nm) if the multilayer stack had been deposited on an unstructured substrate (cf. Figs. 4.3 and 4.7).

Nevertheless, it seems surprising that the grating edges do not lead to higher scattering levels in particular when the strong wavelength dependence in Eq. (2.15) and the large scattering signals at $\lambda = 395\,\mathrm{nm}$ (cf. Fig. 5.21a) are considered. The two main reasons for this low scattering are: (i) the small fraction of the actual grating edge area compared to the overall surface area and (ii) the circumstance that the multilayer design at the non-perfect grating edges, with side slope angles $< 90°$, is not optimized for the local incidence angle of other than 20°. Hence, in contrast to the grating ridges and grooves, the reflectance and scattering from the grating edges is considerably reduced.

In order to determine the overall scattering loss from the non-perfect grating edges, the EUV reflectance of the test sample was measured with the instrument MERLIN at an angle of incidence of 20°. The obtained in-band reflectance between $\lambda = 13.5\,\mathrm{nm} \pm 2\%$ is $(53.0 \pm 0.3)\%$. Taking into account the scattering loss from the substrate and the intrinsic thin film roughness of 2.3% yields a difference of 3.2% to the theoretically expected in-band reflectance of the multilayer ($R_0$ ~58.5%)[3]. Part of this loss can be attributed to the silicide interlayer formation between Mo and Si. Hence, with a grating-like collector mirror, an EUV transmittance of $> 94.3\%$ compared to an unstructured surface can be realized. Such a high EUV transmittance whilst achieving a low IR transmittance (IR-suppression factor ~1000) has not been reported from other spectral filtering approaches, which usually reach out-of-band reduction factors near 10 and an EUV transmittance well below 90% [248, 249, 251, 252, 269].

These encouraging results have also led to the idea of combining two binary gratings on the collector substrate in order to achieve a dual-wavelength spectral purity filter. In this way, the pre-pulse radiation at $\lambda = 1064\,\mathrm{nm}$, which is used to condition the tin droplets in EUV LPP light sources, can be filtered in the same way as the radiation from the main $CO_2$ laser [270].

---

[3] Compared to the reflectance of a classical Mo/Si multilayer, this slightly lower reflectance is caused by the strong absorption in the capping layer.

## 5.5 Summary

The manufacturing of high quality multilayer coatings for $\lambda = 13.5\,\mathrm{nm}$ critically relies on a low substrate roughness because of the replication of most of the roughness features throughout the entire multilayer stack. By using angle resolved light scattering measurements at visible or UV wavelengths, it is possible to retrieve a thorough and detailed characterization of the surface roughness and defects. The roughness sensitivity thereby reaches values below $\mathrm{HSFR} = 0.04\,\mathrm{nm}$, which is comparable to the noise limit of an AFM. Furthermore, by applying the light scattering based characterization approach to large surfaces, area covering roughness maps of the entire sample surface can be derived that cannot be retrieved to such an extent from other high resolution characterization techniques because of the limited sampling area.

The shifted spatial frequency range in the PSDs obtained from the light scattering measurements, due to the use of a longer characterization wavelength than the actual application wavelength, is compensated by the use of a fractal PSD model, which is typical for polished surfaces. It is important to note that although the characterization approach was only demonstrated for EUV collector mirror substrates and EUV masks, the concept can also be applied to other samples and different spatial frequency ranges.

In principle, the used scattering theory is valid for arbitrary wavelengths as long as $\sigma \ll \lambda$ and can be applied at $\lambda = 13.5\,\mathrm{nm}$ in order to circumvent the shift in the covered spatial frequency range. However, the small difference in the refractive index between the substrate material and air leads to a very low roughness-induced scattering level, so that other scattering sources can become more pronounced. For instance, it was shown that SSD can lead to a much higher scattering distribution even for rough surfaces in terms of EUV optics ($\mathrm{HSFR} = 0.48\,\mathrm{nm}$).

# 6 Beyond EUV lithography – reflective coatings for 6.x nm

The persistent adherence to Moore's law implies the same continuous improvement on the lithography process in the future. For instance, the next planned scaling options for EUV lithography include multiple patterning and higher numerical apertures [9]. But, even beyond this, the traditional approach of reducing the lithography wavelength is already actively pursued, particularly in the research areas regarding new coating designs and plasma sources.

Currently, the most promising wavelength for the next lithography generation is $\lambda = 6.\text{x}\,\text{nm}$. The undefined decimal place results from the necessity to match possible source emission spectra with the multilayer reflectance and resist sensitivity. Compared to the reduction factor of >14 for the transition from $\lambda = 193\,\text{nm}$ to 13.5 nm, the wavelength reduction to $\lambda = 6.\text{x}\,\text{nm}$ almost seems marginal. However, this decision is primarily driven by the choice of high reflective multilayer coatings; at $\lambda \sim 6\,\text{nm}$, it is still possible to achieve similar theoretical peak reflectances near normal incidence as can be obtained at $\lambda = 13.5\,\text{nm}$. But, for smaller wavelengths, such as the water window between $\lambda = 2.3\,\text{nm}$ and 4.4 nm, the maximum theoretical reflectance quickly drops below 40% [34].

So far, the highest reported experimental reflectances at $\lambda = 6.\text{x}\,\text{nm}$ achieve only 60% of the theoretically predicted reflectance values at best [271–275]. Hence, there still exists a lot of room for improvement. The last three sections of this thesis are thus dedicated to the study of the roughness evolution and associated scattering properties of multilayer coatings for $\lambda = 6.\text{x}\,\text{nm}$ in order to determine to which extent light scattering can explain these large losses.

## 6.1 Background and overview

The strong absorption of silicon below the L-absorption edge at $\lambda = 12.4\,\text{nm}$ requires a different spacer material than Si for thin film coatings at $\lambda = 6.\text{x}\,\text{nm}$. The next suitable material is boron, which has a K-absorption edge at $\lambda = 6.6\,\text{nm}$, or a boron rich material such as boron carbide. A matching, high plasma emission between $\lambda = 6.5\,\text{nm}$ and 6.7 nm can be achieved from excited ions of the rare earth elements gadolinium and terbium, as demonstrated by first proof-of-principle experiments on solid targets [32, 276, 277]. Therefore, current experimental studies on multilayer coatings focus in particular on the wavelength 6.7 nm as the most probable lithography wavelength after $\lambda = 13.5\,\text{nm}$.

The necessary refractive index change between the spacer and absorber material can still be achieved with Mo. From a roughness point of view, Mo is suited as well since the required layer thickness is below the amorphous-to-crystalline transition thickness of 2 nm so that smooth interfaces can be achieved [275]. In combination with $B_4C$, the theoretical multilayer reflectance for an incidence angle of 5° is $R_0$ ~51% at $\lambda = 6.7\,\text{nm}$. Higher peak reflectances of ~57% and ~69% can be achieved by using ruthenium and lanthanum as absorber materials, respectively. Therefore, the following sections focus in particular on these two absorber materials.

In principal, the reflectance could still be increased if boron is used as spacer material. However, experimental studies [278] revealed a low density of the B thin films, which is ascribed to voids and cracks. These defects not only make the thin films very prone to oxidation but can increase the surface roughness as well.

The difference in the refractive index between the spacer and absorber materials at $\lambda = 6.7\,\text{nm}$ is smaller than between Mo and Si at $\lambda = 13.5\,\text{nm}$, which requires more bi-layers ($N \sim 400$) to achieve a high reflectance. Hence, the control of the interface roughness, periodicity, and layer thickness becomes even more crucial for a successful implementation than at $\lambda = 13.5\,\text{nm}$.

The large number of bi-layers also drastically reduces the spectral bandwidth of the coating. Therefore, the actual optical throughput of a single reflective multilayer at $\lambda = 6.7\,\text{nm}$ is lower by a factor of ~6 compared to a standard Mo/Si multilayer stack at $\lambda = 13.5\,\text{nm}$ even though the peak reflectances do not differ significantly among both coatings.

Initial studies on the roughness and reflectance properties of multilayer coatings for $\lambda = 6.7\,\text{nm}$ [35, 271, 279, 280] just simply connected the experimental reflectance values to an average interface roughness of the multilayer stack, assuming the same interface roughness for all boundaries and a perfect correlation for the interference conditions. However, as already observed during the analysis of the Mo/Si multilayer coatings in Sec. 4.1.2, this is not necessarily fulfilled, in particular at high spatial frequencies. This makes a study of the roughness evolution indispensable for a correct estimation of the scattering losses. Furthermore, the experimental reflectance values not only depend on the roughness properties but they are also influenced by the diffuseness of the interfaces due to intermixing between the layer materials. Hence, if the surface roughness is determined from just reflectance measurements, the latter effect is neglected which leads to an overestimation of the roughness properties. Interlayer diffuseness, on the other hand, cannot cause scattering. Thus, with the analysis of the light scattering properties, the influence of both properties can be distinguished.

## 6.2 Roughness analysis

The La/B$_4$C and Ru/B$_4$C coatings for the study of the roughness evolution were deposited by magnetron sputtering at the optical coatings department of the Fraunhofer IOF. In order to enable the characterization of different intermediate interfaces of the multilayer stacks, the deposition process was interrupted after 50, 100, and 200 bi-layers for the La based thin film coatings, whereas 200 bi-layers were deposited for the Ru based multilayer. The layer period and thickness ratio for all coatings, as determined from grazing incidence x-ray reflectance measurements at $\lambda = 0.154\,\text{nm}$, are $\Lambda = 3.38\,\text{nm}$ and $\Gamma = 0.4$. Exemplary AFM topography measurements before and after the multilayer deposition are shown in Fig. 6.1.

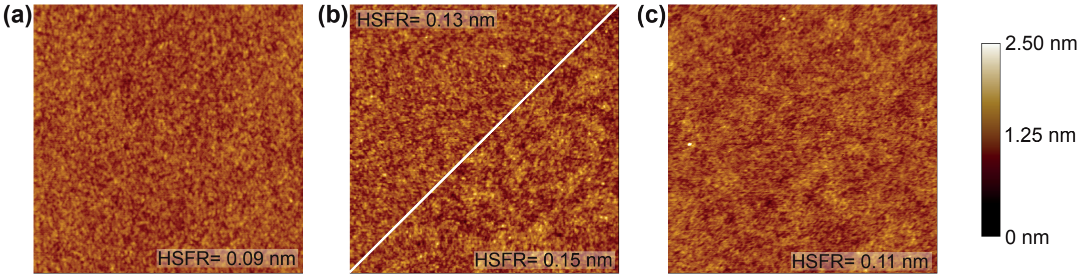

**Fig. 6.1:** AFM topography measurements (scan area: $1 \times 1\,\mu\text{m}^2$) before and after coating. **(a)** Substrate and **(b)** top-surface topographies of La/B$_4$C multilayer after 50 bi-layers (upper left half) and after 200 bi-layers (lower right half), as well as **(c)** Ru/B$_4$C multilayer after 200 bi-layers.

In comparison to the surface topographies of the Mo/Si multilayer coatings (cf. Fig. 4.3), the increase in the surface roughness is very low for both types of coatings. For the Ru-based multilayer, the increase in surface roughness is just $\Delta\text{HSFR} = 0.02\,\text{nm}$ after 400 layers while it is slightly higher ($\Delta\text{HSFR} = 0.06\,\text{nm}$) for the La-based multilayer after the same amount of layers. However, it still remains below the roughness increase of the Mo/Si multilayer coatings which exhibited a $\Delta$HSFR of 0.13 nm for just 120 layers. The combined PSDs of the multilayer coatings from several different scan areas and locations are plotted in Fig. 6.2.

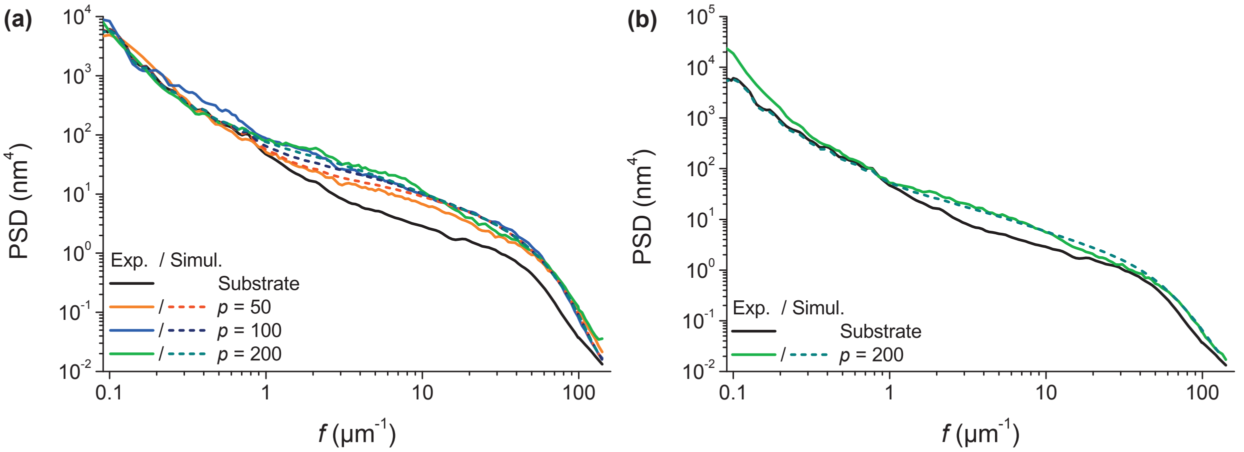

**Fig. 6.2:** Roughness evolution of multilayer coatings for $\lambda = 6.7\,\text{nm}$. **(a)** La-based multilayer coatings; **(b)** Ru-based multilayer coating.

As it is typical for thin film coatings, the roughness components of the substrate are mainly replicated below $f = 1\,\mu\text{m}^{-1}$ throughout all layers of the La-based multilayer. Above this spatial frequency, the PSD steadily grows with increasing bi-layers similar to the Mo/Si multilayer stacks. At high spatial frequencies, the individual PSDs begin to overlap, indicating an equilibrium between smoothing and roughening. The same behavior can be observed for the Ru-based multilayer, however with a lower increase of the overall PSD level after 200 bi-layers.

Beginning with the La-based multilayer coatings, the roughness evolution was modeled using the LCM. Since the average increase per bi-layer is much lower for the La- and Ru-based multilayer coatings than for the Mo/Si multilayer stacks studied in Sec. 4.1.2, no single La, Ru, or $B_4C$ thin films were analyzed in order to decouple the growth parameters between the different layer materials of the multilayer. This is partly compensated for by the intermediate multilayer stacks, all of which were used for the modeling process. After modeling the roughness evolution for the La-based thin film coatings, the same procedure was repeated for the Ru-based multilayer. Since the deposition parameters for $B_4C$ were not altered between both coating types, identical growth parameters for $B_4C$ were assumed.

Over the entire covered spatial frequency range, a good agreement between the modeled and measured PSDs was obtained for all intermediate interfaces and coating types for the growth parameters listed in table 6.1, as shown in Fig. 6.2.

**Table 6.1:** LCM growth parameters for La/$B_4C$ and Ru/$B_4C$ multilayer coatings.

| growth parameter | La | Ru | $B_4C$ |
|---|---|---|---|
| $\Omega$ (nm$^3$) | 0.203 | 0.083 | 0.042 |
| $\nu_{n=1}$ | 0.08 | | |
| $\nu_{n=4}$(nm$^3$) | 2.07 | | |

Similar to the sputtered Mo/Si multilayer coatings (see Sec. 4.1.2), the main relaxation mechanism is surface diffusion ($n = 4$) for all three coating materials, which leads to the convergence of all PSDs as well as the $1/f^4$ decline at high spatial frequencies. The corresponding relaxation rate, $\nu_{n=4}$, is identical for all three materials.

In order to also consider the slight smoothening behavior of the multilayer coatings at spatial frequencies between $f = 10\,\mu\text{m}^{-1}$ and $40\,\mu\text{m}^{-1}$, a further relaxation mechanism was assumed ($n = 1$), indicating viscous flow as an additional relaxation process.

The growth volume for $B_4C$ is close to the atomic volume ($\mathcal{V}_{\mathrm{B_4C}} = 0.037\,\text{nm}^3$), suggesting an amorphous structure. The growth volume for the absorber materials is much higher than their atomic volumes, which can be attributed to polycrystallinities or the compound formation between the two multilayer materials.

## 6.3 Optimal number of layers

Based on the detailed roughness evolution model, it is possible to simulate the scattering behavior of both coatings for an arbitrary number of bi-layers. This can be exploited to determine the optimal number of bi-layers for a given substrate in order to achieve the highest possible reflectance by specifically balancing roughening and smoothing effects.

In a first simulation, only the intrinsic thin film roughness is analyzed by assuming a perfect substrate without any roughness. For a better evaluation and comparison of the results, the same scattering simulation was performed for a Mo/Si multilayer stack as well, based on the LCM growth parameters determined in Sec. 4.1.2. The multilayer designs of all three coatings are optimized for an incidence angle of $\theta_\mathrm{i} = 5°$. In Fig. 6.3, the HSFR of the top-surface as well as the multilayer reflectance with and without the consideration of the scattering losses are plotted as a function of the number of bi-layers.

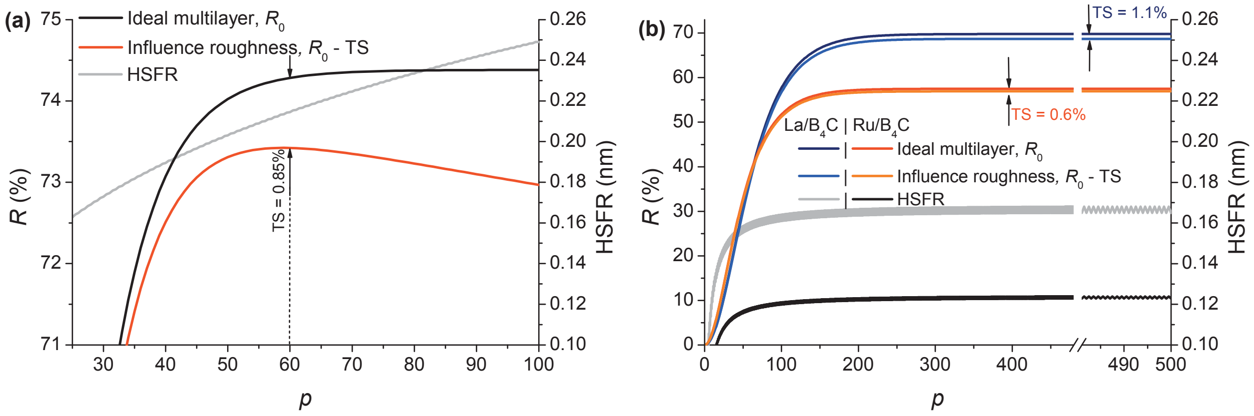

**Fig. 6.3:** Influence of scattering loss on optimal number of bi-layers. **(a)** Mo/Si multilayer for $\lambda = 13.5\,\mathrm{nm}$; **(b)** coatings for $\lambda = 6.7\,\mathrm{nm}$.

For the Mo/Si multilayer, the HSFR and thus the scattering loss steadily rise with increasing number of bi-layers. Due to the growing number of layers, also the multilayer reflectance improves quickly at the beginning of the plot until the penetration depth of the EUV radiation is reached. From this point on, the ideal multilayer reflectance becomes saturated because the lowermost layers of the multilayer stack do not contribute to the reflectance anymore. However, because of the continuous increase of the HSFR of the upper interfaces, the TS still grows with increasing number of thin films. Therefore, the actual multilayer reflectance decreases for a large number of layers, as indicated by the red line in Fig. 6.3a, which leads to an optimal number of bi-layers of 59 for the highest reflectance. This value is very close to the number of bi-layers actually used in Sec. 4.1.2, which was chosen rather heuristically based on the negligible increase of the theoretical reflectance for more bi-layers.

The surface roughness of the La- and Ru-based multilayers likewise quickly increase until ∼100 bi-layers are reached. After this point, smoothing effects and intrinsic thin film roughness cancel each other so that the HSFR reaches saturation but still exhibits a slight zigzag course as can be preferably observed for the uppermost bi-layers because of the larger scaling of the x-axis for these periods. The zigzag course occurs because the absorber layers increase the interface roughness slightly and the next spacer layer smoothens this additional roughness again. The same observation can be made for the Mo/Si multilayer, although the amplitude of the zigzag course is much smaller; here, the spacer material also reduces the HSFR while it is increased by the Mo absorber layers.

The fast saturation of the top-surface roughness after the initially deposited bi-layers of both multilayer coatings for $\lambda = 6.7\,\mathrm{nm}$ and the finite penetration depth of the incident radiation lead to no significant increase in the scattering loss for a high number of bi-layers. Below 200 bi-layers the scattering loss is, of course, continuously increasing because of the growing number of contributing rough interfaces. Hence, the optimal number of layers for a high reflectance is not as limited as for Mo/Si multilayers; above 200 bi-layers the offset between the ideal reflectance, $R_0$, without any roughness and the actually achievable reflectance is not changing anymore. For the Ru-based multilayer, the offset is TS = 0.6% and thus comparable to the Mo/Si multilayer. For the La-based multilayer, the scattering loss is slightly elevated (TS = 1.1%).

In a real application scenario, the scattering loss can be higher because of replicated substrate roughness through the entire multilayer stack. Therefore, the roughness evolution for all three multilayer coatings was modeled for the moderately rough substrate PSD of the two Mo/Si coatings discussed in Sec. 4.2, using the same multilayer design and LCM growth parameters as before. The results of these calculations are presented in Fig. 6.4.

At the lowermost interfaces of the Mo/Si multilayer stack, the HSFR slightly improves before it rises continuously with increasing number of layers. Hence, compared to the simulation without substrate roughness, the roughness increase of the Mo/Si multilayer stack is delayed, which leads to $p = 62$ for the optimal number of bi-layers. For rougher substrates, the optimal number of layers continues to rise. In contrast, the top-surface roughnesses of the coatings for $\lambda = 6.\mathrm{x}\,\mathrm{nm}$ begin to fall right after the deposition of the first bi-layer and approach the intrinsic roughness of the thin films, shown in Fig. 6.3b. The initial substrate roughness can thus easily be compensated for by a higher number of layers, which drastically reduces the requirement on the substrate finish for coatings at $\lambda = 6.7\,\mathrm{nm}$. If a sufficient number of bi-layers are deposited, the overall scattering loss is then only determined by the intrinsic thin film roughness. Furthermore, by depositing the multilayer stacks at an oblique deposition angle, the scattering losses can be reduced in the same way as demonstrated for the Mo/Si multilayer coatings in Sec. 4.2.3.

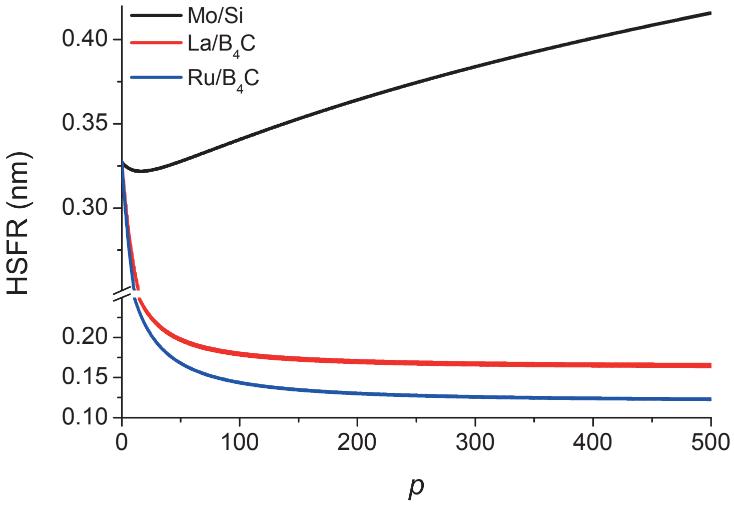

**Fig. 6.4:** Evolution of the HSFR as a function of the number of bi-layers of different multilayer coatings for $\lambda = 6.7\,\mathrm{nm}$ and $13.5\,\mathrm{nm}$. For these simulations, a moderately rough substrate with an HSFR of 0.33 nm was assumed.

Hence, despite the strong wavelength-scaling of $1/\lambda^4$ for the scattering from thin film coatings [see Eq. (2.15)] and the large number of interfaces, the scattering losses from La- and Ru-based multilayer coatings are comparable to a high quality Mo/Si multilayer. This can be attributed to the fortunate circumstance that the relevant spatial frequency range for the ARS overlaps with the spatial frequency range for which the substrate roughness is smoothed by the thin film stack. Thus, the large observed differences between experimental and theoretical reflectances of multilayer coatings for $\lambda = 6.7\,\mathrm{nm}$ more likely result from intermixing between the layer materials.

# 7 Conclusions and Outlook

The continuous reduction of the exposure wavelength in projection lithography, as motivated by the realization of smaller semiconductor dimensions, leads to drastically increasing requirements on optical components. In particular, light scattering from interface imperfections becomes crucially important at EUV wavelengths and can easily limit the optical throughput and resolution because of its strong wavelength dependence. Separating, quantifying, and understanding the relevant scattering mechanisms thus constitute the key for further improvements. However, despite its negative properties, scattered light also carries valuable information about its origins. This can be exploited to characterize the interface roughness of optical components as well as singular defects, with the help of appropriate scattering theories.

Therefore, the aim of this thesis was twofold: on the one hand, the scattering properties of Mo/Si multilayer coatings were investigated and linked to theoretical modeling and analysis tools in order to obtain a detailed knowledge about the impact of the substrate finish, the intrinsic thin film roughness, and the multilayer deposition parameters on the final scattering properties. On the other hand, angle resolved light scattering measurements at EUV and visible wavelengths were performed in order to determine to which extent they can be used to characterize the surface roughness of polished substrates for EUV multilayer optics.

The investigations of the Mo/Si multilayer coatings performed in this work, revealed that the surface irregularities of the substrate are primarily replicated through the entire multilayer stack. In addition, intrinsic thin film roughness enhances the interface imperfections in most of the relevant spatial frequency range for EUV scattering. Only at the upper end of the high spatial frequency range, it is possible that the roughness components are smoothed from one interface to the other. This roughness evolution could be precisely modeled with the linear continuum model. Ambiguities in the corresponding growth parameters between the two layer materials of the multilayer stack could thereby, for the first time, be successfully avoided by studying the roughness evolution of single Si thin films with different layer thicknesses in addition to the Mo/Si multilayer coatings. It was also attempted to model the thin film growth of single Mo coatings. However, it turned out that the roughness evolution of the single Mo thin films differed significantly from those in a multilayer stack, which could be ascribed to a strong oxidation of the single Mo thin films.

In order to reduce the overall scattering loss from Mo/Si multilayer coatings to $(1-2)\%$, it was shown that the substrate roughness must be between $\mathrm{HSFR} = 0.1\,\mathrm{nm}$ and $0.2\,\mathrm{nm}$. For smoother substrates, the scattering loss does not significantly improve anymore as most of the light is scattered from intrinsic thin film roughness ($\mathrm{TS}_{\mathrm{int}}$ ~0.9%). For rougher substrates, the overall scattering rapidly increases. For instance, for an HSFR of 0.34 nm, a total scattering loss of ~4% was determined.

Based on the detailed characterization of the individual influencing factors and the modeling procedures presented in this thesis, the EUV scattering and thus also the EUV reflectance can be precisely predicted prior to manufacturing, if the substrate roughness is known. This was demonstrated for two extended surface areas, by comparing the predicted EUV reflectance values to actual EUV reflectance measurements of the final multilayer coatings, performed at the PTB in Berlin, which revealed an average deviation of less than $< 1\%$. Furthermore, the detailed modeling of the scattering properties enables an optimization of the EUV mirror even for a non-perfect substrate roughness. As an example, the optimal number of multilayer periods for a low scattering and a high EUV reflectance was determined by specifically balancing roughening and smoothing effects during the growth of the multilayer.

Another innovative approach, developed in this work, to even further optimize the multilayer scattering properties is the application of an oblique deposition scheme. Compared to other scattering reduction techniques, discussed in the literature, such as the use of an anti-reflection layer [182] or a shift of the stationary electric field inside the multilayer stack [180,181], the main advantage of this approach is that no modifications to the multilayer design or an exchange of the multilayer materials are required. With the novel concept, the interface cross-correlation PSDs of the multilayer stack are varied, which determine the interference between the individually scattered electric fields of all rough interfaces. Hence, the overall scattering can be significantly reduced by destructive interference. This was demonstrated for a deposition angle of $-30°$, for which a scattering reduction of 28% compared to a normally deposited Mo/Si multilayer with equal interface roughness could be obtained without any degradation of the EUV reflectance. For a deposition angle of $-60°$, a scattering reduction of even 67% was predicted. As these improvements do not rely on a specific substrate or multilayer roughness, the technique can also be applied to samples with an already small substrate roughness. In this way, extremely low scattering losses below 1% can be achieved for Mo/Si multilayer coatings. The scatter reduction thereby not only occurs at large scattering angles but can be observed as close as 2° from the specular beam, which is favorable for imaging optics.

Aside from realizing the required substrate roughness for EUV optics, it is a challenge on its own to achieve these specifications homogeneously on aspheric and large substrates required for EUV projection lithography. Characterizing the surface finish over the entire sample surface thus becomes essential in order to control the polishing process and to avoid any severe losses in the optical system or apodization related problems in the later lithographic process. However, up to now, this could only be realized at small, isolated measurement positions with conventional metrology tools. In order to overcome this lack of appropriate characterization techniques, a novel approach based on angle resolved light scattering measurements at visible wavelengths was developed in this thesis. Due to the non-contact and fast measurement acquisition, area covering roughness maps of the entire sample surface with more than 30 000 individual roughness measurements could be derived in less than six hours, which would be impossible with classical high-resolution roughness characterization techniques because of the long measurement times. For instance, with an atomic force microscope more than half a year would be required in a nonstop operation for the same amount of measurement positions. Furthermore, by exploiting polarization effects, a roughness sensitivity of HSFR $< 0.04\,\mathrm{nm}$ could be demonstrated for the light scattering based roughness characterization approach, which is comparable to the noise limit of an atomic force microscope.

For the first time, it was also attempted to determine the substrate roughness from light scattering measurements at $\lambda = 13.5\,\mathrm{nm}$. However, due to the small change of the refractive index between air and the substrate material, the roughness-induced scattering signal is very low and other scattering sources, such as subsurface damage, can lead to much higher scattering levels. As these two different scattering sources cannot be distinguished in the measured scattering distribution, this can lead to a severe overestimation of the surface roughness, as was demonstrated for two $CaF_2$ substrates with comparable surface finish but different amounts of SSD. At visible wavelengths, this ambiguity can be neglected because of the larger change in the refractive index and a higher scattering signal from surface roughness even for superpolished surfaces.

The results presented in this thesis contributed to a deeper understanding of the scattering characteristics of Mo/Si multilayer coatings and also motivate the application to other spectral ranges and multilayer coatings. Thus, the work may extend in the future into a variety of directions:

- The most prominent of these paths are coatings for $\lambda = 6.\mathrm{x}\,\mathrm{nm}$, proposed as next lithography exposure wavelength after $\lambda = 13.5\,\mathrm{nm}$ [9, 32]. First investigations in this thesis revealed that the roughness evolution of lanthanum and ruthenium based multilayer thin films for $\lambda = 6.7\,\mathrm{nm}$ could be described in a similar way as the Mo/Si multilayer coatings. Hence, techniques such as the oblique multilayer deposition for the reduction of the overall scattering can be applied as well. Surprisingly, these results also showed that in contrast to the Mo/Si multilayer coatings, the main source of scattering is intrinsic thin film roughness. Even for moderately rough substrates, the influence from the substrate roughness can be reduced because of the fortunate circumstance that the relevant spatial frequency range for scattering overlaps with the spatial frequency range for which smoothing from the thin film occurs. Hence, although the exposure wavelength is reduced, the roughness-induced scattering can become more favorable at $\lambda = 6.7\,\mathrm{nm}$.

- Another promising path is the analysis of subsurface damage by EUV light scattering measurements, as first results in this work on the scattering characteristics of $CaF_2$ substrates revealed. In this way, the usually destructive characterization by etching, fracturing, or taper polishing can be prevented [200, 281–284]. A further refinement of this technique could be achieved by changing the angle of incidence. In this way, the analysis volume can be precisely controlled, enabling a detailed characterization of the SSD depth.

- A further interesting research area is the development of spectral purity filters for laser produced plasma sources. A promising solution, discussed in the thesis, are grating-like coatings which can filter a singular wavelength. Because of the encouraging results, first plans to combine several gratings have also been proposed [270]. The combination of grating-like optics with other filtering techniques, such as Si pyramids or anti-reflection coatings, is an interesting option as well in order to increase the spectral range of the filtering device [251, 252]. These concepts will, however, only be successful if the EUV performance is not severally degraded, which makes a detailed study of the interface roughness even more important.

In summary, the combination of the different techniques developed in this thesis enables the scattering of Mo/Si multilayer coatings to be controlled and reduced, starting with the characterization and improvement of the substrate finish already early in the manufacturing process followed by the optimization of the actual multilayer deposition. As a result, extremely low scattering losses of $< 1\%$ can be achieved without excessive specifications for the interface roughness and at the same time, the risk of not reaching the ambitious specifications for the final multilayer optic is drastically reduced.

# References

[1] ISO 21348:2007(E), *Space environment (natural and artificial) - Process for determining solar irradiances* (2007).

[2] G. E. Moore, “Cramming More Components onto Integrated Circuits,” Electronics **38**, 114–117 (1965).

[3] Intel®, *Excerpts from A Conversation with Gordon Moore: Moore’s Law* (2005).

[4] T. Ito and S. Okazaki, “Pushing the limits of lithography,” Nature **406**, 1027–1031 (2000).

[5] J. H. Bruning, “Optical Lithography ... 40 years and holding,” Proc. SPIE **6520**, 652004 (2007).

[6] B. Wu and A. Kumar, “Extreme ultraviolet lithography: A review,” J. Vac. Sci. Technol. B **25**, 1743–1761 (2007).

[7] M. Totzeck, W. Ulrich, A. Göhnermeier, and W. Kaiser, “Pushing deep ultraviolet lithography to its limits,” Nature Photon. **1**, 629–631 (2007).

[8] C. Wagner and N. Harned, “EUV lithography: Lithography gets extreme,” Nature Photon. **4**, 24–26 (2010).

[9] International Technology Roadmap for Semiconductors, “Lithography - 2013 Edition,” `http://www.itrs.net/Links/2013ITRS/2013Chapters/2013Litho.pdf` (last accessed: February 2, 2015).

[10] R. Peeters, S. Lok, J. Mallman, M. van Noordenburg, N. Harned, P. Kuerz, M. Lowisch, E. van Setten, G. Schiffelers, A. Pirati, J. Stoeldraijer, D. Brandt, N. Farrar, I. Fomenkov, H. Boom, H. Meiling, and R. Kool, “EUV lithography: NXE platform performance overview,” Proc. SPIE **9048**, 90481J (2014).

[11] J. M. Elson and J. M. Bennett, “Vector Scattering Theory,” Opt. Eng. **18**, 116–124 (1979).

[12] P. Bousquet, F. Flory, and P. Roche, “Scattering from multilayer thin films: theory and experiment,” J. Opt. Soc. Am. **71**, 1115–1123 (1981).

[13] E. L. Church and P. Z. Takacs, “Surface scattering,” in “Handbook of optics: Fundamentals, Techniques, and Design,” M. Bass, ed. (McGraw-Hill, Inc., New York, N.Y., USA, 1995), chap. 7, pp. 7.1–7.14, 2nd ed.

[14] T. A. Germer, “Angular dependence and polarization of out-of-plane optical scattering from particulate contamination, subsurface defects, and surface microroughness,” Appl. Opt. **36**, 8798–8805 (1997).

[15] E. M. Gullikson, S. Baker, J. E. Bjorkholm, J. Bokor, K. A. Goldberg, J. E. M. Goldsmith, C. Montcalm, P. Naulleau, E. Spiller, D. G. Stearns, J. S. Taylor, and J. H. Underwood, “EUV Scattering and Flare of 10x Projection Cameras,” Proc. SPIE **3676**, 717–723 (1999).

[16] J. P. Cain, P. Naulleau, and C. J. Spanos, “Lithographic measurement of EUV flare in the 0.3-NA Micro Exposure Tool optic at the Advanced Light Source,” Proc. SPIE **5751**, 301–311 (2005).

[17] T. W. Barbee Jr., S. Mrowka, and M. C. Hettrick, “Molybdenum-silicon multilayer mirrors for the extreme ultraviolet,” Appl. Opt. **24**, 883–886 (1985).

[18] E. Spiller, *Soft X-Ray Optics* (SPIE Press, Bellingham, Wash., USA, 1994).

[19] J. C. Stover, *Optical Scattering: Measurement and Analysis* (SPIE Press, Bellingham, Wash., USA, 2012), 3rd ed.

[20] A. Duparré, “Light Scattering of Thin Dielectric Films,” in “Thin Films for Optical Coatings,” R. E. Hummel and K. H. Guenther, eds. (CRC Press, Inc., Boca Raton, Flor., USA, 1995), chap. 10, pp. 273–303.

[21] J. M. Bennett and L. Mattsson, *Introduction to Surface Roughness and Scattering* (Optical Society of America, Washington, D.C., USA, 1989).

[22] C. Amra, “Light scattering from multilayer optics. II. Application to experiment,” J. Opt. Soc. Am. A **11**, 211–226 (1994).

[23] M. Lowisch, P. Kuerz, O. Conradi, G. Wittich, W. Seitz, and W. Kaiser, “Optics for ASML’s NXE:3300B platform,” Proc. SPIE **8679**, 86791H (2013).

[24] J. T. Neumann, P. Gräupner, W. Kaiser, R. Garreis, and B. Geh, “Mask effects for high-NA EUV: impact of NA, chief-ray-angle, and reduction ratio,” Proc. SPIE **8679**, 867915 (2013).

[25] N. R. Böwering, A. I. Ershov, W. F. Marx, O. V. Khodykin, B. A. M. Hansson, E. Vargas L., J. A. Chavez, I. V. Fomenkov, D. W. Myers, and D. C. Brandt, "EUV Source Collector," Proc. SPIE **6151**, 61513R (2006).

[26] E. M. Gullikson, D. G. Stearns, D. P. Gaines, and J. H. Underwood, "Non-specular scattering from multilayer mirrors at normal incidence," Proc. SPIE **3115**, 412–419 (1997).

[27] D. G. Stearns, D. P. Gaines, D. W. Sweeney, and E. M. Gullikson, "Nonspecular x-ray scattering in a multilayer-coated imaging system," J. Appl. Phys. **84**, 1003–1028 (1998).

[28] J. M. Freitag and B. M. Clemens, "Nonspecular x-ray reflectivity study of roughness scaling in Si/Mo multilayers," J. Appl. Phys. **89**, 1101–1107 (2001).

[29] S. Schröder, T. Feigl, A. Duparré, and A. Tünnermann, "EUV reflectance and scattering of Mo/Si multilayers on differently polished substrates," Opt. Express **15**, 13997–14012 (2007).

[30] G. Tallents, E. Wagenaars, and G. Pert, "Lithography at EUV wavelengths," Nature Photon. **4**, 809–811 (2010).

[31] International Technology Roadmap for Semiconductors, "Executive Summary - 2013 Edition," `http://www.itrs.net/Links/2013ITRS/2013Chapters/2013ExecutiveSummary.pdf` (last accessed: February 2, 2015).

[32] G. O'Sullivan, T. Cummins, P. Dunne, A. Endo, P. Hayden, T. Higashiguchi, D. Kilbane, B. Li, C. O'Gorman, T. Otsuka, E. Sokell, and N. Yugami, "Recent progress in source development for lithography at 6.x nm," Phys. Scr. **T156**, 014105 (2013).

[33] A. M. Hawryluk and N. M. Ceglio, "Wavelength considerations in soft-x-ray projection lithography," Appl. Opt. **32**, 7062–7067 (1993).

[34] C. Montcalm, P. A. Kearney, J. M. Slaughter, B. T. Sullivan, M. Chaker, H. Pépin, and C. M. Falco, "Survey of Ti-, B-, and Y-based soft x-ray-extreme ultraviolet multilayer mirrors for the 2- to 12-nm wavelength region," Appl. Opt. **35**, 5134–5147 (1996).

[35] Y. Platonov, L. Gomez, and D. Broadway, "Status of small d-spacing X-ray multilayer development at Osmic," Proc. SPIE **4782**, 152–159 (2002).

[36] F. Cerrina, G. Margaritondo, J. H. Underwood, M. Hettrick, M. A. Green, L. J. Brillson, A. Franciosi, H. Höchst, P. M. Deluca Jr., and M. N. Gould, "MAXIMUM: A Scanning Photoelectron Microscope at Aladdin," Nucl. Instrum. Methods A **266**, 303–307 (1988).

[37] J. A. Trail and R. L. Byer, "Compact scanning soft-x-ray microscope using a laser-produced plasma source and normal-incidence multilayer mirrors," Opt. Lett. **14**, 539–541 (1989).

[38] I. A. Artyukov, A. I. Fedorenko, V. V. Kondratenko, S. A. Yulin, and A. V. Vinogradov, "Soft X-ray submicron imaging experiments with nanosecond exposure," Opt. Commun. **102**, 401–406 (1993).

[39] T. Foltyn, K. Bergmann, S. Braun, P. Gawlitza, A. Leson, W. Neff, and K. Walter, "Design and development of an optical system for EUV-microscopy," Proc. SPIE **5533**, 37–46 (2004).

[40] K. A. Goldberg, I. Mochi, M. P. Benk, C. Lin, A. Allezy, M. Dickinson, C. W. Cork, J. B. Macdougall, E. H. Anderson, W. Chao, F. Salmassi, E. M. Gullikson, D. Zehm, V. Vytla, W. Cork, J. DePonte, G. Picchi, A. Pekedis, T. Katayanagi, M. S. Jones, E. Martin, P. P. Naulleau, and S. B. Rekawa, "The SEMATECH high-NA actinic reticle review project (SHARP) EUV mask-imaging microscope," Proc. SPIE **8880**, 88800T (2013).

[41] W. Ackermann, G. Asova, V. Ayvazyan, A. Azima, N. Baboi, J. Bähr, *et al.*, "Operation of a free-electron laser from the extreme ultraviolet to the water window," Nature Photon. **1**, 336–342 (2007).

[42] V. Hilbert, A. Blinne, S. Fuchs, T. Feigl, T. Kämpfer, C. Rödel, I. Uschmann, M. Wünsche, G. G. Paulus, E. Förster, and U. Zastrau, "An extreme ultraviolet Michelson interferometer for experiments at free-electron lasers," Rev. Sci. Instrum. **84**, 095111 (2013).

[43] J. F. Lindblom, A. B. C. Walker Jr., R. B. Hoover, T. W. Barbee Jr., R. A. VanPatten, and J. P. Gill, "Soft X-Ray/Extreme Ultraviolet Images of the Solar Amosphere With Normal Incidence Multilayer Optics," Proc. SPIE **982**, 316–324 (1988).

[44] A. B. C. Walker Jr., T. W. Barbee Jr., R. B. Hoover, and J. F. Lindblom, "Soft X-ray Images of the Solar Corona with a Normal-Incidence Cassegrain Multilayer Telescope," Science **241**, 1781–1787 (1988).

[45] R. Soufli, E. Spiller, D. L. Windt, J. C. Robinson, E. M. Gullikson, L. Rodriguez-de Marcos, M. Fernández-Perea, S. L. Baker, A. L. Aquila, F. J. Dollar, J. A. Méndez, J. I. Larruquert, L. Golub, and P. Boerner, "In-band and out-of-band reflectance calibrations of the EUV multilayer mirrors of the Atmospheric Imaging Assembly instrument aboard the Solar Dynamics Observatory," Proc. SPIE **8443**, 84433C (2012).

[46] D. Martínez-Galarce, R. Soufli, D. L. Windt, M. Bruner, E. Gullikson, S. Khatri, E. Spiller, J. C. Robinson, S. Baker, and E. Prast, “Multisegmented, multilayer-coated mirrors for the Solar Ultraviolet Imager,” Opt. Eng. **52**, 095102 (2013).

[47] V. Džimbeg-Malčić, Ž. Barbarić-Mikočević, and K. Itrić, “Kubelka-Munk theory in describing optical properties of paper (I),” Tehn. vjesn. **18**, 117–124 (2011).

[48] M. A. Hubbe, J. J. Pawlak, and A. A. Koukoulas, “Paper’s appearance: A review,” BioRes. **3**, 627–665 (2008).

[49] ASME B46.1-2002, *Surface Texture – Surface Roughness, Waviness, and Lay* (2002).

[50] DIN EN ISO 25178-2:2012, *Geometrical product specifications (GPS) - Surface texture: Areal - Part 2: Terms, definitions and surface texture parameters* (2012).

[51] E. L. Church, H. A. Jenkinson, and J. M. Zavada, “Relationship between Surface Scattering and Microtopographic Features,” Opt. Eng. **18**, 125–136 (1979).

[52] J. M. Elson and J. M. Bennett, “Calculation of the power spectral density from surface profile data,” Appl. Opt. **34**, 201–208 (1995).

[53] A. Duparré, J. Ferré-Borrull, S. Gliech, G. Notni, J. Steinert, and J. M. Bennett, “Surface characterization techniques for determining the root-mean-square roughness and power spectral densities of optical components,” Appl. Opt. **41**, 154–171 (2002).

[54] E. L. Church, H. A. Jenkinson, and J. M. Zavada, “Measurement of the Finish of Diamond-Turned Metal Surfaces By Differential Light Scattering,” Opt. Eng. **16**, 360–374 (1977).

[55] C. Amra, “From light scattering to the microstructure of thin-film multilayers,” Appl. Opt. **32**, 5481–5491 (1993).

[56] J. S. Taylor, G. E. Sommargren, D. W. Sweeney, and R. M. Hudyma, “The Fabrication and Testing of Optics for EUV Projection Lithography,” Proc. SPIE **3331**, 580–590 (1998).

[57] M. Flemming, “Methoden der Simulation und Charakterisierung von nanostrukturierten ultrahydrophoben Oberflächen für optische Anwendungen,” Ph.D. thesis, Ilmenau University of Technology (2006).

[58] D. J. Whitehouse, “Instrumentation,” in “Handbook of Surface Metrology,” (Institute of Physics Publishing, Bristol, UK, 1994), chap. 4.

[59] C. Ruppe and A. Duparré, “Roughness analysis of optical films and substrates by atomic force microscopy,” Thin Solid Films **288**, 8–13 (1996).

[60] R. Breil, T. Fries, J. Garnaes, J. Haycocks, D. Hüser, J. Joergensen, W. Kautek, L. Koenders, N. Kofod, K. R. Koops, R. Korntner, B. Lindner, W. Mirandé, A. Neubauer, J. Peltonen, G. B. Picotto, M. Pisani, H. Rothe, M. Sahre, M. Stedman, and G. Wilkening, “Intercomparison of scanning probe microscopes,” Precis. Eng. **26**, 296–305 (2002).

[61] P. Z. Takacs, K. Furenlid, R. A. DeBiasse, and E. L. Church, “Surface topography measurements over the 1 meter to 10 micrometer spatial period bandwidth,” Proc. SPIE **1164**, 203–211 (1989).

[62] L. Assoufid, A. Rommeveaux, H. Ohashi, K. Yamauchi, H. Mimura, J. Qian, O. Hignette, T. Ishikawa, C. Morawe, A. Macrander, A. Khounsary, and S. Goto, “Results of x-ray mirror round-robin metrology measurements at the APS, ESRF, and SPring-8 optical metrology laboratories,” Proc. SPIE **5921**, 59210J (2005).

[63] H. Takeuchi, K. Yosizumi, and H. Tsutsumi, “Ultrahigh Accurate 3-D Profilometer Using Atomic Force Probe of Measuring Nanometer,” in “Topical Meeting of the American Society for Precision Engineering, ASPE,” (Chapel Hill, N.C., USA, 2004), pp. 1–6.

[64] E. Manske, G. Jäger, T. Hausotte, and R. Füßl, “Recent developments and challenges of nanopositioning and nanomeasuring technology,” Meas. Sci. Technol. **23**, 074001 (2012).

[65] D. Malacara, *Optical Shop Testing* (John Wiley & Sons, Inc., Hoboken, N.J., USA, 2007), 3rd ed.

[66] G. E. Sommargren, D. W. Phillion, and E. W. Campbell, “Sub-nanometer Interferometry for Aspheric Mirror Fabrication,” 9th International Conference on Production Engineering, Osaka, Japan (1999).

[67] K. A. Goldberg, P. Naulleau, J. Bokor, H. N. Chapman, and A. Barty, “Testing extreme ultraviolet optics with visible-light and extreme ultraviolet interferometry,” J. Vac. Sci. Technol. B **20**, 2834–2839 (2002).

[68] P. P. Naulleau, K. A. Goldberg, S. H. Lee, C. Chang, D. Attwood, and J. Bokor, “Extreme-ultraviolet phase-shifting point-diffraction interferometer: a wave-front metrology tool with subangstrom reference-wave accuracy,” Appl. Opt. **38**, 7252–7263 (1999).

[69] M. Lowisch, P. Kuerz, H.-J. Mann, O. Natt, and B. Thuering, “Optics for EUV production,” Proc. SPIE **7636**, 763603 (2010).

[70] D. W. Sweeney, R. Hudyma, H. N. Chapman, and D. Shafer, “EUV Optical Design for a 100 nm CD Imaging System,” Proc. SPIE **3331**, 2–10 (1998).

[71] H. Meiling, J. Benschop, U. Dinger, and P. Kürz, “Progress of the EUVL alpha tool,” Proc. SPIE **4343**, 38–50 (2001).

[72] W. H. Bragg and W. L. Bragg, “The Reflection of X-rays by Crystals,” Proc. R. Soc. London, Ser. A **88**, 428–438 (1913).

[73] C. Kittel, “Introduction to Solid State Physics,” (John Wiley & Sons, Inc., Hoboken, N.J., USA, 2005), chap. 1, 8th ed.

[74] E. Spiller, *Soft X-Ray Optics* (SPIE Press, Bellingham, Wash., USA, 1994), chap. 7.

[75] S. Yulin, “Multilayer Coatings for EUV/Soft X-ray Mirrors,” in “Optical Interference Coatings,” N. Kaiser and H. K. Pulker, eds. (Springer, Berlin, 2003), pp. 281–307.

[76] R.-P. Haelbich and C. Kunz, “Multilayer interference mirrors for the XUV range around 100 eV photon energy,” Opt. Commun. **17**, 287–292 (1976).

[77] S. Braun, “Gefüge- und Grenzflächenbeschaffenheit von Mo/Si-Multischichten, synthetisiert mittels Puls-Laser- und Magentron-Sputter-Deposition,” Ph.D. thesis, Bielefeld University (2004).

[78] E. Spiller, “Low-Loss Reflection Coatings Using Absorbing Materials,” Appl. Phys. Lett. **20**, 365–367 (1972).

[79] S. Braun, H. Mai, M. Moss, R. Scholz, and A. Leson, “Mo/Si Multilayers with Different Barrier Layers for Applications as Extreme Ultraviolet Mirrors,” Jpn. J. Appl. Phys. **41**, 4074–4081 (2002).

[80] T. Feigl, S. Yulin, N. Benoit, and N. Kaiser, “EUV multilayer optics,” Microelectron. Eng. **83**, 703–706 (2006).

[81] A. E. Yakshin, R. W. E. van de Kruijs, I. Nedelcu, E. Zoethout, E. Louis, F. Bijkerk, H. Enkisch, and S. Müllender, “Enhanced reflectance of interface engineered Mo/Si multilayers produced by thermal particle deposition,” Proc. SPIE **6517**, 65170I (2007).

[82] I. V. Fomenkov, B. La Fontaine, D. Brown, I. Ahmad, P. Baumgart, N. R. Böwering, D. C. Brandt, A. N. Bykanov, S. De Dea, A. I. Ershov, N. R. Farrar, D. J. Golich, M. J. Lercel, D. W. Myers, C. Rajyaguru, S. N. Srivastava, Y. Tao, and G. O. Vaschenko, “Development of stable extreme-ultraviolet sources for use in lithography exposure systems,” J. Micro/Nanolith. MEMS MOEMS **11**, 021110 (2012).

[83] V. Rehn, V. O. Jones, J. M. Elson, and J. M. Bennett, “The Role of Surface Topography in Predicting Scattering at Grazing Incidence from Optical Surfaces,” Nucl. Instrum. Methods **172**, 307–314 (1980).

[84] A. Duparré, “Scattering from Surfaces and Thin Films,” in “Encyclopedia of Modern Optics,” B. D. Guenther, D. G. Steel, and L. Bayvel, eds. (Elsevier, 2004), pp. 314–321.

[85] F. E. Nicodemus, J. C. Richmond, J. J. Hsia, I. W. Ginsberg, and T. Limperis, “Geometrical Considerations and Nomenclature for Reflectance,” Natl. Bur. Stand. Monograph **160**, 1–52 (1977).

[86] SEMI ME 1392-0305, *Guide for Angle Resolved Optical Scatter Measurements on Specular or Diffuse Surfaces* (2005).

[87] ASTM E2387-05, *Standard Practice for Goniometric Optical Scatter Measurements* (2005).

[88] J. C. Stover, “Scatterometers,” in “Handbook of optics: Devices, Measurements, & Properties,” M. Bass, ed. (McGraw-Hill, Inc., New York, N.Y., USA, 1995), chap. 26, pp. 26.1–26.16, 2nd ed.

[89] ISO 13696:2002(E), *Optics and optical instruments - Test methods for radiation scattered by optical components* (2002).

[90] M. Saillard and A. Sentenac, “Rigorous solutions for electromagnetic scattering from rough surfaces,” Waves Random Media **11**, R103–R137 (2001).

[91] P. Beckmann and A. Spizzichino, *The Scattering of Electromagnetic Waves from Rough Surfaces* (Pergamon Press, Oxford, UK, 1963).

[92] J. E. Harvey, A. Krywonos, and C. L. Vernold, “Modified Beckmann-Kirchhoff scattering model for rough surfaces with large incident and scattering angles,” Opt. Eng. **46**, 078002 (2007).

[93] K. F. Warnick and W. C. Chew, “Numerical simulation methods for rough surface scattering,” Waves Random Media **11**, R1–R30 (2001).

[94] T. M. Elfouhaily and C.-A. Guérin, “A critical survey of approximate scattering wave theories from random rough surfaces,” Waves Random Media **14**, R1–R40 (2004).

[95] S. O. Rice, “Reflection of Electromagnetic Waves from Slightly Rough Surfaces,” Commun. Pure Appl. Math. **4**, 351–378 (1951).

[96] Lord Rayleigh, “On the Dynamical Theory of Gratings,” Proc. R. Soc. London, Ser. A **79**, 399–416 (1907).

[97] E. L. Church and J. M. Zavada, “Residual surface roughness of diamond-turned optics,” Appl. Opt. **14**, 1788–1795 (1975).

[98] H. Davies, “The reflection of electromagnetic waves from a rough surface,” Proc. IEEE **101**, 209–214 (1954).

[99] H. E. Bennett and J. O. Porteus, “Relation Between Surface Roughness and Specular Reflectance at Normal Incidence,” J. Opt. Soc. Am. **51**, 123–129 (1961).

[100] J. C. Stover, S. Schröder, and T. A. Germer, “Upper roughness limitations on the TIS/RMS relationship,” Proc. SPIE **8495**, 849503 (2012).

[101] P. H. Berning, “Theory and Calculations of Optical Thin Films,” in “Physics of Thin Films,” G. Hass, ed. (Academic Press, New York, N.Y., USA, 1963), pp. 69–121, 1st ed.

[102] M. Born and E. Wolf, “Principles of Optics: Electromagnetic theory of propagation, interference and diffraction of light,” (Cambridge University Press, Cambridge, UK, 1999), chap. 1, 7th ed.

[103] H. A. Macleod, *Thin-Film Optical Filters* (Institute of Physics Publishing, Bristol, UK, 2001), 3rd ed.

[104] J. M. Elson, J. P. Rahn, and J. M. Bennett, “Light scattering from multilayer optics: comparison of theory and experiment,” Appl. Opt. **19**, 669–679 (1980).

[105] C. Amra, “Light scattering from multilayer optics. I. Tools of investigation,” J. Opt. Soc. Am. A **11**, 197–210 (1994).

[106] D. Rönnow, “Interface roughness statistics of thin films from angle-resolved light scattering at three wavelengths,” Opt. Eng. **37**, 696–704 (1998).

[107] S. F. Edwards and D. R. Wilkinson, “The surface statistics of a granular aggregate,” Proc. R. Soc. London A **381**, 17–31 (1982).

[108] M. Kardar, G. Parisi, and Y.-C. Zhang, “Dynamic Scaling of Growing Interfaces,” Phys. Rev. Lett. **56**, 889–892 (1986).

[109] D. G. Stearns, “Stochastic model for thin film growth and erosion,” Appl. Phys. Lett. **62**, 1745–1747 (1993).

[110] B. A. Movchan and A. V. Demchishin, “Study of the structure and properties of thick vacuum condensates of nickel, titanium, tungsten, aluminium oxide and zirconium dioxide,” Phys. Met. Metallogr. (Engl. Trans.) **28**, 83–90 (1969).

[111] W. M. Tong and R. S. Williams, “Kinetics of Surface Growth: Phenomenology, Scaling, and Mechanisms of Smoothing and Roughening,” Annu. Rev. Phys. Chem. **45**, 401–438 (1994).

[112] D. G. Stearns, “X-ray scattering from interfacial roughness in multilayer structures,” J. Appl. Phys. **71**, 4286–4298 (1992).

[113] R. Canestrari, D. Spiga, and G. Pareschi, “Analysis of microroughness evolution in X-ray astronomical multilayer mirrors by surface topography with the MPES program and by X-ray scattering,” Proc. SPIE **6266**, 626613 (2006).

[114] M. Trost, S. Schröder, T. Feigl, A. Duparré, and A. Tünnermann, “Influence of the substrate finish and thin film roughness on the optical performance of Mo/Si multilayers,” Appl. Opt. **50**, C148–C153 (2011).

[115] T. Herffurth, M. Trost, S. Schröder, K. Täschner, H. Bartzsch, P. Frach, A. Duparré, and A. Tünnermann, “Roughness and optical losses of rugate coatings,” Appl. Opt. **53**, A351–A359 (2014).

[116] B. Salmaso, D. Spiga, R. Canestrari, and L. Raimondi, “X-ray scattering of periodic and graded multilayers: Comparison of experiments to simulations from surface microroughness characterization,” Nucl. Instrum. Methods A **710**, 106–113 (2013).

[117] C. Amra, J. H. Apfel, and E. Pelletier, “Role of interface correlation in light scattering by a multilayer,” Appl. Opt. **31**, 3134–3151 (1992).

[118] D. Rönnow, “Determination of interface roughness cross correlation of thin films from spectroscopic light scattering measurements,” J. Appl. Phys. **81**, 3627–3636 (1997).

[119] J. Ferré-Borrull, A. Duparré, and E. Quesnel, “Roughness and light scattering of ion-beam-sputtered fluoride coatings for 193 nm,” Appl. Opt. **39**, 5854–5864 (2000).

[120] D. G. Stearns, P. B. Mirkarimi, and E. Spiller, “Localized defects in multilayer coatings,” Thin Solid Films **446**, 37–49 (2004).

[121] S. Bajt, J. B. Alameda, T. W. Barbee Jr., W. M. Clift, J. A. Folta, B. Kaufmann, and E. A. Spiller, “Improved reflectance and stability of Mo-Si multilayers,” Opt. Eng. **41**, 1797–1804 (2002).

[122] Y. P. Pershyn, E. M. Gullikson, V. V. Kondratenko, V. V. Mamon, S. A. Reutskaya, D. L. Voronov, E. N. Zubarev, I. A. Artyukov, and A. V. Vinogradov, “Effect of working gas pressure on interlayer mixing in magnetron-deposited Mo/Si multilayers,” Opt. Eng. **52**, 095104 (2013).

[123] J. A. Thornton, “The microstructure of sputter-deposited coatings,” J. Vac. Sci. Technol. A **4**, 3059–3065 (1986).

[124] N. Kaiser, “Review of the fundamentals of thin-film growth,” Appl. Opt. **41**, 3053–3060 (2002).

[125] K. L. Westra and D. J. Thomson, “The microstructure of thin films observed using atomic force microscopy,” Thin Solid Films **257**, 15–21 (1995).

[126] U. Kaiser, N. Kaiser, P. Weißbrodt, U. Mademann, E. Hacker, and H. Müller, “Structure of thin fluoride films deposited on amorphous substrates,” Thin Solid Films **217**, 7–16 (1992).

[127] K. H. Guenther, “Revisiting structure zone models for thin film growth,” Proc. SPIE **1324**, 2–12 (1990).

[128] S. Schröder, T. Herffurth, H. Blaschke, and A. Duparré, “Angle-resolved scattering: an effective method for characterizing thin-film coatings,” Appl. Opt. **50**, C164–C171 (2011).

[129] S. Schröder, T. Herffurth, M. Trost, and A. Duparré, “Angle-resolved scattering and reflectance of extreme-ultraviolet multilayer coatings: measurement and analysis,” Appl. Opt. **49**, 1503–1512 (2010).

[130] N. Kandaka, T. Kobayashi, M. Shiraishi, T. Komiya, T. Oshino, and K. Murakami, “Measurement of EUV scattering from Mo/Si multilayer mirrors,” Photon Factory Activity Report, part B, p. 257 (2003).

[131] A. Haase, V. Soltwisch, C. Laubis, and F. Scholze, “Role of dynamic effects in the characterization of multilayers by means of power spectral density,” Appl. Opt. **53**, 3019–3027 (2014).

[132] M. M. Barysheva, Y. A. Vainer, B. A. Gribkov, M. V. Zorina, A. E. Pestov, N. N. Salashchenko, N. I. Chkhalo, and A. V. Shcherbakov, “Investigation of Supersmooth Optical Surfaces and Multilayer Elements Using Soft X-ray Radiation,” Tech. Phys. **58**, 1371–1379 (2013).

[133] D. R. Cheever, F. M. Cady, K. A. Klicker, and J. C. Stover, “Design review of a unique complete angle scatter instrument (CASI),” Proc. SPIE **818**, 13–20 (1987).

[134] C. L. Vernold, “Application and verification of wavelength scaling for near specular scatter predictions,” Proc. SPIE **1165**, 18–30 (1989).

[135] F. M. Cady, J. C. Stover, D. R. Bjork, M. L. Bernt, M. W. Knighton, D. J. Wilson, and D. R. Cheever, “A design review of a multiwavelength, three-dimensional scatterometer,” Proc. SPIE **1331**, 201–208 (1990).

[136] H. Truckenbrodt, A. Duparré, and U. Schuhmann, “Roughness and Defect Characterization of Optical Surfaces by Light Scattering Measurements,” Proc. SPIE **1781**, 139–151 (1992).

[137] C. Amra, D. Torricini, and P. Roche, “Multiwavelength (0.45 – 10.6 µm) angle-resolved scatterometer or how to extend the optical window,” Appl. Opt. **32**, 5462–5474 (1993).

[138] C. C. Asmail, C. L. Cromer, J. E. Proctor, and J. J. Hsia, “Instrumentation at the National Institute of Standards and Technology for bidirectional reflectance distribution function (BRDF) measurements,” Proc. SPIE **2260**, 52–61 (1994).

[139] K. H. Guenther, P. G. Wierer, and J. M. Bennett, “Surface roughness measurements of low-scatter mirrors and roughness standards,” Appl. Opt. **23**, 3820–3836 (1984).

[140] O. Kienzle, J. Staub, and T. Tschudi, “Description of an integrated scatter instrument for measuring scatter losses of ‘superpolished’ optical surfaces,” Meas. Sci. Technol. **5**, 747–752 (1994).

[141] H. E. Bennett, “Scattering Characteristics of Optical Materials,” Opt. Eng. **17**, 480–488 (1978).

[142] J. A. Detrio and S. M. Miner, “Standardized total integrated scatter measurements of optical surfaces,” Opt. Eng. **24**, 419–422 (1985).

[143] L. Mattsson, “Total integrated scatter measurement system for quality assessment of coatings on optical surfaces,” Proc. SPIE **652**, 264–271 (1986).

[144] D. Rönnow and E. Veszelei, “Design review of an instrument for spectroscopic total integrated light scattering measurements in the visible wavelength region,” Rev. Sci. Instrum. **65**, 327–334 (1994).

[145] ISO 14644-1:1999, *Cleanrooms and associated controlled environments - Part 1: Classification of air cleanliness* (1999).

[146] M. C. Teich, K. Matsuo, and B. E. A. Saleh, "Excess Noise Factors for Conventional and Superlattice Avalanche Photodiodes and Photomultiplier Tubes," IEEE J. Quant. Electron. **22**, 1184–1193 (1986).

[147] Labsphere, "Technical Guide: Reflectance Materials and Coatings," `http://www.labsphere.com/uploads/technical-guides/a-guide-to-reflectance-materials-and-coatings.pdf` (last accessed: February 2, 2015).

[148] R. Lebert, C. Wies, B. Jägle, L. Juschkin, U. Bieberle, M. Meisen, W. Neff, K. Bergmann, K. Walter, O. Rosier, M. C. Schuermann, and T. Missalla, "Status of EUV-Lamp Development and Demonstration of Applications," Proc. SPIE **5374**, 943–953 (2004).

[149] Burle Industries, Inc, "Channeltron - Electron Multiplier Handbook for Mass Spectrometry Applications," `http://www.photonis.com/attachment.php?id_attachment=148` (last accessed: February 2, 2015).

[150] R. Korde, C. Prince, D. Cunningham, R. E. Vest, and E. Gullikson, "Present status of radiometric quality silicon photodiodes," Metrologia **40**, S145–S149 (2003).

[151] S. Schröder, "Light scattering of optical components at 193 nm and 13.5 nm," Ph.D. thesis, Friedrich Schiller University Jena (2008).

[152] T. Herffurth, "Untersuchungen zu Reflexion und Streulicht von EUV-Komponenten," Diplomarbeit, Friedrich Schiller University Jena (2008).

[153] M. Trost, "Messung und Modellierung des Reflexions- und Streuverhaltens von Spiegeln und Substraten für 13.5 nm," Diplomarbeit, Friedrich Schiller University, Jena (2009).

[154] D. L. Windt, "IMD-Software for modeling the optical properties of multilayer films," Comput. Phys. **12**, 360–370 (1998).

[155] B. L. Henke, E. M. Gullikson, and J. C. Davis, "X-ray interactions: photoabsorption, scattering, transmission, and reflection at $E = 50 - 30{,}000$ eV, $Z = 1 - 92$," At. Data Nucl. Data Tables **54**, 181–342, `http://henke.lbl.gov/optical_constants` (1993).

[156] E. D. Palik, ed., *Handbook of Optical Constants of Solids*, vol. I, II, III (Academic Press, San Diego, Calif., USA, 1985/1991/1998).

[157] S. Churilov, Y. N. Joshi, and J. Reader, "High-resolution spectrum of xenon ions at 13.4 nm," Opt. Lett. **28**, 1478–1480 (2003).

[158] A. Sasaki, "Theoretical EUV Spectrum of Near Pd-like Xe," J. Plasma Fusion Res. **79**, 315–317 (2003).

[159] E. Spiller, S. Baker, E. Parra, and C. Tarrio, “Smoothing of mirror substrates by thin-film deposition,” Proc. SPIE **3767**, 143–153 (1999).

[160] D. G. Stearns and E. M. Gullikson, “Nonspecular scattering from extreme ultraviolet multilayer coatings,” Physica B **283**, 84–91 (2000).

[161] T. Feigl, “Struktur und Eigenschaften von Schichtsystemen für den EUV-Spektralbereich,” Ph.D. thesis, Friedrich Schiller University Jena (2000).

[162] S. Bajt, D. G. Stearns, and P. A. Kearney, “Investigation of the amorphous-to-crystalline transition in Mo/Si multilayers,” J. Appl. Phys. **90**, 1017–1025 (2001).

[163] S. S. Andreev, S. V. Gaponov, S. A. Gusev, M. N. Haidl, E. B. Kluenkov, K. A. Prokhorov, N. I. Polushkin, E. N. Sadova, N. N. Salashchenko, L. A. Suslov, and S. Y. Zuev, “The microstructure and X-ray reflectivity of Mo/Si multilayers,” Thin Solid Films **415**, 123–132 (2002).

[164] Institut für Arbeitsschutz, IFA, “Gestis-Stoffdatenbank,” `http://www.dguv.de/dguv/ifa/Gefahrstoffdatenbanken` (last accessed: February 2, 2015).

[165] M. Singh and J. J. M. Braat, “Design of multilayer extreme-ultraviolet mirrors for enhanced reflectivity,” Appl. Opt. **39**, 2189–2197 (2000).

[166] J. H. Underwood, E. M. Gullikson, and K. Nguyen, “Tarnishing of Mo/Si multilayer x-ray mirrors,” Appl. Opt. **32**, 6985–6990 (1993).

[167] C. Montcalm, S. Bajt, P. B. Mirkarimi, E. Spiller, F. J. Weber, and J. A. Folta, “Multilayer reflective coatings for extreme-ultraviolet lithography,” Proc. SPIE **3331**, 42–51 (1998).

[168] M. Gritsch, C. Brunner, K. Piplits, H. Hutter, P. Wilhartitz, A. Schintlmeister, and H. P. Martinz, “Application of scanning SIMS techniques for the evaluation of the oxidation behavior of high-purity molybdenum,” Fresen. J. Anal. Chem. **365**, 188–194 (1999).

[169] D. K. Bowen and B. K. Tanner, *X-Ray Metrology in Semiconductor Manufacturing* (CRC Press/Taylor & Francis Group, Boca Raton, Flor., USA, 2006).

[170] A. Duparré and H.-G. Walther, “Surface smoothing and roughening by dielectric thin film deposition,” Appl. Opt. **27**, 1393–1395 (1988).

[171] D. Rönnow, J. Isidorsson, and G. A. Niklasson, “Surface roughness of sputtered $ZrO_2$ films studied by atomic force microscopy and spectroscopic light scattering,” Phys. Rev. E **54**, 4021–4026 (1996).

[172] S. Jakobs, A. Duparré, and H. Truckenbrodt, "Interfacial roughness and related scatter in ultraviolet optical coatings: a systematic experimental approach," Appl. Opt. **37**, 1180–1193 (1998).

[173] A. K. Petford-Long, M. B. Stearns, C.-H. Chang, S. R. Nutt, D. G. Stearns, N. M. Ceglio, and A. M. Hawryluk, "High-resolution electron microscopy study of x-ray multilayer structures," J. Appl. Phys. **61**, 1422–1428 (1987).

[174] J. V. Grishchenko and M. L. Zanaveskin, "Investigation into the Correlation Factor of Substrate and Multilayer Film Surfaces by Atomic Force Microscopy," Crystallogr. Rep. **58**, 493–497 (2013).

[175] C. Bräuer-Burchardt, S. Schröder, M. Trost, P. Kühmstedt, A. Duparré, and G. Notni, "Roughness Determination of Ultra Thin Multilayer Coatings in Cross-Section Images with Poor SNR Using Edge Localization," Proc. ISPA09, pp. 176–181 (2009).

[176] J. M. Nieuwenhuizen and H. B. Haanstra, "Microfractography of thin films," Philips Technical Review **27**, 87–91 (1966).

[177] H. A. Macleod, "Structure-related optical properties of thin films," J. Vac. Sci. Technol. A **4**, 418–422 (1986).

[178] E. L. Church and P. Z. Takacs, "The optimal estimation of finish parameters," Proc. SPIE **1530**, 71–85 (1991).

[179] M. Trost, T. Herffurth, S. Schröder, A. Duparré, and A. Tünnermann, "Scattering reduction through oblique multilayer deposition," Appl. Opt. **53**, A197–A204 (2014).

[180] J. H. Apfel, "Optical coating design with reduced electric field intensity," Appl. Opt. **16**, 1880–1885 (1977).

[181] S. Schröder, D. Unglaub, M. Trost, X. Cheng, J. Zhang, and A. Duparré, "Spectral angle resolved scattering of thin film coatings," Appl. Opt. **53**, A35–A41 (2014).

[182] C. Amra, G. Albrand, and P. Roche, "Theory and application of antiscattering single layers: antiscattering antireflection coatings," Appl. Opt. **25**, 2695–2702 (1986).

[183] C. Amra, C. Deumié, G. Georges, L. Arnaud, M. Zerrad, C. Grèzes-Besset, and F. Chazallet, "Selective cancellation of scattered light in optical substrates and coatings," Proc. SPIE **6720**, 67201G (2007).

[184] I. J. Hodgkinson, P. I. Bowmar, and Q. H. Wu, "Scatter from tilted-columnar birefringent thin films: observation and measurement of anisotropic scatter distributions." Appl. Opt. **34**, 163–168 (1995).

[185] I. J. Hodgkinson, S. C. Cloughley, Q. H. Wu, and S. Kassam, "Anisotropic scatter patterns and anomalous birefringence of obliquely deposited cerium oxide films," Appl. Opt. **35**, 5563–5568 (1996).

[186] S. Kassam, I. J. Hodgkinson, Q. H. Wu, and S. C. Cloughley, "Light scattering from thin films with an oblique columnar structure and with granular inclusions," J. Opt. Soc. Am. A **12**, 2009–2021 (1995).

[187] M. M. Hawkeye and M. J. Brett, "Glancing angle deposition: Fabrication, properties, and applications of micro- and nanostructured thin films," J. Vac. Sci. Technol. A **25**, 1317–1335 (2007).

[188] M. Jergel, V. Holý, E. Majková, S. Luby, and R. Senderák, "Interface study of W-Si/Si and obliquely deposited W/Si multilayers by grazing-incidence high-resolution x-ray diffraction," J. Phys. D: Appl. Phys. **28**, A241–A245 (1995).

[189] D. Le Bellac, G. A. Niklasson, and C. G. Granqvist, "Scaling of Surface Roughness in Obliquely Sputtered Chromium Films," Europhys. Lett. **32**, 155–159 (1995).

[190] A. Besnard, N. Martin, C. Millot, J. Gavoille, and R. Salut, "Effect of sputtering pressure on some properties of chromium thin films obliquely deposited," IOP Conf. Ser.: Mater. Sci. Eng. **12**, 012015 (2010).

[191] J. E. Bjorkholm, "EUV Lithography - The Successor to Optical Lithography?" Intel Technology Journal **Q3**, 1–8 (1998).

[192] H. Meiling, V. Banine, P. Kürz, B. Blum, G. J. Heerens, and N. Harned, "The EUV Program at ASML: an update," Proc. SPIE **5037**, 24–35 (2003).

[193] R. Soufli, S. L. Baker, E. M. Gullikson, T. McCarville, J. C. Robinson, D. Martínez-Galarce, M. Fernández-Perea, and M. J. Pivovaroff, "Review of substrate materials, surface metrologies and polishing techniques for current and future-generation EUV/x-ray optics," Proc. SPIE **8501**, 850102 (2012).

[194] A. H. Leung, D. A. Tichenor, W. C. Replogle, J. E. M. Goldsmith, G. D. Kubiak, R. H. Stulen, W. P. Ballard, K. L. Jefferson, L. E. Klebanoff, D. J. O'Connell, J. B. Wronosky, J. S. Taylor, J. A. Folta, L. C. Hale, H. N. Chapman, D. W. Sweeney, S. H. Lee, D. T. Attwood, K. A. Goldberg, and P. Naulleau, "Current Status of the EUV Engineering Test Stand," J. Photopolym. Sci. Technol. **15**, 351–360 (2002).

[195] D. A. Tichenor, A. K. Ray-Chaudhuri, W. C. Replogle, R. H. Stulen, G. D. Kubiak, P. D. Rockett, L. E. Klebanoff, K. L. Jefferson, A. H. Leung, J. B. Wronosky, L. C.

Hale, H. N. Chapman, J. S. Taylor, J. A. Folta, C. Montcalm, R. Soufli, E. Spiller, K. Blaedel, G. E. Sommargren, D. W. Sweeney, P. Naulleau, K. A. Goldberg, E. M. Gullikson, J. Bokor, P. J. Batson, D. T. Attwood, K. H. Jackson, S. D. Hector, C. W. Gwyn, and P.-Y. Yan, "System Integration and Performance of the EUV Engineering Test Stand," Proc. SPIE **4343**, 19–37 (2001).

[196] M. Trost, S. Schröder, M. Hauptvogel, G. Notni, A. Duparré, and T. Feigl, "Vorrichtung und Verfahren zur winkelaufgelösten Streulichtmessung," Patent DE 10 2012 005 417 B4 (2012).

[197] M. Trost, S. Schröder, A. Duparré, S. Risse, T. Feigl, U. D. Zeitner, and A. Tünnermann, "Structured Mo/Si multilayers for IR-suppression in laser-produced EUV light sources," Opt. Express **21**, 27852–27864 (2013).

[198] F. Draheim, B. Harnisch, and T. Weigel, "Sub surface damage of optical components and the influence on scattering properties," Proc. SPIE **2210**, 709–720 (1994).

[199] J. Wang, Y. Li, J. Han, Q. Xu, and Y. Guo, "Evaluating subsurface damage in optical glasses," J. Eur. Opt. Soc., Rapid Publ. **6**, 11001 (2011).

[200] M. Trost, T. Herffurth, D. Schmitz, S. Schröder, A. Duparré, and A. Tünnermann, "Evaluation of subsurface damage by light scattering techniques," Appl. Opt. **52**, 6579–6588 (2013).

[201] I. A. Artyukov, A. Y. Karabekov, I. V. Kozhevnikov, B. M. Alaudinov, and V. E. Asadchikov, "Experimental observation of the near surface layer effects on X-ray reflection and scattering," Physica B **198**, 9–12 (1994).

[202] V. E. Asadchikov, A. Duparré, S. Jakobs, A. Y. Karabekov, I. V. Kozhevnikov, and Y. S. Krivonosov, "Comparative study of the roughness of optical surfaces and thin films by use of x-ray scattering and atomic force microscopy," Appl. Opt. **38**, 684–691 (1999).

[203] O. N. Gilev, V. E. Asadchikov, A. Duparré, N. A. Havronin, I. V. Kozhevnikov, Y. S. Krivonosov, S. P. Kuznetsov, V. I. Mikerov, V. I. Ostashev, and V. A. Tukarev, "X-ray investigations of a near surface layer of metal samples," Proc. SPIE **4099**, 279–289 (2000).

[204] S. Schröder, M. Kamprath, A. Duparré, A. Tünnermann, B. Kühn, and U. Klett, "Bulk scattering properties of synthetic fused silica at 193 nm," Opt. Express **14**, 10537–10549 (2006).

[205] J. C. Stover, M. L. Bernt, and C. Egert, "Wavelength scaling investigation of several materials," Proc. SPIE **1995**, 256–266 (1993).

[206] J. M. Elson, J. M. Bennett, and J. C. Stover, "Wavelength and angular dependence of light scattering from beryllium: comparison of theory and experiment," Appl. Opt. **32**, 3362–3376 (1993).

[207] C. Wagner, J. Bacelar, N. Harned, E. Loopstra, S. Hendriks, I. de Jong, P. Kuerz, L. Levasier, M. van de Kerkhof, M. Lowisch, H. Meiling, D. Ockwell, R. Peeters, E. van Setten, J. Stoeldraijer, S. Young, J. Zimmerman, and R. Kool, "EUV Lithography at Chipmakers has started: Performance Validation of ASML's NXE:3100," Proc. SPIE **7969**, 79691F (2011).

[208] R. Peeters, S. Lok, E. van Alphen, N. Harned, P. Kuerz, M. Lowisch, H. Meijer, D. Ockwell, E. van Setten, G. Schiffelers, J.-W. van der Horst, J. Stoeldraijer, R. Kazinczi, R. Droste, H. Meiling, and R. Kool, "ASML's NXE platform performance and volume introduction," Proc. SPIE **8679**, 86791F (2013).

[209] N. R. Böwering, I. V. Fomenkov, D. C. Brandt, A. N. Bykanov, A. I. Ershov, W. N. Partlo, D. W. Myers, N. R. Farrar, G. O. Vaschenko, O. V. Khodykin, J. R. Hoffman, C. P. Chrobak, S. N. Srivastava, I. Ahmad, C. Rajyaguru, D. Golich, D. A. Vidusek, S. De Dea, and R. R. Hou, "Performance results of laser-produced plasma test and prototype light sources for EUV lithography," J. Micro/Nanolith. MEMS MOEMS **8**, 041504 (2009).

[210] E. L. Church, "Fractal surface finish," Appl. Opt. **27**, 1518–1526 (1988).

[211] E. L. Church and P. Z. Takacs, "Statistical and signal processing concepts in surface metrology," Proc. SPIE **645**, 107–115 (1986).

[212] M. N. Sweeney, "Advanced Manufacturing Technologies for Light-Weight, Post Polished, Snap-together Reflective Optical System Designs," Proc. SPIE **4771**, 144–154 (2002).

[213] K. H. Krishnan, S. John, K. N. Srinivasan, J. Praveen, M. Ganesan, and P. M. Kavimani, "An Overall Aspect of Electroless Ni-P Depositions - A Review Article," Metall. Mater. Trans. A **37**, 1917–1926 (2006).

[214] R. Steinkopf, A. Gebhardt, S. Scheiding, M. Rohde, O. Stenzel, S. Gliech, V. Giggel, H. Löscher, G. Ullrich, P. Rucks, A. Duparré, S. Risse, R. Eberhardt, and A. Tünnermann, "Metal Mirrors with Excellent Figure and Roughness," Proc. SPIE **7102**, 71020C (2008).

[215] H. Sari, G. Karam, and I. Jeanclaude, “Transmission Techniques for Digital Terrestrial TV Broadcasting,” IEEE Commun. Mag. **33**, 100–109 (1995).

[216] N. Marchetti, M. I. Rahman, S. Kumar, and R. Prasad, “OFDM: Principles and Challenges,” in “New Directions in Wireless Communications Research,” V. Tarokh, ed. (Springer, Dordrecht, Netherlands, 2009), chap. 2, pp. 29–62.

[217] S. B. Weinstein, “The History of Orthogonal Frequency-Devision Multiplexing,” IEEE Commun. Mag. **47**, 26–35 (2009).

[218] Ametek Advanced Measurement Technology, Inc, “Model 7265 DSP Lock-in Amplifier Instruction Manual,” `www.signalrecovery.com/download/190284-A-MNL-C.pdf` (2002, last accessed: February 2, 2015).

[219] A. von Finck, M. Trost, S. Schröder, and A. Duparré, “Parallelized single-detector BRDF measurements,” to be submitted to Appl. Opt. (2015).

[220] M. Trost, T. Herffurth, S. Schröder, A. Duparré, M. Beier, S. Risse, A. Tünnermann, and N. Böwering, “In situ and ex situ characterization of optical surfaces by light scattering techniques,” Opt. Eng. **53**, 092013 (2014).

[221] F. Scholze, J. Tümmler, and G. Ulm, “High-accuracy radiometry in the EUV range at the PTB soft x-ray beamline,” Metrologia **40**, 224–228 (2003).

[222] C. Laubis, F. Scholze, C. Buchholz, A. Fischer, S. Hesse, A. Kampe, J. Puls, C. Stadelhoff, and G. Ulm, “High accuracy EUV reflectometry at large optical components and oblique incidence,” Proc. SPIE **7271**, 72713Y (2009).

[223] E. L. Church, “Statistical effects in the measurement and characterization of smooth scattering surfaces,” Proc. SPIE **511**, 18–22 (1984).

[224] S. Maure, G. Albrand, and C. Amra, “Low-level scattering and localized defects,” Appl. Opt. **35**, 5573–5582 (1996).

[225] T. Herffurth, S. Schröder, M. Trost, A. Duparré, and A. Tünnermann, “Comprehensive nanostructure and defect analysis using a simple 3D light-scatter sensor,” Appl. Opt. **52**, 3279–3287 (2013).

[226] Z. Z. Li, J. M. Wang, X. Q. Peng, L. T. Ho, Z. Q. Yin, S. Y. Li, and C. F. Cheung, “Removal of single point diamond-turning marks by abrasive jet polishing,” Appl. Opt. **50**, 2458–2463 (2011).

[227] K. Tayabaly, J. C. Stover, R. E. Parks, M. Dubin, and J. H. Burge, "Use of the surface PSD and incident angle adjustments to investigate near specular scatter from smooth surfaces," Proc. SPIE **8838**, 883805 (2013).

[228] A. Gebhardt, S. Scheiding, J. Kinast, S. Risse, A. Duparré, M. Trost, R.-R. Rohloff, V. Schönherr, V. Giggel, and H. Löscher, "Nickel Plated Metal Mirrors for Advanced Applications," 26th Annual Meeting of the American Society for Precision Engineering, ASPE, Denver, Colo., USA (2011).

[229] M. Schürmann, P. J. Jobst, S. Yulin, T. Feigl, H. Heiße, S. Wilbrandt, O. Stenzel, A. Gebhardt, S. Risse, and N. Kaiser, "Optical reflector coatings for astronomical applications from EUV to IR," Proc. SPIE **8450**, 84502K (2012).

[230] M. Kriese, Y. Platonov, B. Ehlers, L. Jiang, J. Rodriguez, U. Mueller, J. Daniel, S. Khatri, A. Magruder, S. Grantham, C. Tarrio, and T. Lucatorto, "Development of an EUVL collector with infrared radiation suppression," Proc. SPIE **9048**, 90483C (2014).

[231] R. ter Horst, N. Tromp, M. de Haan, R. Navarro, L. Venema, and J. Pragt, "Directly Polished Light Weight Aluminum Mirror," Proc. SPIE **7018**, 701808 (2008).

[232] K. J. Moeggenborg, C. Barros, S. Lesiak, N. Naguib, and S. Reggie, "Low-scatter bare aluminum optics via chemical mechanical polishing," Proc. SPIE **7060**, 706002 (2008).

[233] C. C. Asmail, J. Hsia, A. Parr, and J. Hoeft, "Rayleigh scattering limits for low-level bidirectional reflectance distribution function measurements," Appl. Opt. **33**, 6084–6091 (1994).

[234] T. A. Germer and C. C. Asmail, "A goniometric optical scatter instrument for bidirectional reflectance distribution function measurements with out-of-plane and polarimetry capabilities," Proc. SPIE **3141**, 220–231 (1997).

[235] M. Trost, S. Schröder, and T. Herffurth, "Verfahren zur hochempfindlichen Streulichtmessung," Patent DE 10 2012 106 322 B3 (2012).

[236] K. Hrdina, "Production and Properties of ULE® Glass with Regards to EUV Masks," 1st International EUVL Workshop (1999).

[237] L. Coriand, "Roughness, wetting, and optical properties of functional surfaces," Ph.D. thesis, Friedrich Schiller University Jena (2012).

[238] W. Vogel, *Glaschemie* (Springer, Berlin, 1992), 3rd ed.

[239] A. Mallik, W. Vansumere, J. Ryckaert, A. Mercha, N. Horiguchi, S. Demuynck, J. Bömmels, T. Zsolt, G. Vandenberghe, K. Ronse, A. Thean, D. Verkest, H. Lebon, and A. Steegen, “The need for EUV lithography at advanced technology for sustainable wafer cost,” Proc. SPIE **8679**, 86792Y (2013).

[240] T. Tomie, “Tin laser-produced plasma as the light source for extreme ultraviolet lithography high-volume manufacturing: history, ideal plasma, present status, and prospects,” J. Micro/Nanolith. MEMS MOEMS **11**, 021109 (2012).

[241] I. V. Fomenkov, A. I. Ershov, W. N. Partlo, D. W. Myers, D. Brown, R. L. Sandstrom, B. La Fontaine, A. N. Bykanov, G. O. Vaschenko, O. V. Khodykin, N. R. Böwering, P. Das, V. B. Fleurov, K. Zhang, S. N. Srivastava, I. Ahmad, C. Rajyaguru, S. De Dea, R. R. Hou, W. J. Dunstan, P. Baumgart, T. Ishihara, R. D. Simmons, R. N. Jacques, R. A. Bergstedt, and D. C. Brandt, “Laser Produced Plasma Light Source for EUVL,” Proc. SPIE **7969**, 796933 (2011).

[242] N. R. Farrar, B. M. La Fontaine, I. V. Fomenkov, and D. C. Brandt, “Advances in EUV light sources,” Adv. Opt. Techn. **1**, 279–287 (2012).

[243] D. C. Brandt, I. V. Fomenkov, N. R. Farrar, B. La Fontaine, D. W. Myers, D. J. Brown, A. I. Ershov, N. R. Böwering, D. J. Riggs, R. J. Rafac, S. De Dea, R. Peeters, H. Meiling, N. Harned, D. Smith, A. Pirati, and R. Kazinczi, “LPP EUV Source Readiness for NXE 3300B,” Proc. SPIE **9048**, 90480C (2014).

[244] N. Böwering, “EUV Light Sources for Device Development and Manufacturing,” 273rd PTB–Seminar VUV and EUV Metrology, Berlin (2013).

[245] H. Mizoguchi, H. Nakarai, T. Abe, T. Ohta, K. Nowak, Y. Kawasuji, H. Tanaka, Y. Watanabe, T. Hori, T. Kodama, Y. Shiraishi, T. Yanagida, T. Yamada, T. Yamazaki, S. Okazaki, and T. Saitou, “LPP-EUV Light Source Development for High Volume Manufacturing Lithography,” Proc. SPIE **8679**, 86790A (2013).

[246] I. V. Fomenkov, D. C. Brandt, N. R. Farrar, B. La Fontaine, D. W. Myers, D. J. Brown, A. I. Ershov, N. R. Böwering, D. J. Riggs, R. J. Rafac, S. De Dea, M. Purvis, R. Peeters, H. Meiling, N. Harned, D. Smith, R. Kazinczi, and A. Pirati, “Laser Produced Plasma Light Source Development for HVM,” Proc. SPIE **9048**, 904835 (2014).

[247] K. Nishihara, A. Sasaki, A. Sunahara, and T. Nishikawa, “Conversion Efficiency of LPP Sources,” in “EUV Sources for Lithography,” V. Bakshi, ed. (SPIE Press, Bellingham, Wash., USA, 2005), chap. 11, pp. 339–370.

[248] C. Mbanaso, A. Antohe, H. Bull, F. Goodwin, A. Hershcovitch, and G. Denbeaux, “Out-of-band radiation mitigation at 10.6 µm by molecular absorbers in laser-produced plasma extreme ultraviolet sources,” J. Micro/Nanolith. MEMS MOEMS **11**, 021116 (2012).

[249] M. S. Bibishkin, N. I. Chkhalo, S. A. Gusev, E. B. Kluenkov, A. Y. Lopatin, V. I. Luchin, A. E. Pestov, N. N. Salashchenko, L. A. Shmaenok, N. N. Tsybin, and S. Y. Zuev, “Multilayer Zr/Si filters for EUV lithography and for radiation source metrology,” Proc. SPIE **7025**, 702502 (2008).

[250] W. A. Soer, M. J. J. Jak, A. M. Yakunin, M. M. J. W. van Herpen, and V. Y. Banine, “Grid spectral purity filters for suppression of infrared radiation in laser-produced plasma EUV sources,” Proc. SPIE **7271**, 72712Y (2009).

[251] W. A. Soer, P. Gawlitza, M. M. J. W. van Herpen, M. J. J. Jak, S. Braun, P. Muys, and V. Y. Banine, “Extreme ultraviolet multilayer mirror with near-zero IR reflectance,” Opt. Lett. **34**, 3680–3682 (2009).

[252] Q. Huang, D. M. Paardekooper, E. Zoethout, V. V. Medvedev, R. van de Kruijs, J. Bosgra, E. Louis, and F. Bijkerk, “UV spectral filtering by surface structured multilayer mirrors,” Opt. Lett. **39**, 1185–1188 (2014).

[253] H. Kierey, K. Heidemann, B. Kleemann, R. Winters, W. Egle, W. Singer, F. Melzer, R. Wevers, and M. Antoni, “EUV spectral purity filter: optical and mechanical design, gratings fabrication, and testing,” Proc. SPIE **5193**, 70–78 (2004).

[254] A. J. R. van den Boogaard, F. A. van Goor, E. Louis, and F. Bijkerk, “Wavelength separation from extreme ultraviolet mirrors using phaseshift reflection,” Opt. Lett. **37**, 160–162 (2012).

[255] D. C. O’Shea, T. J. Suleski, A. D. Kathman, and D. W. Prather, *Diffractive Optics Design, Fabrication, and Test* (SPIE Press, Bellingham, Wash., USA, 2004).

[256] M. G. Moharam and T. K. Gaylord, “Rigorous coupled-wave analysis of planar-grating diffraction,” J. Opt. Soc. Am. **71**, 811–818 (1981).

[257] N. R. Böwering, J. R. Hoffman, O. V. Khodykin, C. L. Rettig, B. A. M. Hansson, A. I. Ershov, and I. V. Fomenkov, “Metrology of laser-produced plasma light source for EUV lithography,” Proc. SPIE **5752**, 1248–1256 (2005).

[258] D. C. Brandt, I. V. Fomenkov, N. R. Farrar, B. La Fontaine, D. W. Myers, D. J. Brown, A. I. Ershov, R. L. Sandstrom, G. O. Vaschenko, N. R. Böwering, P. Das,

V. B. Fleurov, K. Zhang, S. N. Srivastava, I. Ahmad, C. Rajyaguru, S. De Dea, W. J. Dunstan, P. Baumgart, T. Ishihara, R. D. Simmons, R. N. Jacques, R. A. Bergstedt, P. I. Porshnev, C. J. Wittak, R. J. Rafac, J. Grava, A. A. Schafgans, Y. Tao, K. Hoffmann, T. Ishikawa, D. R. Evans, and S. D. Rich, "$CO_2$/Sn LPP EUV sources for device development and HVM," Proc. SPIE **8679**, 86791G (2013).

[259] H. Voorma, E. Louis, N. B. Koster, F. Bijkerk, T. Zijlstra, L. E. M. de Groot, B. A. C. Rousseeuw, J. Romijn, E. W. J. M. van der Drift, and J. Friedrich, "Fabrication and analysis of extreme ultraviolet reflection masks with patterned W/C absorber bilayers," J. Vac. Sci. Technol. B **15**, 293–298 (1997).

[260] S. D. Hector, "EUVL Masks: Requirements and Potential Solutions," Proc. SPIE **4688**, 134–149 (2002).

[261] A. R. Pawloski, B. La Fontaine, H. J. Levinson, S. Hirscher, S. Schwarzl, K. Lowack, F.-M. Kamm, M. Bender, W.-D. Domke, C. Holfeld, U. Dersch, P. Naulleau, F. Letzkus, and J. Butschke, "Comparative Study of Mask Architectures for EUV Lithography," Proc. SPIE **5567**, 762–773 (2004).

[262] A. M. Nugrowati, A. S. van de Nes, S. F. Pereira, and J. J. M. Braat, "EUV phase mask engineering based on image optimisation," Microelectron. Eng. **83**, 684–687 (2006).

[263] C. K. Malek, F. R. Ladan, R. Rivoira, and T. Moreno, "Application of e-beam lithography and reactive ion etching to the fabrication of masks for projection x-ray lithography," J. Vac. Sci. Technol. B **9**, 3315–3318 (1991).

[264] J. H. Peters, "Status of EUVL mask development in Europe," Proc. SPIE **5853**, 297–307 (2005).

[265] S.-I. Han, E. Weisbrod, Q. Xie, P. J. S. Mangat, S. D. Hector, and W. J. Dauksher, "Design and Method of Fabricating Phase Shift Masks for Extreme Ultraviolet Lithography by Partial Etching into the EUV Multilayer Mirror," Proc. SPIE **5037**, 314–330 (2003).

[266] L. Dreeskornfeld, G. Haindl, U. Kleineberg, U. Heinzmann, F. Shi, B. Volland, I. W. Rangelow, E. Majkova, S. Luby, Kostic, L. Matay, P. Hrkut, P. Hudek, and H.-Y. Lee, "Nanostructuring of Mo/Si multilayers by means of reactive ion etching using a three-level mask," Thin Solid Films **458**, 227–232 (2004).

[267] L. Dreeskornfeld, R. Segler, G. Haindl, O. Wehmeyer, S. Rahn, E. Majkova, U. Kleineberg, U. Heinzmann, P. Hudek, and I. Kostic, "Reactive ion etching with end

point detection of microstructured Mo/Si multilayers by optical emission spectroscopy," Microelectron. Eng. **54**, 303–314 (2000).

[268] A. J. R. van den Boogaard, "Ion-enhanced growth in planar and structured Mo/Si multilayers," Ph.D. thesis, University of Twente (2011).

[269] E. Louis, "Physics and technology development of multilayer EUV reflective optics," Ph.D. thesis, University of Twente (2012).

[270] T. Feigl, M. Perske, H. Pauer, T. Fiedler, U. Zeitner, R. Leitel, A. Matthes, M. Trost, S. Schröder, F. Scholze, and C. Laubis, "Dual-wavelength spectral purity filter for EUV collector mirrors," International Symposium on Extreme Ultraviolet Lithography, Washington, D.C., USA (2014).

[271] J.-M. André, P. Jonnard, C. Michaelsen, J. Wiesmann, F. Bridou, M.-F. Ravet, A. Jérome, F. Delmotte, and E. O. Filatova, "La/$B_4C$ small period multilayer interferential mirror for the analysis of boron," X-Ray Spectrom. **34**, 203–206 (2005).

[272] S. S. Andreev, M. M. Barysheva, N. I. Chkhalo, S. A. Gusev, A. E. Pestov, V. N. Polkovnikov, N. N. Salashchenko, L. A. Shmaenok, Y. A. Vainer, and S. Y. Zuev, "Multilayered mirrors based on La/$B_4C$($B_9C$) for X-ray range near anomalous dispersion of boron ($\lambda \approx 6.7\,\mathrm{nm}$)," Nucl. Instrum. Methods A **603**, 80–82 (2009).

[273] S. Yulin, V. Nesterenko, T. Feigl, and N. Kaiser, "Reflective optics for next generation lithography," International Symposium on Extreme Ultraviolet Lithography, Miami, Flor., USA (2011).

[274] Y. Platonov, J. Rodriguez, M. Kriese, E. Gullikson, T. Harada, T. Watanabe, and H. Kinoshita, "Multilayers for next generation EUVL at 6.Xnm," Proc. SPIE **8076**, 80760N (2011).

[275] M. Barthelmess and S. Bajt, "Thermal and stress studies of normal incidence Mo/$B_4C$ multilayers for a 6.7 nm wavelength," Appl. Opt. **50**, 1610–1619 (2011).

[276] S. S. Churilov, R. R. Kildiyarova, A. N. Ryabtsev, and S. V. Sadovsky, "EUV spectra of Gd and Tb ions excited in laser-produced and vacuum spark plasmas," Phys. Scr. **80**, 045303 (2009).

[277] T. Otsuka, B. Li, C. O'Gorman, T. Cummins, D. Kilbane, T. Higashiguchi, N. Yugami, W. Jiang, A. Endo, P. Dunne, and G. O'Sullivan, "A 6.7-nm beyond EUV source as a future lithography source," Proc. SPIE **8322**, 832214 (2012).

[278] M. Vidal-Dasilva, M. Fernández-Perea, J. A. Méndez, J. A. Aznárez, and J. I. Larruquert, “Electron-beam deposited boron coatings for the extreme ultraviolet,” Appl. Opt. **47**, 2926–2930 (2008).

[279] S. S. Andreev, M. M. Barysheva, N. I. Chkhalo, S. A. Gusev, A. E. Pestov, V. N. Polkovnikov, D. N. Rogachev, N. N. Salashchenko, Y. A. Vainer, and S. Y. Zuev, “Multilayer X-ray Mirrors Based on La/$B_4C$ and La/$B_9C$,” Tech. Phys. **55**, 1168–1174 (2010).

[280] F. Choueikani, F. Bridou, B. Lagarde, E. Meltchakov, F. Polack, P. Mercere, and F. Delmotte, “X-ray properties and interface study of $B_4C$/Mo and $B_4C$/$Mo_2C$ periodic multilayers,” Appl. Phys. A **111**, 191–198 (2013).

[281] Y. Zhou, P. D. Funkenbusch, D. J. Quesnel, D. Golini, and A. Lindquist, “Effect of Etching and Imaging Mode on the Measurement of Subsurface Damage in Microground Optical Glasses,” J. Am. Ceram. Soc. **77**, 3277–3280 (1994).

[282] J. A. Menapace, P. J. Davis, W. A. Steele, L. L. Wong, T. I. Suratwala, and P. E. Miller, “MRF Applications: Measurement of Process-dependent Subsurface Damage in Optical Materials using the MRF Wedge Technique,” Proc. SPIE **5991**, 599103 (2005).

[283] J. A. Randi, J. C. Lambropoulos, and S. D. Jacobs, “Subsurface damage in some single crystalline optical materials,” Appl. Opt. **44**, 2241–2249 (2005).

[284] X. Tonnellier, P. Morantz, P. Shore, A. Baldwin, R. Evans, and D. D. Walker, “Subsurface damage in precision ground ULE® and Zerodur® surfaces,” Opt. Express **15**, 12197–12205 (2007).

[285] M. Trost, S. Schröder, T. Feigl, A. Duparré, and A. Tünnermann, “Roughness characterization of large EUV mirror optics by laser light scattering,” Proc. SPIE **8169**, 81690P (2011).

[286] M. Trost, S. Schröder, C. C. Lin, A. Duparré, and A. Tünnermann, “Roughness characterization of EUV multilayer coatings and ultra-smooth surfaces by light scattering,” Proc. SPIE **8501**, 85010F (2012).

# Acknowledgements

I would like to express my sincere gratitude to a number of people whose support throughout the last few years has made this thesis possible.

Firstly, I would like to sincerely thank my supervisor Prof. Dr. Andreas Tünnermann, for his encouragement and guidance throughout the work. His constructive criticism and valuable comments contributed significantly to the success of the work and were always highly appreciated.

I am also especially indebted to Dr. Angela Duparré, head of the surface and thin film characterization group at the Fraunhofer IOF, for providing me with the interesting subject of this thesis. She was always happy to give me advice, guidance, and support while at the same time allowing me a great degree of freedom to choose the research path.

Furthermore, I would like to thank Dr. Sven Schröder who introduced me to the art of measuring light scattering but also later showed a deep interest in my work. In particular, his brilliant input and encouraging feedback have helped me to go to the very edge of scientific knowledge and - hopefully - a bit beyond.

I would also like to thank Matthias Hauptvogel, Tobias Herffurth, Alexander von Finck, and David Schmitz for numerous fruitful discussions on scattering, their great lab expertise, and countless joyful hours at work. Dr. Luisa Coriand, Nadja Felde, and Christian Wiede deserve thanks as well for their fast and reliable AFM and WLI measurements even of the most delicate and challenging samples.

My gratitude further extends to many of my colleagues at the Fraunhofer IOF from the optical systems department headed by Prof. Dr. Gunther Notni, the optical coatings department, the precision engineering department, and the microoptical systems department for the kind support, the professional work, and the friendly atmosphere. In particular, I would like to mention Dr. Torsten Feigl, Hagen Pauer, Marco Perske, (all now with optiX fab), Dr. Sergiy Yulin, Dr. Stefan Risse, Robert Jende, Sandra Müller, Dr. Uwe Zeitner, and Dr. Robert Leitel who also provided me with many of the different samples presented in this thesis.

I am also very grateful to the people with whom I had the opportunity to cooperate on the various aspects of this work. In particular, I would like to name Dr. Norbert Böwering (Cymer, Netherlands), Chihcheng Lin (Sematech, USA), and Dr. Jue Wang (Corning, USA) who offered me the opportunity to characterize some of the most unique optics ever fabricated. Additionally, their willingness and support when it came to the publication of the results and to get the articles through the industrial clearance process are well remembered and valued. Special thanks go to Dr. John Stover (The Scatter Works, USA), Dr. Peter Takacs (Brookhaven National Laboratory, USA), and Prof. James Harvey (University of

Central Florida / Photon Engineering, USA) for sharing their profound knowledge on surface roughness and scattering as well as for answering even the most tedious questions regarding scattering during their visits in Jena as well as several conference meetings.

I would also like to thank Lars Mejnertsen and Méabh Garrick for the final proof reading of the manuscript and answering my surely never ending questions to the very last detail of the English language.

Last but not least, I am deeply indebted to my friends and family who have permanently given me great support and joyful times, which has always helped to free my mind and gain new motivation. I would especially like to express my sincere gratitude to my parents, my two brothers Tobias and Jonas, as well as Bernadette for their unlimited support and patience throughout the past years, which contributed an essential part to the success of this thesis.

# Kurzzusammenfassung

Die stetige Reduzierung der Belichtungswellenlängen in der optischen Lithographie, motiviert durch die Herstellung immer kleinerer Halbleiterbauelemente, zieht enorme Herausforderungen an optische Komponenten nach sich. Insbesondere Streulicht an optischen Oberflächen stellt durch die starke Wellenlängenabhängigkeit gegenüber Oberflächenimperfektionen ($\sim {}^1\!/\!_{\lambda^4}$) einen kritischen Faktor dar. Das Ziel dieser Arbeit bestand daher in der Untersuchung der Rauheits- und Streulichteigenschaften von Mo/Si Mehrschichtsystemen für die nächste geplante Lithographiewellenlänge $\lambda = 13{,}5\,\mathrm{nm}$.

Neben der Charakterisierung und Klassifizierung der wesentlichen Streulichtmechanismen, wie etwa die durch das Schichtsystem replizierte Substratrauheit und die intrinsische Schichtrauheit, wurden neue Lösungsstrategien erarbeitet, um Streulicht von Mehrschichtsystemen gezielt zu minimieren. So konnte beispielsweise durch eine schiefe Beschichtung des Mo/Si Mehrschichtsystems eine Streulichtreduzierung von über 28% gegenüber einem gleichartigen, senkrecht beschichteten Spiegel, ohne eine Degradation des spekularen Reflexionsgrades, erzielt werden.

Wesentlich für geringe Streulichtverluste ist ebenfalls eine niedrige Substratrauheit, da diese weitestgehend durch das Schichtsystem repliziert wird. Aufgrund der komplexen Formen und großen Abmessungen von EUV-Optiken, mit mehreren 100 mm Durchmesser, stoßen klassische hochauflösende Rauheitsmessverfahren, wie das Rasterkraftmikroskop, allerdings schnell an ihre Grenzen. Daher wurde im Rahmen der Arbeit ein neuartiges flächendeckendes Charakterisierungsverfahren entwickelt, welches auf winkelaufgelösten Streulichtmessungen bei visuellen Wellenlängen basiert. Dieses ermöglicht es, Rauheitskarten der gesamten Oberfläche zu erstellen und somit detaillierte Aussagen bezüglich der Homogenität sowie einzelner Defektbereiche zu treffen. Im Zusammenspiel mit der Modellierung der Streulichteigenschaften des Mo/Si Mehrschichtsystems können so schon vor der Beschichtung Aussagen über den späteren EUV-Reflexionsgrad getroffen werden. Dadurch wird bereits früh im gesamten Herstellungsprozess eine zielgerichtete Optimierung möglich, da zu diesem Zeitpunkt das Substrat an kritischen Bereichen überpoliert werden kann. Selbst extrem niedrige, hochfrequente Rauheiten von $< 0{,}04\,\mathrm{nm}$ können mit dem streulichtbasierten Verfahren zuverlässig bestimmt werden. Dies entspricht dem typischen Rauschlimit eines Rasterkraftmikroskops.

Ein weiteres, sehr junges Forschungsfeld sind optische Komponenten für eine Wellenlänge von 6,x nm, die derzeit als nächste Lithographiewellenlänge nach $\lambda = 13{,}5\,\mathrm{nm}$ intensiv diskutiert wird. Um eine erste Abschätzung der Streulichteigenschaften und kritischen Rauheitsparameter zu ermöglichen, wurde daher am Ende der Arbeit auf die Rauheitsentwicklung von Mehrschichtsystemen für eine Wellenlänge von $\lambda = 6{,}7\,\mathrm{nm}$, basierend auf Lanthan und Ruthenium als hochbrechenden Materialien, eingegangen. Im Gegensatz zu Mo/Si Mehrschichtspiegeln zeigte sich, dass die Streulichteigenschaften weitestgehend durch die intrinsische Schichtrauheit bestimmt werden. Dieser vorteilhafte Umstand ist darauf zurückzuführen, dass die für die Streuung relevanten Rauheitskomponenten des Substrates durch das Schichtsystem geglättet werden.

# Ehrenwörtliche Erklärung

Ich erkläre hiermit ehrenwörtlich, dass ich die vorliegende Arbeit selbständig, ohne unzulässige Hilfe Dritter und ohne Benutzung anderer als der angegebenen Hilfsmittel und Literatur angefertigt habe. Die aus anderen Quellen direkt oder indirekt übernommenen Daten und Konzepte sind unter Angabe der Quellen gekennzeichnet.

Bei der Auswahl und Auswertung des folgenden Materials haben mir die nachstehend aufgeführten Personen in der jeweils beschriebenen Weise unentgeltlich geholfen:

1. Dr. Torsten Feigl, Hagen Pauer und Marco Perske (optiX fab GmbH, Jena): Herstellung von EUV-Schichtsystemen und Röntgenreflektometriemessungen an Einfachschichten
2. Dr. Sergiy Yulin (Fraunhofer IOF, Jena): Herstellung von Schichtsystemen für $\lambda = 6.7\,\mathrm{nm}$
3. Dr. Norbert Böwering (Cymer BV, Veldhoven, Niederlande): Bereitstellung von EUV-Kollektorspiegelsubstraten
4. Chihcheng Lin (Sematech, Albany, N.Y., USA): Bereitstellung einer unstrukturierten EUV-Maske
5. Dr. Jue Wang (Corning Tropel Corporation, Fairport, N.Y., USA): Bereitstellung von $CaF_2$ Substraten mit unterschiedlichen SSD Gehalt
6. Dr. Frank Scholze und Christian Buchholz (Physikalisch-Technische Bundesanstalt, Berlin): EUV-Spektralphotometrie
7. Prof. Dr. Ute Kaiser und Dr. Johannes Biskupek (Universität Ulm, Ulm): HRTEM Messungen
8. Dr. Christian Bräuer-Burchardt (Fraunhofer IOF, Jena): Entwicklung Kantenfindungsalgorithmus
9. Dr. Luisa Coriand, Christian Wiede und Nadja Felde (Fraunhofer IOF, Jena): AFM/WLI Messungen
10. Dr. Stefanie Kroker (Friedrich-Schiller-Universität Jena, Institut für Angewandte Physik): RCWA Berechnungen

Weitere Personen waren an der inhaltlich-materiellen Erstellung der vorliegenden Arbeit nicht beteiligt. Insbesondere habe ich hierfür nicht die entgeltliche Hilfe von Vermittlungs- bzw. Beratungsdiensten (Promotionsberater oder anderen Personen) in Anspruch genommen. Niemand hat von mir unmittelbar oder mittelbar geldwerte Leistungen für Arbeiten erhalten, die im Zusammenhang mit dem Inhalt der vorgelegten Dissertation stehen.

Teile dieser Arbeit wurden aus Prioritätsgründen bereits veröffentlicht oder zur Veröffentlichung eingereicht [114, 179, 196, 197, 200, 220, 235, 285, 286].

Die Arbeit wurde bisher weder im In- noch im Ausland in gleicher oder ähnlicher Form einer anderen Prüfungsbehörde vorgelegt.

Die geltende Promotionsordnung der Physikalisch-Astronomischen Fakultät ist mir bekannt.

Ich versichere ehrenwörtlich, dass ich nach bestem Wissen die reine Wahrheit gesagt und nichts verschwiegen habe.

Jena, 2. Februar 2015 Marcus Trost

# Lebenslauf

**Name:** Marcus Trost

**Geburtsdatum:** 17.08.1982

**Geburtsort:** Heilbad Heiligenstadt

## Schulischer und akademischer Werdegang

| | |
|---|---|
| 1989 – 1993 | Staatliche Grundschule *Theodor Storm*, Heilbad Heiligenstadt |
| 1993 – 1999 | *Bergschule St. Elisabeth*, staatlich anerkanntes katholisches Gymnasium, Heilbad Heiligenstadt |
| 1999 – 2000 | *North High School*, Sioux City, Iowa, USA |
| 2000 – 2002 | *Bergschule St. Elisabeth*, staatlich anerkanntes katholisches Gymnasium, Heilbad Heiligenstadt, Abschluss: Abitur |
| 2002 – 2003 | Zivildienst in der Verwaltung des *Naturparks Eichsfeld-Hainich-Werratal*, Fürstenhagen |
| 2003 – 2009 | Studium an der *Friedrich-Schiller-Universität Jena* |
| 25.03.2009 | Diplom im Studiengang Physik |
| 04/2009 – 10/2009 | wissenschaftlicher Mitarbeiter am *Fraunhofer IOF*, Jena |
| seit 10/2009 | Doktorand am *Institut für Angewandte Physik* an der *Friedrich-Schiller-Universität Jena / Fraunhofer IOF*, Jena |

Jena, Januar 2015